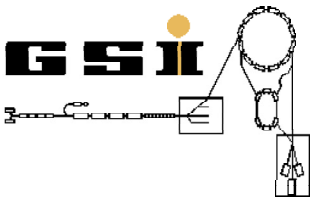

Investigation of the nuclear matter density distributions of the exotic ^{12}Be, ^{14}Be and ^{8}B nuclei by elastic proton scattering in inverse kinematics

Dissertation

zur

Erlangung des Grades

"Doktor der Naturwissenschaften"

am Fachbereich Physik

der Johannes Gutenberg-Universität

in Mainz

Stoyanka Ilieva

geb. in Sofia, Bulgarien

Mainz, 2008

Summary

The proton-nucleus elastic scattering at intermediate energies is a well-established method for the investigation of the nuclear matter distribution in stable nuclei and was recently also applied for the investigation of radioactive nuclei using the method of inverse kinematics.

In the current experiment the differential cross section for proton elastic scattering on the isotopes ^{7,9,10,11,12,14}Be and ^{8}B was measured. The experiment was performed at GSI, Darmstadt. The beams of exotic nuclei were produced via fragmentation of a primary beam (^{12}C or ^{18}O) and separated by means of the GSI fragment separator (FRS). The main part of the experimental setup was the time projection ionization chamber IKAR which was simultaneously used as hydrogen target and a detector for the recoil protons. The trajectories of the projectiles were determined by a set of multi-wire proportional chambers placed two in front of IKAR and two after it, respectively. Several scintillator detectors placed throughout the experimental setup were used for Z-identification of the projectiles and for the trigger signal. As compared to the experiments on investigating the neutron-rich He and Li isotopes, performed with similar setup, there were several improvements. The experimental setup was build in a different experimental hall where better transmission of the radioactive beam from FRS was achievable which leads to higher intensity beams. Multi-wire proportional chambers with individual strip read-out, which gives better resolution as compared to the ones used in previous IKAR experiments, were used. Different trigger logic was applied which resulted in more events written to tape.

As results from the experiment the absolute differential cross sections $\mathrm{d}\sigma/\mathrm{d}t$ as a function of the four momentum transfer t were obtained. In this work the differential cross sections for elastic p-^{12}Be, p-^{14}Be and p-^{8}B scattering at low t ($t \leq 0.05$ (GeV/c)^2) are presented.

The measured cross sections were analyzed within the Glauber multiple-scattering theory and the nuclear matter density distributions and radii of the investigated isotopes were determined. For deducing the density distributions, the cross sections were calculated within the Glauber theory using various parameterizations of the density functions. As a first approach phenomenological density distributions were used and their parameters were fitted to the experimental cross sections. In a more model independent analysis the density distribution was expanded on a basis of Gaussian functions (Sum of Gaussian analysis) and the free parameters were also fitted to the experimental data. In this case no constraints on the shape of the nucleus are made a priori.

The analysis of the differential cross section for the isotope ^{14}Be shows that a good description of the experimental data is obtained when density distributions consisting of separate core and halo components are used. The parameterizations SF, GG, GO and GH give the best description. The results imply the existence of a halo structure in the isotope ^{14}Be with a possible configuration of a ^{12}Be core and two valence neutrons. The determined *rms* matter radius is $3.11 \pm 0.04 \pm 0.13$ fm. Consistent results are obtained when assuming a structure of ^{10}Be core and four halo neutrons for ^{14}Be.

In the case of the ^{12}Be nucleus, a good description of the experimental data is

obtained with the GG, GO, GH and SOG parameterizations. The results showed an extended matter distribution for this nucleus as well. The halo consists of two valence neutrons around ^{10}Be core. For this nucleus a matter radius of $2.82 \pm 0.03 \pm 0.12$ fm was determined. An interesting result is that the free ^{12}Be nucleus behaves differently as compared to the core of ^{14}Be and is much more extended than it.

Preliminary experimental results for the isotope ^{8}B are also presented. The density distribution was parameterized with the GG, GO and GH functions. An extended matter distribution was obtained (though much more compact as compared to the neutron halos). A proton halo structure was observed for the first time with the proton elastic scattering method. The deduced matter radius is $2.60 \pm 0.02 \pm 0.26$ fm.

The density distributions from microscopic theoretical calculations were used as an input to the Glauber theory to calculate the differential cross sections which were then compared to the experimental data. Microscopic densities calculated within the FMD (Fermionic Molecular Dynamics) model and in a few-body calculation were used. The calculated cross sections describe the experimental data relatively well and the calculated densities are close to the ones deduced from the present analysis for the cases of ^{14}Be and ^{8}B. In the case of ^{12}Be bigger discrepancies are observed. A significant contribution of intruder states from the *sd* shell to the structure of the ^{12,14}Be nuclei was confirmed. In the case of ^{12}Be the the *sd* intruder states play important role for the $N = 8$ neutron magic number disappearance. The provided experimental data can be used as an input to theoretical calculations to further investigate the shell breaking and the clustering effects.

The results obtained in the present analysis are in most cases consistent with previous experimental studies of the same isotopes with different experimental methods (total interaction and reaction cross section measurements, momentum distribution measurements). In the case of the ^{12}Be isotope slightly larger matter radius than the previously measured one was determined.

The EXL project within the NUSTAR project at the future accelerator facility FAIR proposes a new universal detector system for studies of light-ion induced reactions. The EXL detector setup will be installed at the new experimental storage ring (NESR) where reactions of radioactive beams with internal gas targets can be studied. The FAIR facility provides high intensity radioactive beams and the usage of storage ring techniques increases further the luminosity which is very important for experiments with rare isotopes. The proposed setup will allow, among others, the investigation of the nuclear matter distribution of exotic nuclei in regions of the nuclear chart not accessible with present techniques. Within this thesis a feasibility study of the EXL setup was performed using a stable ^{136}Xe beam. Detectors representing all the major systems of EXL were installed in the ESR at GSI and tested. Check of the achievable luminosity was performed and different reaction channels were separated. The results from this test experiment were promising and the feasibility of the setup was confirmed.

Contents

List of Tables

List of Figures

CHAPTER 1

Introduction

1.1 Measuring nuclear sizes and shapes

The nuclear structure of stable nuclei is fairly well known and the existing nuclear models are able to describe the properties of such nuclei in most cases with reasonable accuracy. At the same time, when going away from the valley of stability, the predictions of the theoretical models in most cases deviate substantially from the experimental results. In the last decades, since radioactive beams became available, the major interest has been focused on performing experiments with exotic nuclei, which expand the knowledge about nuclear structure and the results can be used to test and improve the predicting power of various theoretical models.

The size and radial distribution of the nuclear charge and matter receive considerable attention as these are fundamental properties of the nuclear many-body system. The theoretical models attempting to describe the nuclear system have as basic parameters, among many others, the size and the shape of the nucleus. Thus, it is not surprising that physicists keep their interest in determining these observables.

Many methods have been developed to study the nuclear density distributions of stable nuclei. Standard methods for probing the charge density and radius are the elastic electron scattering and the isotope shift measurements of X-rays from muonic and electronic atoms [1]. To obtain the charge densities, electromagnetic probes are used and thus, precise information about the distributions can be obtained due to the fact that the electromagnetic interaction is very well known. Using (e,e) elastic scattering, experiments at low and high momentum transfer were performed and the charge densities of stable isotopes were extensively investigated. The charge densities of some exotic nuclei were also investigated by isotope shift measurements using laser spectroscopy. The charge radii of the He [2] and Li [3] isotopes were determined and recently also the charge radii in the ^{7,9,10,11}Be isotopes [4] were investigated. The ^{12}Be and ^{14}Be isotopes are still not investigated due to the limited production rate

of these nuclei at low beam energies.

Experiments on hadron elastic scattering and total cross section measurements provide information about the nuclear matter density distribution [1]. Additionally, from the momentum distributions of the fragments from break-up reactions the *rms* nuclear matter radii can be determined. In this case, due to the approximate knowledge of the nucleus-nucleus interaction and the reaction process, relatively large uncertainties in the results are present. Besides, the hadron elastic scattering is more difficult to perform at high momentum transfer due to the increasing contribution of inelastic processes.

If the matter $\rho_m(r)$ and charge $\rho_{ch}(r)$ density (which is equivalent to the proton density $\rho_p(r)$) distributions are known, the neutron distribution $\rho_n(r)$ can be deduced[1] from the relation:

$$\rho_m(r) = \rho_p(r) + \rho_n(r) \ , \tag{1.1}$$

where all densities are normalized to the corresponding number of nucleons. The first moments[2] of these density distributions are related through:

$$\begin{aligned} R_m^{rms} &= \left(\frac{Z < R_p^{rms2} > + N < R_n^{rms2} >}{A} \right)^{1/2} \text{, where} \\ R^{rms} &=< R^2 >^{1/2} = \left(\frac{\int_0^\infty r^2 \rho_(r) 4\pi r^2 dr}{\int_0^\infty \rho_(r) 4\pi r^2 dr} \right)^{1/2} , \end{aligned} \tag{1.2}$$

replacing $\rho(r)$ with the corresponding density.

In general, the density distributions (1.1) have non spherical components which should be included when complete information about the nuclear sizes and shapes is sought. The discussion in this thesis is restricted only to spherical density distributions and some experimental methods to derive them, in particular for exotic nuclei.

The basic and relatively easy method used for determination of the nuclear matter radius of unstable nuclei is the measurement of the total interaction cross section σ_I which is defined as the total cross section for nucleon removal from the incident nucleus [5]. At intermediate energies the effective radius (interaction radius) for the nucleus-nucleus collision can be defined in a simple geometrical picture as:

$$\sigma_I = \pi (R_p + R_t)^2 \ , \tag{1.3}$$

where R_p and R_t are the interaction radii of the projectile and target nuclei, respectively. The separability of the projectile and target radii assumed in the above equation can be proven by performing measurements with different targets. Using Glauber-type calculations, the interaction radius is connected to the root mean square radius R_{rms} [5].

[1] Throughout this work point density distributions are regarded (in a point distribution the nucleons are regarded as point-like particles and are assumed to have no intrinsic density distribution). To obtain the real (folded) radius it has to be folded with the size of the nucleon. The relation between the folded and unfolded radii is: $\sqrt{< r^2_{folded} >} = \sqrt{< r^2_{unfolded} > + < r^2_{nucleon} >}$

[2] The first moment corresponds to the root mean square radius (*rms*)

The momentum distributions of the fragments from break-up reactions give information about the nuclear size and the spatial extent of the valence nucleons. The width of the transverse momentum distribution of the valence nucleons is related to the spatial extent and the binding energy of the valence nucleons around the core in agreement with the uncertainty principle [5].

The wave function of the valence nucleon/s at large distances is of Yukawa type and has the form (1.4) with R being the width of the potential [5].

$$\psi(r) = \left(\frac{2\pi}{\kappa}\right)\left[\frac{e^{\kappa R}}{(1+\kappa R)^{1/2}}\right]\frac{e^{-\kappa r}}{r} \tag{1.4}$$

The inverse decay length κ determines the slope of the density tail and is related to the nucleon/s separation energy S_n via:

$$\kappa = \frac{\sqrt{2\mu S_n}}{\hbar} \ , \tag{1.5}$$

where μ is the reduced mass of the system. From this wave function the density distribution can be written as:

$$\rho(r) = |\psi(r)|^2 \ . \tag{1.6}$$

The momentum distribution of the valence nucleon is given by the Fourier transform of the nucleon wave function (1.4) and is equal to:

$$f(p) = C_1 \frac{1}{p^2 + \hbar^2\kappa^2} \ , \quad \text{with} \quad \hbar^2\kappa^2 = \frac{\Gamma^2}{4} \tag{1.7}$$

where C_1 is a normalization constant and p is the Cartesian momentum of the nucleons and Γ is the FWHM of the momentum distribution. Conclusions about the spatial extent of the tail in the nuclear density can be made as this transformation directly reflects the Heisenberg uncertainty relation – narrow momentum distributions correspond to large radii and vice versa.

With these relations, the properties of the valence nucleons are deduced from the experimentally measured momentum distributions and the *rms* radius of the nucleus R_{rms} is calculated via:

$$< R^2 >= \frac{\hbar^2}{4\mu S_n} = \frac{1}{2\kappa^2} = \frac{2\hbar^2}{\Gamma^2} \ . \tag{1.8}$$

Such calculations are only true for valence particles with orbital angular momenta $l = 0, 1$ [6].

More detailed information about the structure of the nucleus can be obtained via measuring the differential cross section for proton elastic scattering. The intermediate energy proton elastic scattering is a well-established method for studying the structure of stable nuclei [7] and was recently successfully applied for the investigation of the radioactive isotopes of ^{6,8}He [8, 9, 10] and ^{8,9,11}Li [11] (Fig. 1.1). This method allows for deducing not only the *rms* radius of the nucleus but also the nuclear matter radial density distribution. A big advantage of the method is that at intermediate energies (~1 GeV) the elastic scattering process is very well

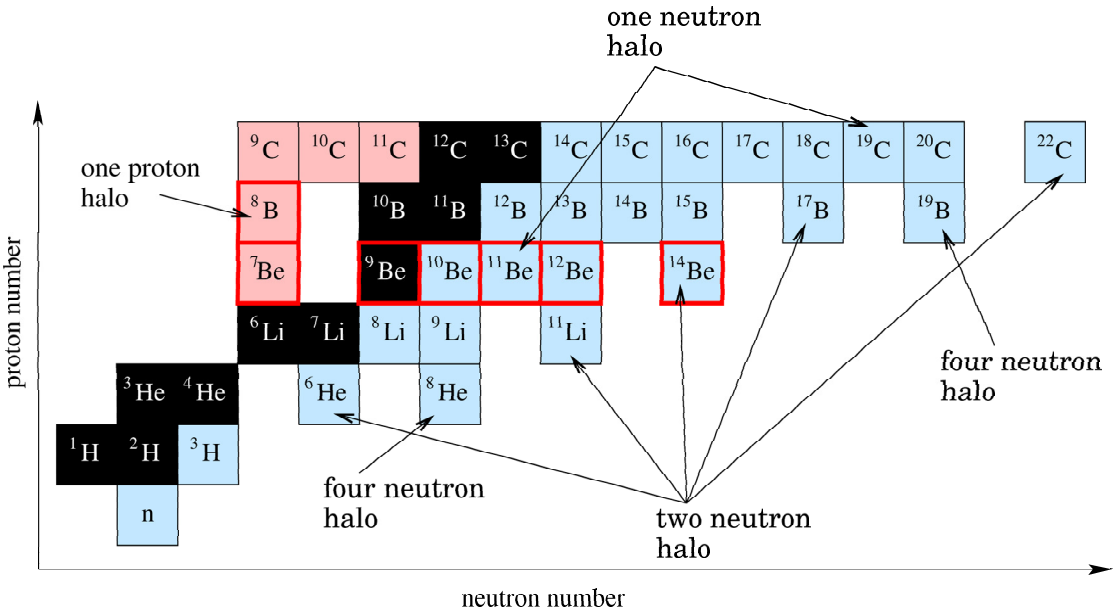

Figure 1.1: Excerpt of the nuclear chart for the light isotopes. Stable nuclei are marked in black, in blue are the β^--radioactive isotopes and in pink – β^+-radioactive ones. Candidates for halo nuclei are indicated. The isotopes studied in the present experiment are marked with red.

understood and there exists a theory, namely the Glauber multiple-scattering theory, which connects in a straightforward way the measured differential cross section and the matter density distribution.

The Glauber multiple-scattering theory describes the differential cross section for elastic scattering based on the assumption that the eikonal and the adiabatic approximations are valid (for details see Chapter 4). The differential cross section is expressed through the free nucleon-nucleon scattering amplitudes folded with the nucleon density distribution. The approach is similar to the description of optical diffraction. The advantage is that relatively small systematical uncertainties are introduced from the theoretical model because the experimental values for the free nucleon-nucleon scattering amplitudes, which are fairly well known, are used. This model also takes into account multiple scattering of the proton in the nucleus. Depending on the choice of parameterization for the nucleon density distribution model dependent or independent results are obtained.

Experiments on cross section measurements at low energies also provide important information about the nuclear structure but they have the disadvantage that the nucleon-nucleon interaction at these energies is not well known and in medium effects and potential scattering make the theoretical interpretation of these data difficult.

1.2 Halo nuclei

Already with the first experimental studies of nuclear radii (e.g (α, α) scattering experiments made by Rutherford) it was discovered that the nuclear radius is con-

nected to the mass number A to a good approximation by the relation:

$$R = r_0 A^{1/3} \tag{1.9}$$

with r_0 ~1.2 fm. When the first secondary radioactive beams were produced at BEVALAC, LBL[3], Berkeley, Tanihata *et al.* made systematic measurements of the total interaction cross sections for various nuclei in 1985 [12, 5]. The results showed unexpectedly large values for the cross sections for some very neutron-rich nuclei which differed substantially from the standard relation (1.9). This phenomenon has been explained as due to an extended nuclear matter distribution consisting of a compact core surrounded by a low-density halo of loosely bound valence nucleon/s. Nuclei with such structure are called *halo nuclei*. The most famous example of a halo nucleus is the isotope ^{11}Li (Fig. 1.2). This nucleus has a halo radius of 5.98(32) fm [11] which is almost equal to the matter radius of ^{208}Pb (6.58 fm [7]), even though the latter has about 20 times more nucleons. In the case of halo nuclei, the nuclear radii differ substantially from the classical formula (1.9). In Fig. 1.1 the halo nuclei which are subject of investigation in the last decades are shown on the chart of the nuclides.

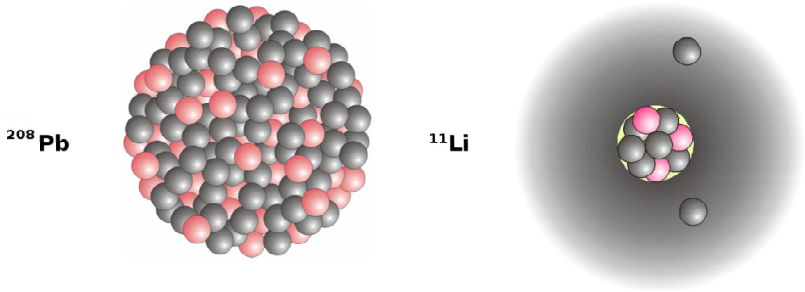

Figure 1.2: Schematic view of the density distributions of the nuclear matter for stable nucleus (^{208}Pb) and extremely neutron-rich nucleus (^{11}Li) [13].

The nuclear halo is a quantum effect and is explained as a result of the combined impact of the small binding energy of the valence particle/s and their low angular momenta ($l = 0, 1$) [14, 15, 16, 17]. To distinguish a halo from other spatially extended system two constraints must be fulfilled. First, the total many-body wave function must have a cluster structure, so that a core and one or more halo components can be found. Second, a large part of the wave function for the halo particles must be in the classically forbidden region outside of the nuclear potential (normally, a probability of at least 0.5 is assumed as a large part).

The density distributions of nuclei far from stability are generally not very well known. For the understanding of the nucleon-nucleon interaction the description of these nuclei is of high importance as it can test the theoretical models for asymmetric nuclear matter and its isospin dependence. Of special interest are the so called

[3]Ernest Orlando Lawrence Berkeley National Laboratory, Berkeley, CA, USA

Borromean[4] halo nuclei (which are composed of a core plus two valence neutrons) where the nucleon-nucleon correlations play an important role and can be exclusively studied.

1.3 Motivation

The nuclear matter density distributions and the nuclear matter radius are important parameters in the description of the complicated relations among the constituents of the nuclear matter. Microscopic models which describe the density distributions permit to study the interactions between the nucleons. Nowadays, these calculations are limited to the lightest nuclei with $A \leq 12$. Thus, experimental investigation of the nuclear structure of heavier exotic nuclei is very important for expanding the knowledge about the nuclear matter and its correct theoretical description. The aim is to have a model which can describe "normal" as well as exotic nuclei in the same framework.

The experiments with exotic nuclei are challenging because of the specific techniques required due to the low intensity with which the nuclei are produced and their short lifetime. First of all, it is impossible to make a target of short-lived nuclides, therefore, the experiments must be performed in inverse kinematics. In this case a beam of radioactive nuclei is produced and it interacts with a stable target (in the case of the present experiment with a hydrogen target). This requires some advanced experimental techniques. Second, the secondary beams of radioactive nuclei have low intensity which demands longer data taking and/or very thick targets and large detection solid angles, and for some of the experimental methods even makes it impossible to perform the analysis due to insufficient statistics. Very effective at low momentum transfer measurements is the use of an active target which provides a full solid angle coverage and a relatively thick target with low detection threshold. For halo nuclei investigations this is of particular importance, as the low momentum transfer region is sensitive to the halo part of the nucleus and also can be almost exactly theoretically described as the nuclear density of the halo is very small which makes the in medium nuclear effects and the contribution of the multiple scattering small or even negligible.

The isotope ^{14}Be is known to be a Borromean two-neutron halo nucleus. Its halo structure was first discovered in interaction cross section [19] and fragments' momentum distributions [20] measurements. The low two-neutron separation energy (S_{2n}=1.34 MeV) which is a condition for the existence of a halo is also observed. Later, experiments on total reaction [21] and interaction [22] cross sections measurements confirmed the halo structure. The halo configuration of ^{14}Be is accepted to be ^{12}Be core plus two valence neutrons but a configuration with four halo neutrons also cannot be excluded. In a number of theoretical calculations the wave functions of the valence neutrons were studied [23, 24, 25]. The effects of a low-lying $\nu 1s_{1/2}$

[4]The Borromean rings are the heraldic symbol of the Borromeo family, which can be found carved on their castle on an island in Lago Maggiore in Northern Italy. The three rings are interlocked in such a way that if any of them were removed, the other two would also fall apart [18]. The 3-body quantum analog is one where the 3-body system is bound, but where none of the two-body subsystems are bound, hence, the name of the *Borromean halo nuclei*.

orbital [24, 25] on the structure of the nucleus and the clustering effects [23, 26] were investigated. A considerable occupancy of the intruder orbital is expected as compared to the standard shell-model ordering where the neutrons should be on the $\nu 0d_{5/2}$ orbital. Several experiments were performed to study this structure which gave controversial results about the amount of mixing [27, 28, 29, 30]. Experimental information about the matter density distribution will be useful to compare with the theoretical calculations and get a deeper insight in the structure of the ^{14}Be nucleus.

The nucleus ^{12}Be is supposed to be the core of the halo nucleus ^{14}Be which alone makes it interesting enough to study its structure. Another interesting aspect is the expected breakdown of the shell structure and disappearance of the $N = 8$ magic number for the neutrons. Details on the experimental investigations of the shell gap reduction can be found in [31, 32, 33, 30]. Several measurements of the radius of ^{12}Be have been also carried out [19, 20, 21]. Theoretical calculations which study the mixing with the intruder orbitals from the *sd* shell also exist. Clustering structure [34, 23, 26] or few-body structure with a ^{12}Be composed from a ^{10}Be core plus two valence neutrons [25, 24] have been investigated as well. The valence neutrons' wave function depends on this structure and the size of the nucleus is strongly affected, respectively. The mixing with the intruder *sd* configuration and the relatively low two-neutron separation energy (S_{2n}=3.67 MeV) may lead, though not to a Borromean halo, to an extended matter distribution. Additional information about the density distribution, not only the matter radius will be very useful for a better understanding of the structure of ^{12}Be.

One of the candidates for a proton-halo nucleus is ^{8}B. The experimental results for its structure are somewhat controversial. Depending on the experimental method and the energy of the incident beam different results are obtained. Measurements of the total interaction and reaction cross sections at energies above $\approx$ 140 MeV/u did not give evidence for an extended matter distribution in ^{8}B [35, 36, 37], while later measurements of total reaction cross section at 20-60 MeV/u were interpreted as evidence for a long low-density tail in the density distribution [38]. The measurements of the momentum distributions of the break-up fragments show narrow peaks which also supports a halo structure [39, 40]. A proton halo has not been investigated with small angle proton elastic scattering up to now and such study will give important information about the structure of the ^{8}B nucleus.

From the above considerations it is clear that the investigation of neutron- and proton-rich nuclei is particularly important for the understanding of the nuclear matter and the evolution of shell structure away from the β-stability and close to the drip lines. In the present experiment the differential cross sections for small angle proton elastic scattering on light exotic nuclei were measured in inverse kinematics. The isotopes ^{7,9,10,11,12,14}Be and ^{8}B (Fig. 1.1) were investigated with the main interest focused on the very neutron-rich ^{14}Be nucleus, which is assumed to have a two-neutron halo structure, the nucleus ^{12}Be (supposed to be the core of ^{14}Be) and the proton-rich isotope ^{8}B which is a candidate for a proton halo nucleus. The aim of the work is to determine the nuclear matter density distributions of the investigated nuclei which is one of their basic properties. In this thesis the experimental results on the isotopes ^{12}Be and ^{14}Be will be presented together with their theoretical interpretation in the frame of the Glauber multiple-scattering theory. A comparison

with several theoretical microscopic calculations will be also made. Some preliminary results for the nucleus ^{8}B and their interpretations will be displayed as well.

At the future FAIR facility radioactive beams with high intensity (several orders of magnitude higher than the one available in GSI) will be produced [41, 42]. Within the EXL project for FAIR a universal detector system is being developed with the purpose to study the structure of exotic nuclei via light-ion induced reactions [43, 44]. The EXL setup will be installed at the NESR at FAIR. The usage of storage ring techniques gives the possibility to perform high luminosity and low background experiments. This setup can be also used to investigate matter distributions in nuclei using proton elastic scattering [45]. It has the advantage that also heavy isotopes can be studied which is not the case with the present IKAR setup. With it only isotopes up to carbon can be studied due to the increased multiple Coulomb scattering of the projectiles which makes impossible the determination of the scattering angles with the necessary accuracy and the increased energy loss of the projectiles in the detector which hinders the high resolution measurements of the protons' recoil energies.

To check the feasibility of the EXL detector setup a test experiment was performed at the existing experimental storage ring ESR at GSI. Small solid angle detectors representing all the systems in EXL were installed and the system was tested with a stable ^{136}Xe beam. Results from this experiment will be also presented.

CHAPTER 2

Experimental techniques

The S247 experiment was performed at the GSI (GSI Helmholtzzentrum für Schwerionenforschung GmbH) accelerator facility (see Fig. 2.1) in Darmstadt [46], in two runs in the years of 2005 and 2006. In this experiment, the absolute differential cross sections for proton elastic scattering on the ^{7,9,10,11,12,14}Be isotopes and on ^{8}B at low momentum transfer (small scattering angles) were measured.

When it comes to experiments with exotic nuclei, fulfilling the experimental demands is a challenging task and special experimental techniques have to be used. As the exotic nuclei have very short lifetimes it is not possible to produce targets from them. Thus, the method of inverse kinematics has to be used to perform the experiment. This means that the roles of target and beam are interchanged and a beam of the radioactive ions impinging on a stable target is used. The production of radioactive beams itself is a complicated and challenging task and usually the produced beams have relatively low intensity and may also contain contaminations from other isotopes. The low beam intensity can be compensated with the use of a very thick active target. The active target method (where the target medium is simultaneously used as a detection medium) is particularly useful when the measurement is performed at low recoil energies as there is no low energy cut off due to events which could not leave the target to reach the detector. Another advantage of the active target is the fact that it covers the full solid angle of interest. This makes the active target method highly effective for the investigation of small angle proton scattering in inverse kinematics with radioactive beams.

2.1 Beam production

For the radioactive beam production two primary beams were used. The ^{12}C ion beam was produced with the ECR ion source at the high-charge state injector (HLI) and the ^{18}O was produced using the MEVVA (MEtal Vapour Vacuum Arc) source which delivers high intensity beams (during the experiment intensities from 10^{8} up

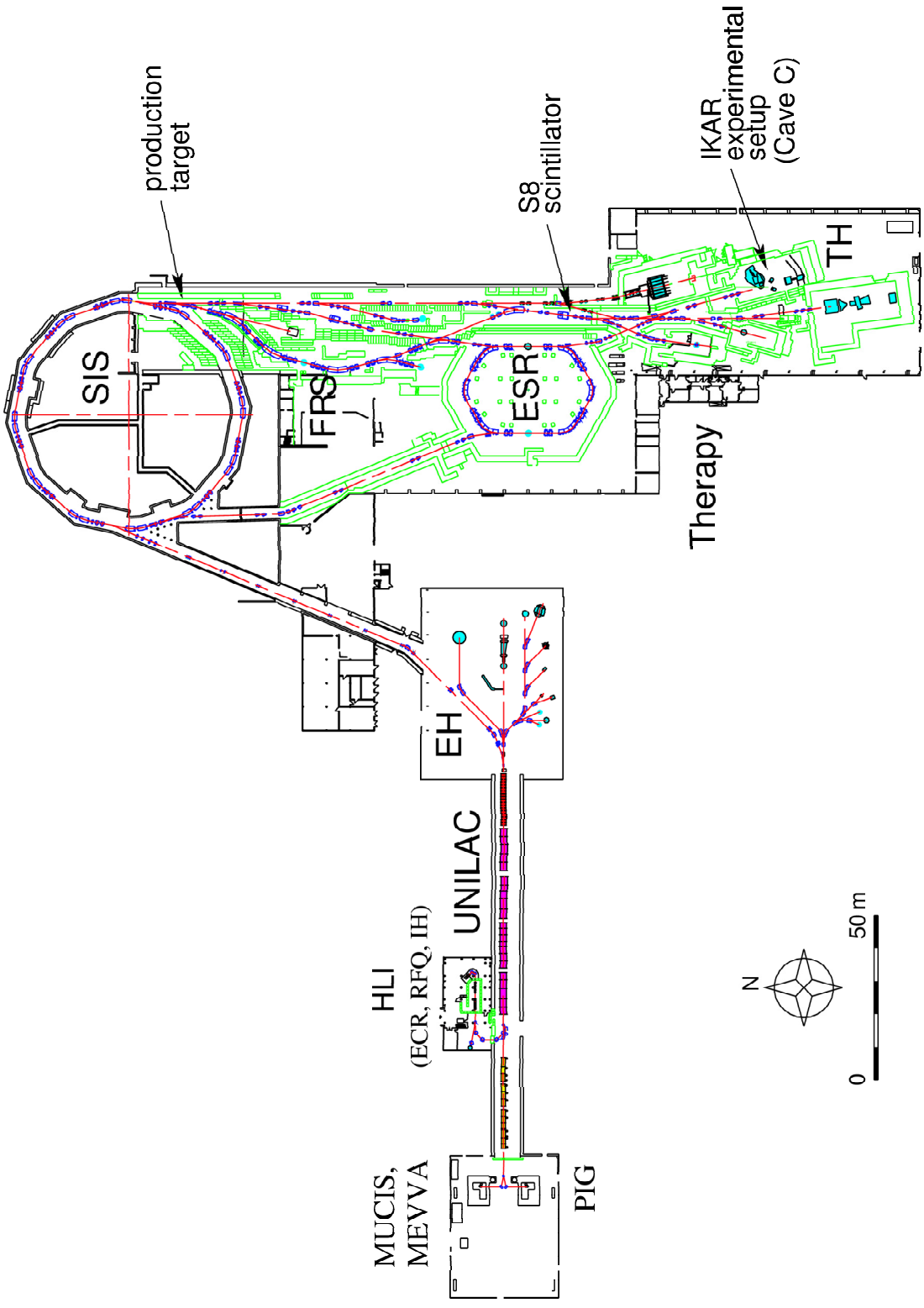

Figure 2.1: GSI accelerator facility. The beam is accelerated in the UNILAC and SIS accelerators. At the entrance of the fragment separator FRS it interacts with a Be production target. The produced fragments are separated in the FRS and the secondary beam of exotic ions is delivered to Cave C where the experimental setup is placed.

to 10^{10} part./s were used). The beams were accelerated to relativistic energies of about 750 MeV/u with the UNILAC accelerator (UNIversal Linear ACcelerator) and the heavy-ion synchrotron SIS (SchwerIonen Synchrotron) (detailed parameters for the beam production are given in Table 2.1). Using the slow extraction mode, when the desired energy is reached in the SIS, the beam is extracted during a time interval from one to ten seconds, which results in a typical uniform structure of the beam bunch. The beam is then directed to a beryllium production target with a thickness 8000 mg/cm^2 located at the entrance of the FRagment Separator (FRS) [47, 48].

Primary beam	E_{prim}, MeV/u	Degrader, mg/cm^2	Second. beam	E_{sec}, MeV/u	Intensity, part./s	Contamination, %
^{12}C	769	2000	^{7}Be	700(8)	3300	0.3
	779	2700	^{8}B	701(8)	2500	2.7
	764	5000	^{9}Be	700(8)	6000	0.5
	745	–	^{10}Be	702(8)	4700	6.5
^{18}O	762	5000	^{11}Be	700(8)	6000	1.5
	759	5000	^{12}Be	701(8)	5600	1.1
	744	1000	^{14}Be	700(8)	3200	25

Table 2.1: Parameters of the primary and secondary beams and the production setup. The degrader thickness is optimized for maximum secondary beam intensity and minimum contamination. The primary beam energy is chosen such that the secondary beam energy at the center of the IKAR detector equals 700 MeV/u. The σ of the spread in energies for the secondary beam is given in brackets. In all cases the thinest possible degrader was used to reduce the spread in energies.

At relativistic energies the reaction mechanism is considered to be "pure" projectile fragmentation [49]. An advantage of this reaction mechanism at high energies and using heavy-ion beams is that the reaction products are confined to forward angles and have velocities close to that of the primary beam, which allows to produce good quality beams of radioactive nuclei. Depending on the impact parameter projectile fragmentation occurs for peripheral collisions and multi-fragmentation in the case of central collisions. The fragmentation is a two-step process described by the abrasion-ablation model [49]. For a given impact parameter, the nucleons which are located in the geometrical overlap of the two interacting particles are called *participants* (Fig. 2.2). These are the nucleons which interact during the reaction. The nucleons outside the interacting region are called *spectators*. After the abrasion most of the participants leave the collision region. This process is fast and occurs within 10^{-21} s. The target spectators are nearly at rest while the projectile spectators continue with almost the incident particle velocity. They constitute the *prefragments* which further undergo statistical evaporation (ablation) of particles, clusters or fission fragments. The second step is slow and takes about 10^{-16} s. The produced final fragments are then separated in the FRS.

The FRS is an achromatic magnetic forward spectrometer [50, 51]. It can separate all kinds of exotic beams in-flight by a combination of ion optic devices and a passive degrader. The FRS facility consists of four 30° dipole magnets placed symmetrically to a dispersive intermediate focal plane and a number of quadrupole

and hexapole magnets (Fig. 2.3). The quadrupoles placed in front of each dipole are used to achieve high resolving power and a good transmission by properly illuminating the field volume of the bending magnets. Quadrupoles placed after the dipole magnets determine the focusing conditions at each focal plane. Hexapole magnets placed before and after the dipoles are used for second order aberration corrections. The isotope separation is based on magnetic analysis combined with energy loss in matter ($B\rho - -\Delta E - -B\rho$ selection). Heavy ion beams with magnetic rigidity $B\rho$ from 5 to 18 Tm can be analyzed by the device.

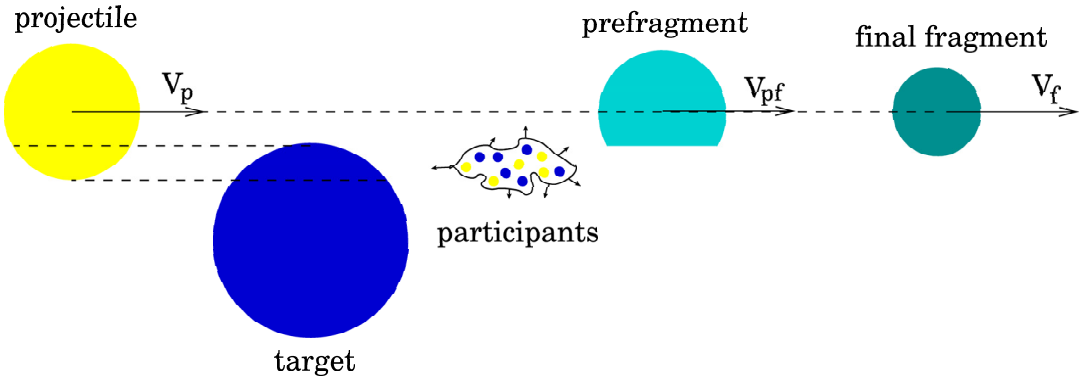

Figure 2.2: Projectile fragmentation at relativistic energies. The particles which are located in the region of geometrical overlap of the projectile and target nucleus interact during the reaction (participants). The nucleons outside the interacting region are called spectators. The final fragments have velocities close to that of the incident beam particle.

The motion of a particle with momentum p in a magnetic field B is described by the Lorentz force. Thus, for the particle motion the following equation is obtained:

$$B\rho = \frac{p}{q} , \tag{2.1}$$

where ρ is the radius of the trajectory of the particle and q is its charge. The ratio p/q is called magnetic rigidity and is characteristic for a particle with certain mass, charge and velocity. At relativistic energies the fragments are fully stripped and therefore $q = Ze$, where e is the elementary charge. Their momentum is $p = \beta\gamma Auc$ with $\beta = v/c$, $\gamma = \sqrt{1/(1-\beta^2)}$, u is the atomic mass unit and c is the velocity of light. In this case equation (2.1) transforms to

$$\frac{A}{Z} = \frac{eB\rho}{\beta\gamma cu} . \tag{2.2}$$

In the first stage of the analysis isotopes with the same A/Z are selected, according to Eq. (2.2). Heavy-metal alloy slits are used to remove the parts of the beam with A/Z different from the selected one. An Al wedge degrader is placed at the central dispersive focal plane F_2 of the FRS (Fig. 2.3). Isotopes with the same magnetic rigidity which have passed the A/Z selection are focused on the same position of the energy degrader. They lose momentum in the degrader according to their charge Z and mass A (Bethe-Bloch formula [52]). At the end a second stage $B\rho$ selection is applied and the particles are separated according to their different

velocities. The mean thickness of the degrader and the $B\rho$ settings of both separator stages define the mass A and the charge Z of the fragment which is selected.

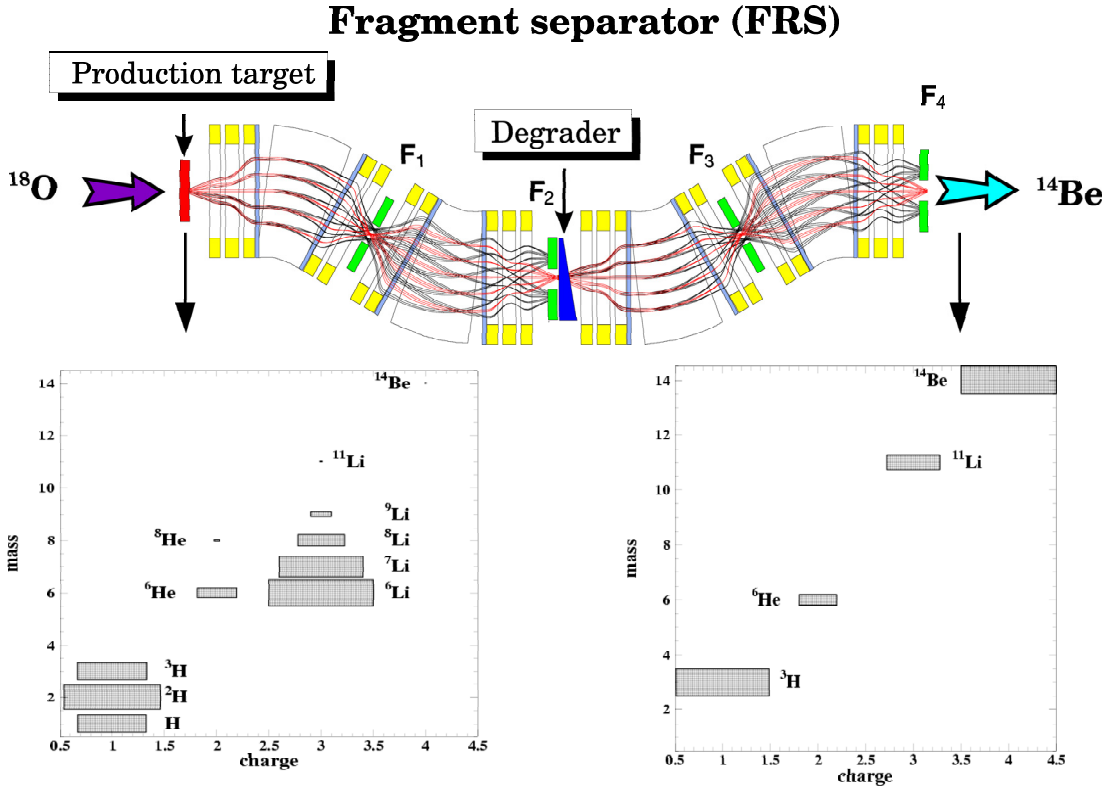

Figure 2.3: Setup of the fragment separator ion optics. The path of the projectiles with different A/Z ratio is schematically shown and the selection is marked (with red the path of the selected ions is marked, in black are the fragments which are separated with the Bρ selection). On the A vs. Z plots the isotopic composition of the beam after the target and at the end of the FRS are shown. The size of the squares represents the corresponding intensity of the isotope.

The simulation for the settings of the fragment separator and the optimization for the beam production was done with the MOCADI program [53]. The program calculates the transport of particles through ion optical systems and layers of matter. For each isotope simulations with different degrader thicknesses were done in order to choose the one which gives the best values for the intensity of the primary fragment and the contamination from other isotopes in the secondary beam. The very exotic nuclei, as in our case, have larger fragmentation probability when interacting with matter. Thus, a thinner degrader was necessary in order to achieve higher transmission of the isotope of interest which leads to a not very "clean" secondary beam. Whenever it was possible no degrader was used as it makes the spread in the beam energies higher (e.g. in the case of ^{10}Be). The quality of the isotope separation as calculated from MOCADI is shown in Fig. 2.4. The example is for the case of ^{14}Be beam production. In this case the largest contamination from other isotope was observed which is due to the fact that a very thin degrader had to be used in order to obtain reasonable intensity for the ^{14}Be beam which has very high break-up cross section. The produced secondary beams had intensities of several

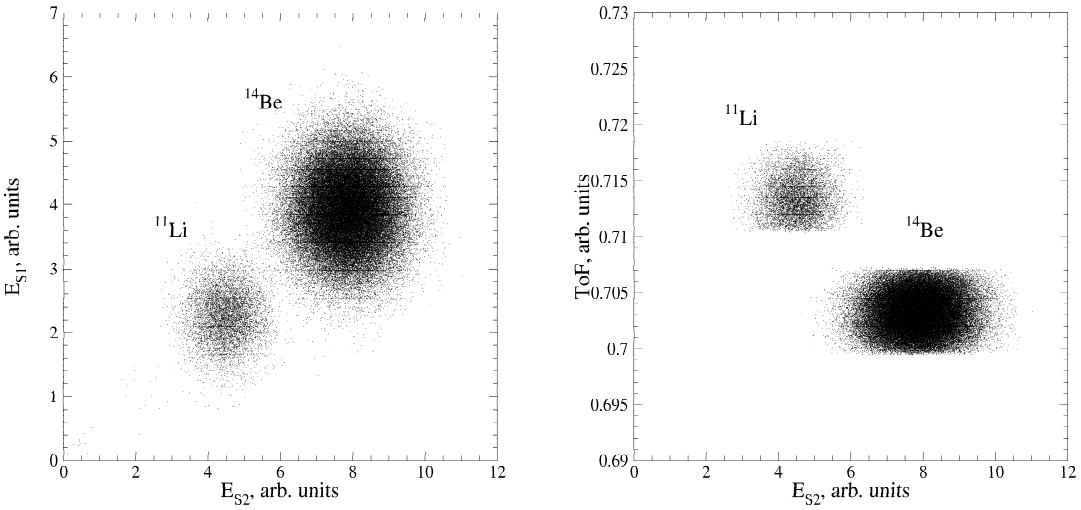

Figure 2.4: Beam composition and quality of the isotope selection obtained with the MOCADI simulation. The settings for the FRS are chosen for the production of ^{14}Beam. The sharp cuts of the ToF values are due to the acceptance of the dipole magnets which is the limit in the simulation (in experiment the limit is the resolution of the detector).

thousands particles per second (Table 2.1). The additional isotopes in the beam were separated in the off-line analysis. In the simulation the energy of the primary beam was chosen such that the energy of the secondary beam in the center of the IKAR detector was 700 MeV/u for all isotopes. It is important to note that later in the analysis of the experimental data the equivalent proton energies for the case of "normal" kinematics are used. During the experiment about 10^5 elastic scattering events for each isotope were collected.

2.2 Experimental setup

A schematic view of the experimental setup is shown in Fig. 2.5. The main part of the setup was the time projection ionization chamber IKAR which was used as an active target. Additionally, four multi-wire proportional chambers (MWPC) were installed, two of them placed before IKAR and two after it. They were used for tracking of the projectiles and determination of the projectile scattering angle. The MWPCs were also used to adjust and monitor the beam profile and to determine the positions of the chambers relative to each other. Between the first two and the second two MWPCs there were bags filled with He gas used to minimize the interaction of beam particles with matter and thus, reduce the multiple Coulomb scattering. The energy loss in the three scintillators S1, S2 and S3 together with an information about the time of flight between the S8 scintillator, placed at the end of the FRS (see Fig. 2.1), and S1 were used for projectile identification. The signals from S1, S2 and S3 were also used for a fast trigger signal. A VETO scintillator was placed at the entrance of IKAR to limit the accepted beam size and was also included

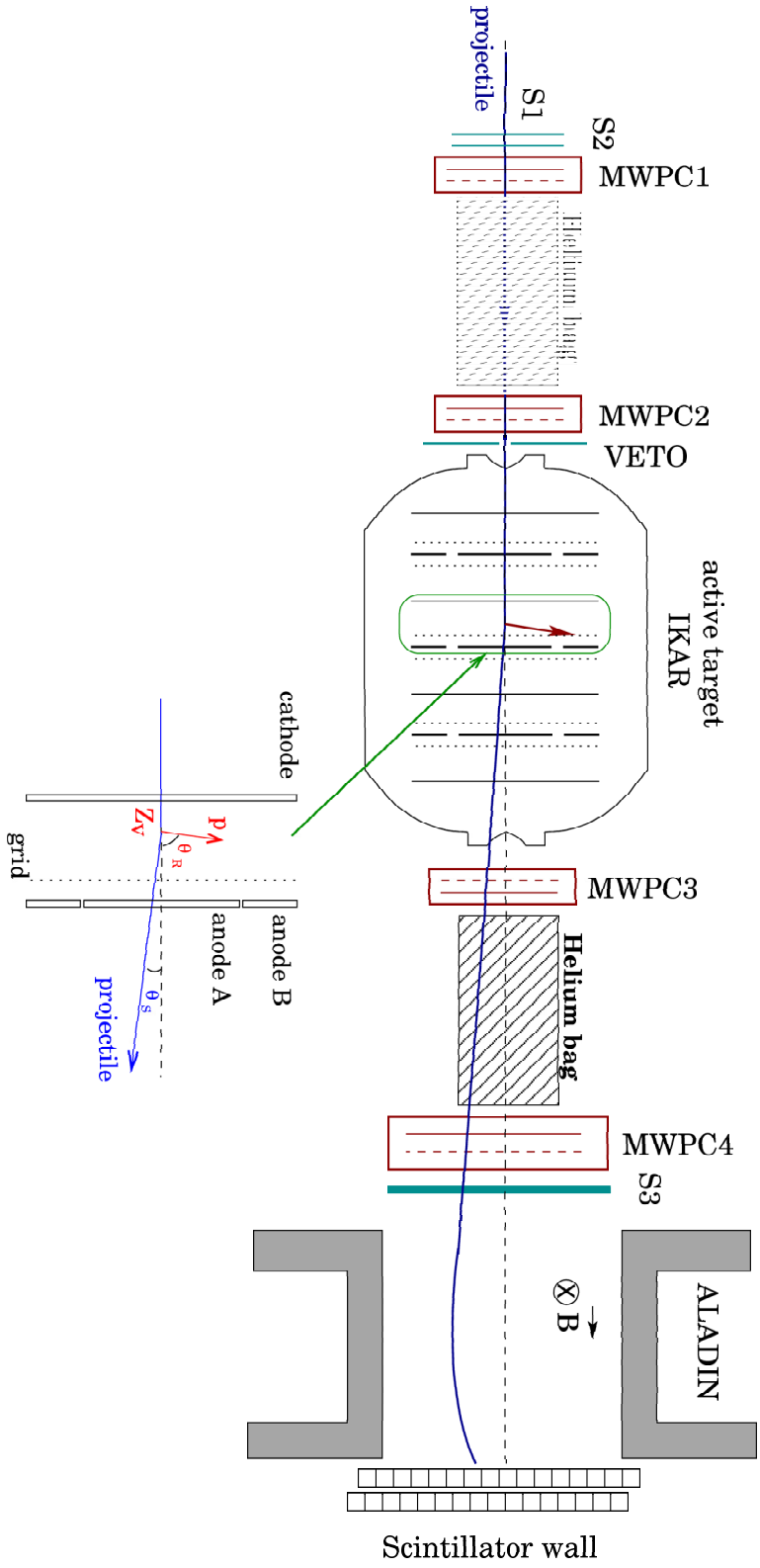

Figure 2.5: Schematic view of the experimental setup for small angle proton elastic scattering on exotic nuclei in inverse kinematics. The central part is the ionization chamber IKAR, simultaneously used as a gas target and recoil proton detector. The four multi-wire proportional chambers MWPC1–MWPC4 determine the scattering angle of the projectile θ_s. He bags were placed between them to reduce the multiple Coulomb scattering of the projectiles. The scintillators S1–S3 and VETO are used for beam identification and triggering. The ALADIN magnet and the position sensitive scintillator wall are used for break-up reaction channels discrimination.

in the first level trigger. At the end of the setup was the large acceptance magnet ALADIN with a position sensitive scintillator wall placed after it. With their help projectiles which undergo reactions on their path through the experimental setup are discriminated using their different magnetic rigidity ($\sim A/Z$) and energy loss in the scintillators ($\sim Z^2$). With this experimental setup kinematically complete measurements could be performed.

Major change as compared to the previous IKAR experiments [8, 11] when the neutron-rich He and Li isotopes were investigated is the fact that the experiment was performed in Cave C (old experiments were made in Cave B) where much better transmission from the FRS can be achieved and therefore higher intensity secondary beams are obtained. Another difference are the used MWPCs. The read-out of the current chambers was performed strip-wise and therefore better coordinate determination was possible. The flash ADCs used to read the signals from IKAR were also different with bigger word length and shorter time bit of 40 ns. An effect which worsens the conditions as compared to previous measurements is the fact that due to the higher charge of the projectiles there is a bigger contribution of multiple Coulomb scattering when the beam passes through the setup which makes the determination of the scattering angle θ_s less accurate.

The next sections describe the construction of the detectors used in the experimental setup, while detailed explanation of the procedure for the signal processing and data analysis is given in Chapter 3.

2.2.1 *Design and operating principle of the IKAR detector*

The ionization chamber IKAR[1] is a cylindrically symmetric stainless steel gas detector with a diameter of 70 cm and a length of 160 cm. It was developed in PNPI (Petersburg Nuclear Physics Institute, Gatchina, Russia) [54, 55, 56]. It consists of six identical ionization chamber modules (Fig. 2.6) placed perpendicularly to the axis of the chamber which coincides with the beam axis. At the entrance and at the exit there are semi-sphere shaped Be windows with thickness 0.5 mm and diameter 7 cm through which the beam passes. This shape was chosen in order to withstand the high pressure at which the chamber is operated and tests with overpressure were performed to check the reliability of the construction. During the experiment the chamber was filled with a high purity H_2 gas (less than 1 ppm[2] impurities) with a pressure of 10 bar. For a safe operation of the chamber a special tent was build around it which, in case of a leak, should lead the hydrogen gas out of the building to prevent the build up of an explosive mixture. An emergency shutdown of the high-voltage supply was included in case this happens. The high operating pressure was necessary in order to achieve a reasonable target thickness and it was constantly measured during the experiment with a high precision manometer. Depending on the recoil angle a target thickness of 7.513 mg/cm^2 (for 500 keV protons) to 5.089 mg/cm^2 for 30 MeV protons was achieved. Even small amounts of electronegative impurities cause a noticeable electron loss on the electron drift path to the anode due to adhesion of the electrons. This adhesion leads to deterioration of the

[1] IKAR – the name comes from the first letters of the Russian translation of "Ionization Chamber for Hadron Scattering".

[2] 1 ppm = 1 foreign particle per 10^6 H atoms

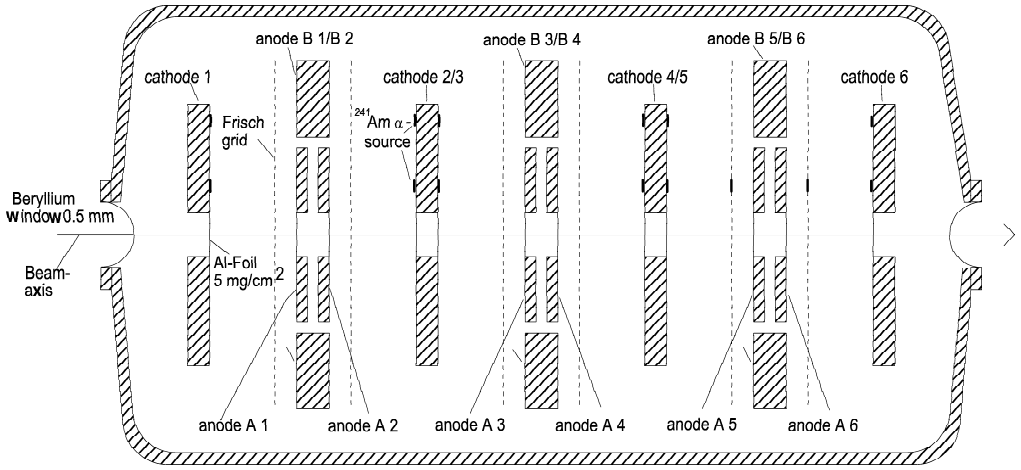

Figure 2.6: The IKAR ionization chamber (Figure from [57]). In six independent sections of this detector the recoil energy T_R, the recoil angle θ_R and the vertex point Z_v are determined. (see also Fig. 2.7).

energy resolution and modification of the energy response. Therefore, high purity gas is necessary to achieve precise measurements of the recoil energy and additional correction for the electron adhesion has to be done. The fluctuation in the number of ion pairs created by the proton has a negligible effect on the energy resolution of the order of 0.1% [58, 54].

Each ionization chamber module is composed by cathode, grid and anode (Fig. 2.7). The anode consists of two parts – inner anode A and outer anode B, all made from

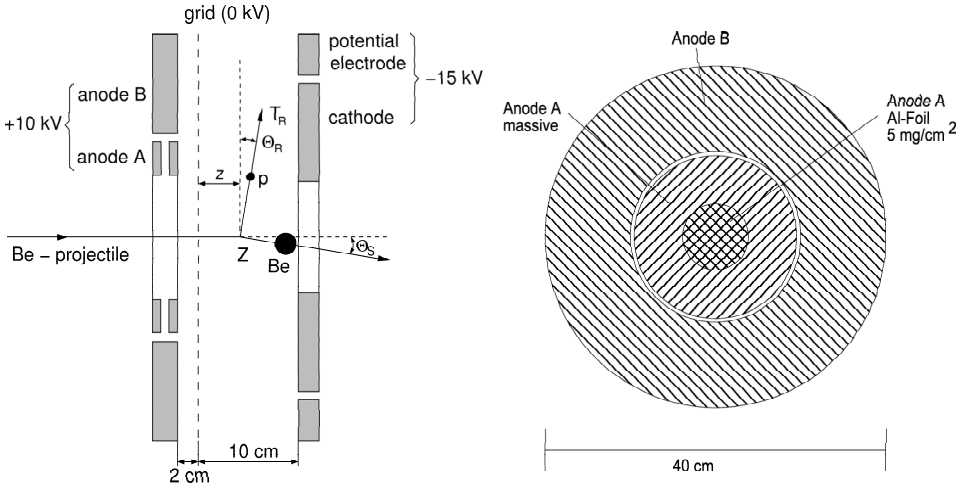

Figure 2.7: Structure of a single IKAR module with a typical scattering event (left). All variables which can be determined with IKAR, namely the recoil angle θ_R, the recoil energy T_R and the vertex point Z_v, are marked in the figure. Scheme of one anode (right). Each anode consists of central anode A, the central part of which is made of thin Al foil in order to reduce the matter with which the beam interacts, and a ring anode B, which is common for each two neighbouring modules. [57].

stainless steel. Anode A has a diameter of 194 mm with a central part made of Al foil with a thickness of 5 mg/cm^2 to reduce the interaction of the beam with matter. Anode B is shaped as a ring with inner diameter 206 mm and outer one 390 mm. Events which happen between the grid and the cathode which are placed at a distance of 100 mm are detected. The distance between the grid and the anode is 20 mm. The operating voltage is +10 kV on the anodes and -15 kV on the cathodes. To keep the number of electrodes relatively small, the cathodes and the B anodes are common for two neighbouring modules. The configuration of modules 2, 4 and 6 is shown in Fig. 2.7. Modules 1, 3 and 5 have a mirror configuration with respect to this one (module six is the first in beam direction). The recoil tracks corresponding to elastic scattering at small angles are almost parallel to the surface of the electrodes. As it slows down, the proton ionizes the gas in the chamber forming electron-ion pairs. The number of ion pairs is proportional to the energy of the recoil proton T_R. The signal is induced on the cathode immediately after the collision when the electrons separate from the ions and start to drift towards the anode plate. The anode signal appears first when the electrons drift through the grid.

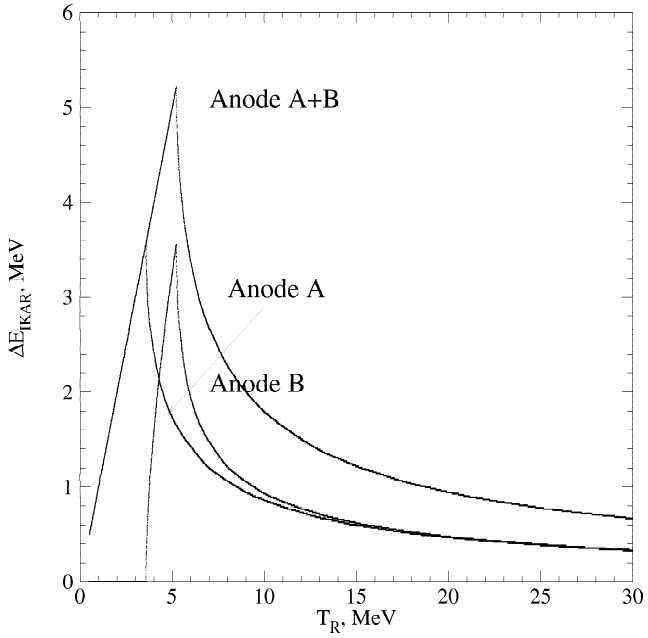

Figure 2.8: Monte Carlo simulation of the signals from elastic scattering events in IKAR as a function of the energy T_R of the recoil proton. Anode A measures full energy up to $E_p = 3.5$ MeV and after that only energy loss as the range of the proton becomes longer than the size of the anode. Up to energy 5.2 MeV the track of the proton fits in the active region of anodes A and B together thus, the sum of their signals gives the full proton energy. Above 5.2 MeV only the energy loss is detected in IKAR.

For the energy calibration of the detector ^{241}Am α-sources are used. On the surface of each cathode two sources were evaporated and in addition in modules 5 and 6 sources were also placed on the grid. The comparison between the signals from the α-particles placed on the grid and the cathode was used to control the amount

of electrons lost due to adhesion on the impurities in the hydrogen gas (mainly O_2 molecules).

The expected pulse-heights on the anodes A and B for elastic scattering events as a function of the proton energy T_R are shown in Fig. 2.8. Protons with energy less than 5.2 MeV are completely stopped in the active volume of IKAR. For an energy $T_R < 3.5$ MeV the range of the proton fits in the area of anode A and signals appear only on it. For $3.5 < T_R < 5.2$ the proton goes beyond the end of anode A and its energy is given by the sum of the signals on anode A and B. For higher energies the protons leave the active volume of IKAR and only the energy loss is detected in both anodes. Besides precise energy measurement, the vertex point of the interaction and the scattering angle of the recoil proton can also be determined with the IKAR detector.

2.2.2 *Tracking detectors*

The MWPCs determine the trajectory of the projectile before and after IKAR. Hence, the scattering angle θ_s of the projectile can be extracted. The baseline of each couple of chambers is 113.5 cm. A schematic view of one plane of the MWPC is shown in Fig. 2.9. Each chamber has two such planes, one in X and one in Y

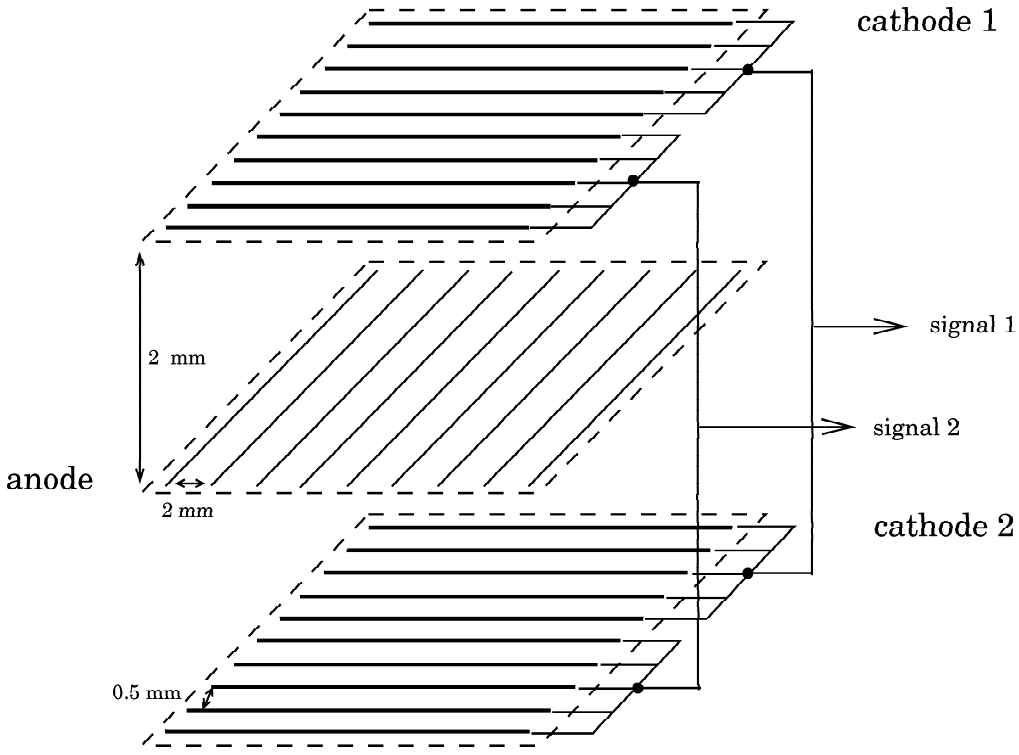

Figure 2.9: Scheme of one plane of a multi-wire proportional chamber. The cathode strips are read-out in groups and the coordinates are determined using the signal amplitudes.

direction. Each plane has two cathode layers and one anode with a 2 mm cathode-anode gap. In the small chambers (MWPC1, MWPC2 and MWPC3), the anode is made of 25 μm wires with spacing of 2 mm, while in the big chamber (MWPC4)

the wires are 30 μm again with spacing of 2 mm. The last MWPC was made bigger in order to provide acceptance for the scattered projectiles. The cathodes are made of 50 μm wires with spacing 0.5 mm. In the small chambers each 5 wires of the cathodes are shortcut and thus, the signal from them is read-out as from 2.5 mm strip. In the big chamber MWPC4 each 6 wires are shortcut which corresponds to a strip width of 3 mm. This is done to reduce the number of electronic channels to be used. The charge on each strip is read-out and then the coordinates in the chambers are determined by analyzing the distribution of the charges on the cathode strips. The first three chambers have 64 strips in each plane while the last one has 86 strips. The windows of the chambers are made from mylar. The chambers are filled with a mixture of 75 % Ar and 25 % CO_2 gases and their working voltage is 1.5 kV. Additionally to the tracking, the proportional chambers were used to adjust and monitor the beam profile.

2.2.3 *Scintillator detectors*

At the beginning of the setup there were two plastic scintillators S1 and S2 with a thickness 1 mm (S1) and 2 mm (S2). They are designed relatively thin in order to minimize the interaction with the beam and gave a fast signal for the trigger (see Section 2.3). They were also used for projectile identification together with the time of flight information from the S8 scintillator in FRS and S1 (see Section 3.1). After the last proportional chamber a third scintillator S3 was placed. It was much thicker than the first two (5 mm) so that a sufficiently good energy-loss signal was obtained and isotope selection was possible.

At the entrance of IKAR a VETO detector was placed. It was a plastic scintillator with 2 mm thickness and a hole with a diameter of 2 cm in the center. The signals were detected with two photomultipliers placed on both sides of the scintillator to avoid loss of events due to the hole in the center. The purpose of the VETO was to limit the size of the accepted beam and angular dispersion and thus to assure that the accepted beam particles are on the axis of IKAR. It was important that the scattering process happens at the axis or as close as possible to it. Otherwise, the energy of the proton would not be determined with sufficient accuracy.

2.2.4 *ALADIN magnet and the scintillator wall*

The ALADIN magnet and the scintillator wall behind it were used to separate the break-up events occurring along the experimental setup from the elastic and inelastic scattering ones (Fig. 2.10). The chamber behind the magnet was not evacuated and the scintillators were operated at atmospheric pressure due to technical problems which did not allow the operation of the photomultipliers in vacuum. This lead to an increased number of break-up events. The position sensitive scintillator wall consists of two layers. Each layer is built by 96 plastic scintillators (BC408) with a 2.5 cm width, 110 cm length and 1 cm thickness positioned in vertical direction behind the ALADIN magnet. The distance between the two layers is about 5 cm. Each scintillator bar is packed in black foil to exclude cross-talk. Each 8 bars are packed together and have a common high-voltage supply. Additionally, a light guide is connected to each scintillator with the purpose to test the system with a laser.

The second layer of the wall is moved with half a bar width aside with respect to the first one in order not to miss events where the particle passes between the bars and to increase the position resolution. The total active area of the detector is 240×110 cm^2. The scintillator wall is placed at an angle 7° with respect to the perpendicular to the beam direction so that the particles hit the scintillators perpendicularly to the surface which makes it easier to determine the coordinate. The signals from each scintillator are detected with two photomultipliers placed on top and bottom of each bar. Via the energy loss in the scintillators the charge Z of the projectile and the x position can be determined. The algorithm for recognizing the events in the scintillator wall was developed by T. Schäfer [59].

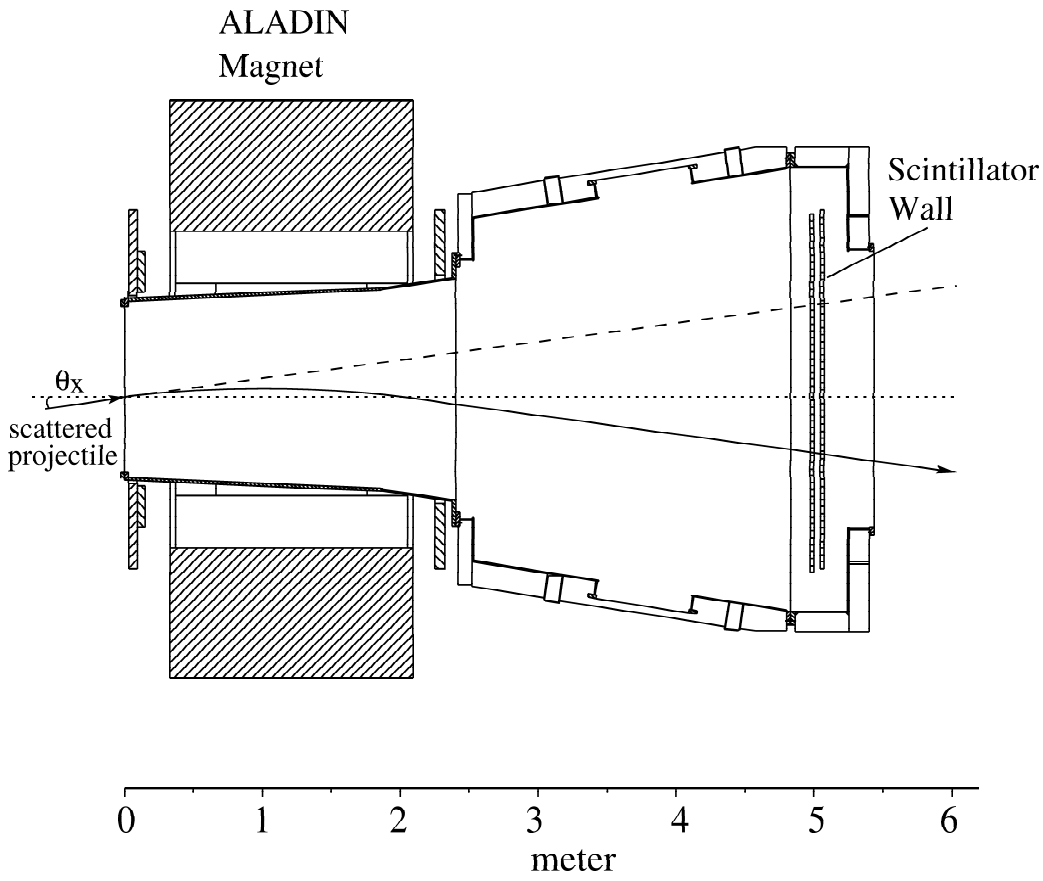

Figure 2.10: The Large Acceptance DIpole magNet (ALADIN) and the scintillator wall. The straight dashed line represents the trajectory of the projectiles with magnetic field off. The solid line is the trajectory of an ion when a magnetic field is applied.

For each isotope, before the actual data taking, a so called "sweep" run was made to calibrate the scintillator detectors in the wall. For this purpose the field of the magnet was changed from 0 to its maximum value of 1.66 T and thus, all possible scintillator bars were illuminated by the beam.

2.3 Electronics and data acquisition

The electronics scheme of the S247 experimental setup is shown in Fig. 2.11. A two level trigger logic was applied in order to write on tape only useful events which have complete information from all detectors and are not affected by pile-up in IKAR which was the slowest detector in the setup. In the first level a coincidence between the scintillators S1, S2 and S3 together with an anti-coincidence with the VETO detector was demanded (T1). The second level trigger contained a check for the presence of a signal in IKAR in a combination with a pile-up protection scheme. This was done by a control unit (CU) with a condition that the time between the current event and the previous one is at least 24 μs. In case a particle comes in the same time window after the current event it is counted as an EKR/LEKR[3] event. Only in case the condition was fulfilled a second level trigger was produced which gave the start to the data acquisition system (DAQ). The DAQ read the information from the flash ADCs (FADC) for IKAR and the MWPCs as well as the signals from all the scintillators, and also scaler values. The used FADCs had a signal length of 32 μs (800 channels). For the read-out of the signals from the MWPCs special preamplifiers GASSIPLEX, developed in CERN, were used [60]. The scalers gave information about the counts in S1, S2, S3, S8 and IKAR, and in addition a clock with a 10 kHz frequency was also connected to it. During the read-out the DAQ sent an inhibit signal to the scalers and they did not count during the dead time. With this trigger conditions the system was working with an average dead time of about 50 %. The relatively big dead time was partly due to the not uniform structure of the spills obtained from the synchrotron by slow extraction which lead to more than one projectile coming in the 24 μs window. For the data acquisition the GSI system MBS (Multi Branch System) was used [61] and the online data monitoring and analysis was performed with the Physics Analysis Workstation PAW [62].

[3]EKR – Event Killed by Rationer which comes in the 24 μs window after a candidate event; LEKR – also event killed by rationer but coming after an EKR event.

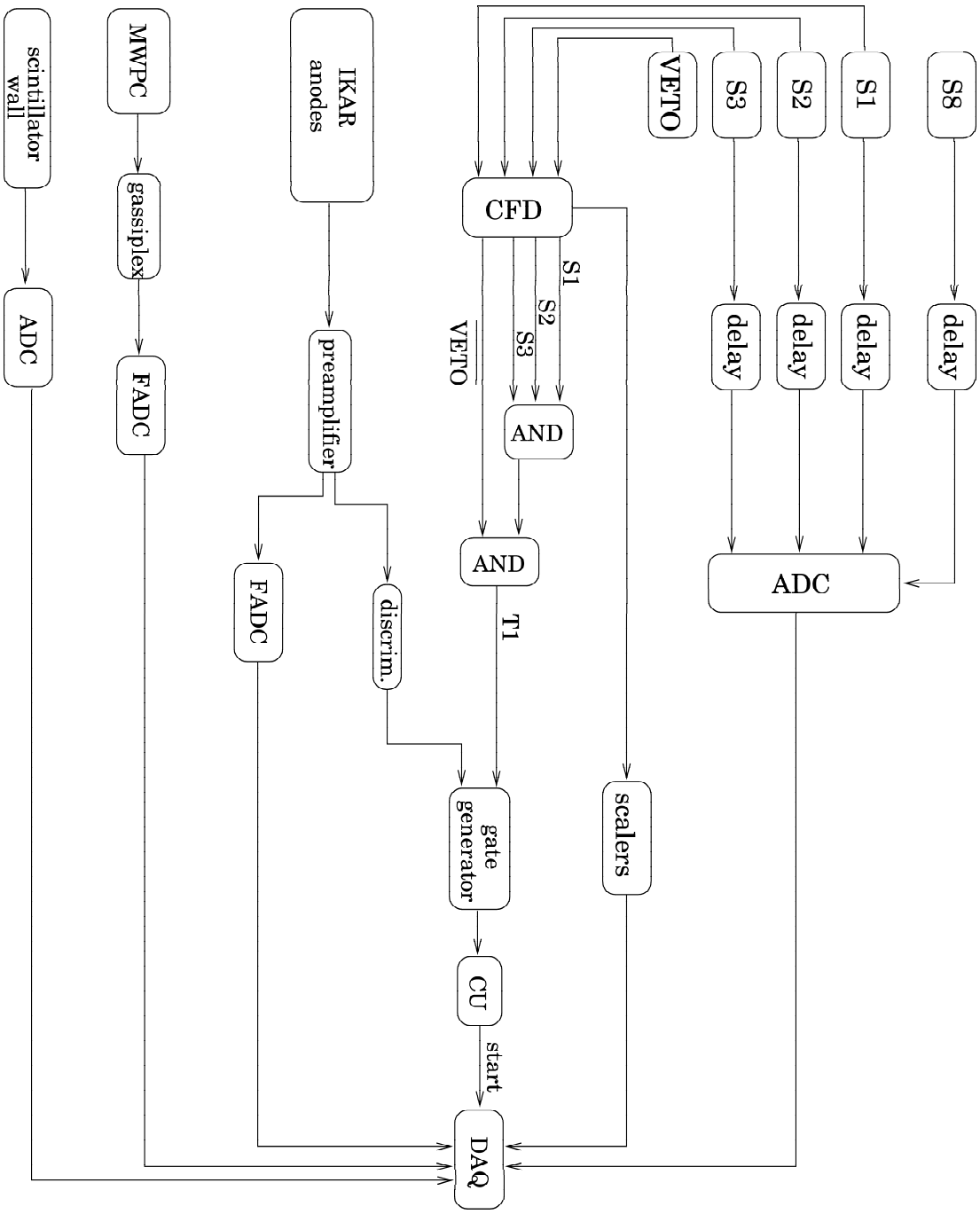

Figure 2.11: Electronics scheme of the IKAR setup. The first level trigger is given by a logical AND from the signals of the scintillators S1, S2 and S3 in an anti-coincidence with the VETO detector. The second level trigger is given by the presence of signal in IKAR. The control unit (CU) provides pile-up protection as described in the text. (CFD means constant fraction discriminator.)

CHAPTER 3

Data analysis

3.1 Isotope identification of the projectiles

The secondary beam produced by the Fragment separator contains other isotopes beside the main one (see Section 2.1). Due to this fact additional projectile identification is necessary. This is done off-line by using the information from the three scintillators S1, S2 and S3 and also information from the FRS about the time-of-flight (ToF) of the projectile. The start signal for the ToF measurement was given from the scintillator S8 at the end of the FRS and the stop was given by a coincidence signal from S1-S2. The flight path is $\approx$ 40 m. Typical ToF for the Be isotopes was 223 ns. In Fig. 3.1 the 2-dimensional plots of the energy loss in the different detectors and the ToF for the case of a ^{14}Be beam are shown. From these correlations the isotopes in the beam can be unambiguously separated. In addition the energy loss in the scintillator S3 was used to make sure that after the target the projectile has the same charge Z. The observed intensities are similar to the expected ones (see MOCADI calculations Fig. 2.4). Similar plots for the identification of the projectiles in the cases of ^{12}Be and ^{8}B beams are shown in Figs. 3.2 and 3.3, respectively. The isotope separation is done on event by event basis.

3.2 Tracking of the projectiles

The particles passing through the proportional chambers ionize the gas inside the chamber which induces a charge on the chamber's strips. The amplitudes of the signals from the strips are used to determine the coordinates of the particles. When the signal is produced by only one particle (Fig. 3.4(A)) the coordinate is calculated using the center of gravity method for three strips [63]:

$$X = W(i_{max} - 0.5) + C_1 \frac{(A_{i_{max}+1} - A_{i_{max}-1})}{A_{i_{max}+1} + A_{i_{max}} + A_{i_{max}-1}} \ , \qquad (3.1)$$

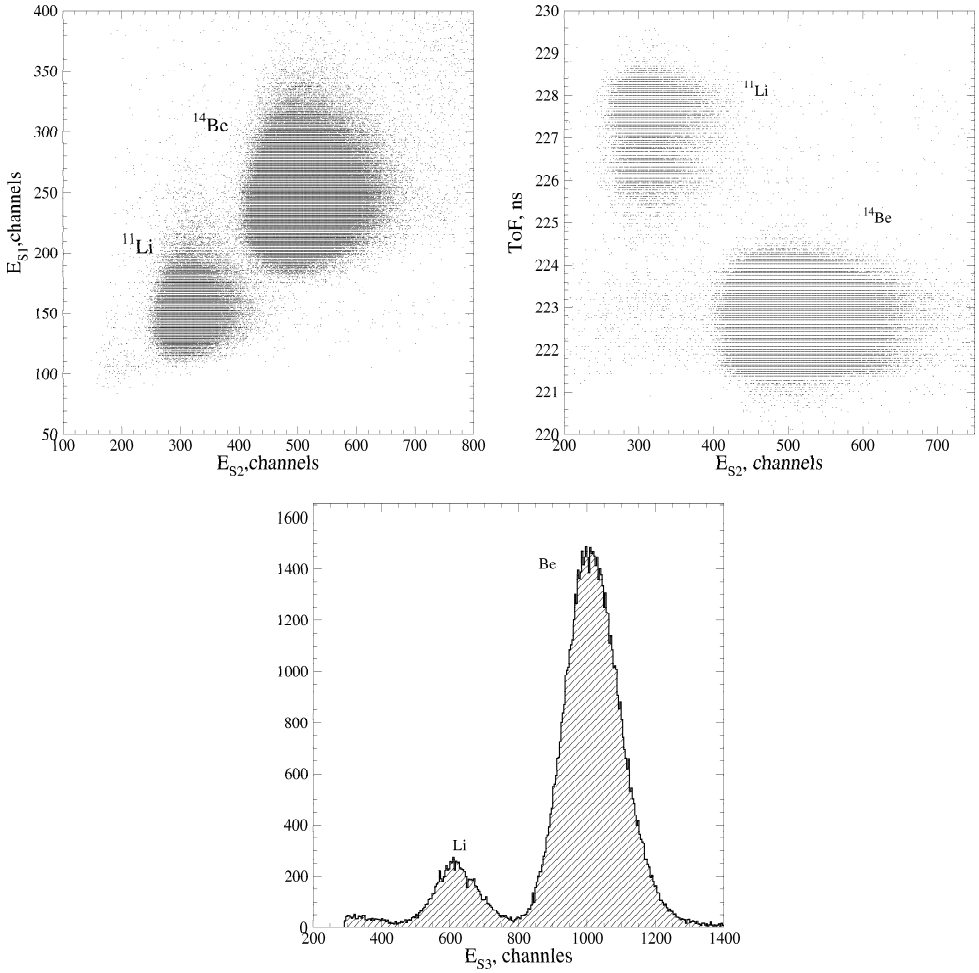

Figure 3.1: 2-dimensional ΔE plot from scintillators S1 and S2 (left), and from the ToF and ΔE from S2 (right). Additionally, the energy loss in S3 (bottom figure) was used to make sure that the projectile had the same charge Z after the target. The given example is for the case of ^{14}Be beam. The ^{14}Be nuclei are clearly separated from the admixtures of ^{11}Li which also pass through the FRS.

where W is the strip width, A_i is the amplitude of the signal on the i^{th} strip and i_{max} is the number of the strip with maximal amplitude. When two particles are hitting the detector at the same time, two different cases are distinguished (Fig. 3.4(B)). Let S be the sum of the amplitudes from the three strips with highest values. In case that the sum for the first particle is at least three times bigger than the same sum for the second particle $S_1 \geq 3S_2$ and their maxima are more than five strips away from each other the same center of gravity method (as discussed above) is used. This condition is applied in order to assure that the particle which coordinate is determined is really the projectile. In case the sums of the amplitudes differ less than three times it is not possible to determine which signal corresponds to the needed projectile particle and which comes from background or noise and such events were neglected. When the maximum of the second signal is closer than five strips to the first one and $S_1 \geq 3S_2$, the coordinates of the particles are found by

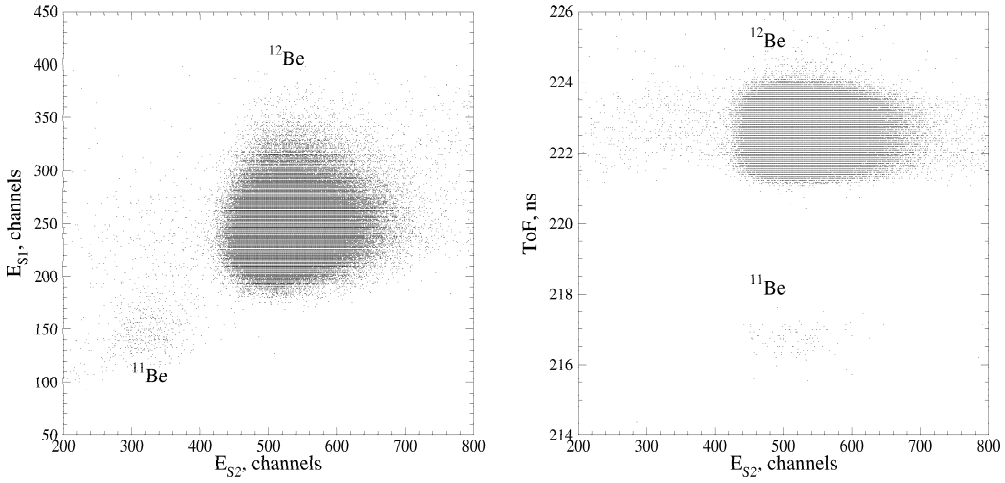

Figure 3.2: Isotope identification for the case of ^{12}Be beam.

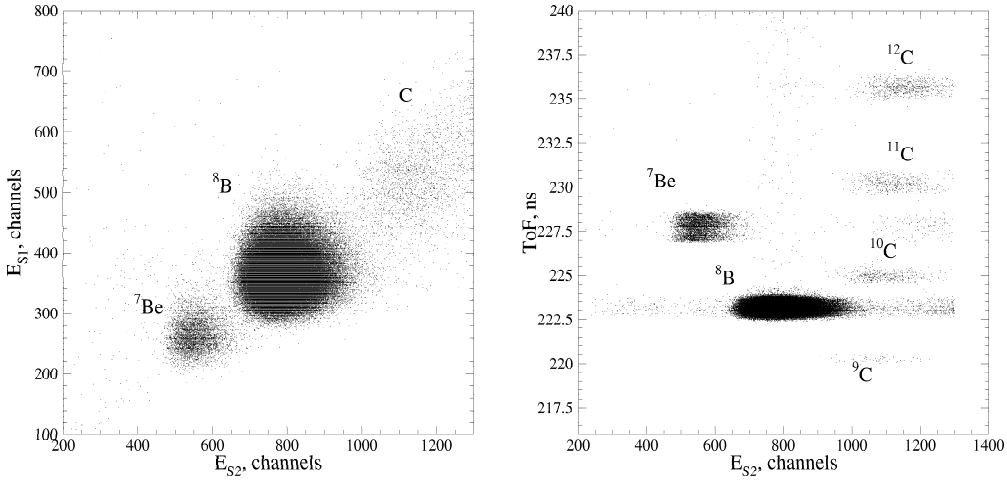

Figure 3.3: Isotope identification for the case of ^{8}B beam.

fitting the signals with a Gatti function $\Gamma_1(\lambda)$:

$$\frac{\rho(\lambda)}{q_a} = \Gamma_1(\lambda) = K_1 \frac{1 - tanh^2(K_2\lambda)}{1 + K_3 tanh^2(K_2\lambda)} \quad , \quad \lambda = \frac{x}{h} \quad , \tag{3.2}$$

which gives the best description of the response of the MWPC [64]. The fitting was done by using the induced charge method [63]. The variable λ of the Gatti function is given by the ratio of the distance x from the maximum of the signal and the distance between the anode and the cathode h. The Gatti function is equal to the charge density normalized to the total anode charge q_a. The parameters K_1, K_2 and K_3 depend on each other (see Eq. 3.3) and K_3 is determined from the chamber geometry:

$$\begin{aligned} K_1 &= \frac{K_2 K_3^{1/2}}{4arctan(K_3^{1/2})} \quad , \\ K_2 &= \frac{\pi}{2}(1 - \frac{1}{2}K_3^{1/2}) \quad . \end{aligned} \tag{3.3}$$

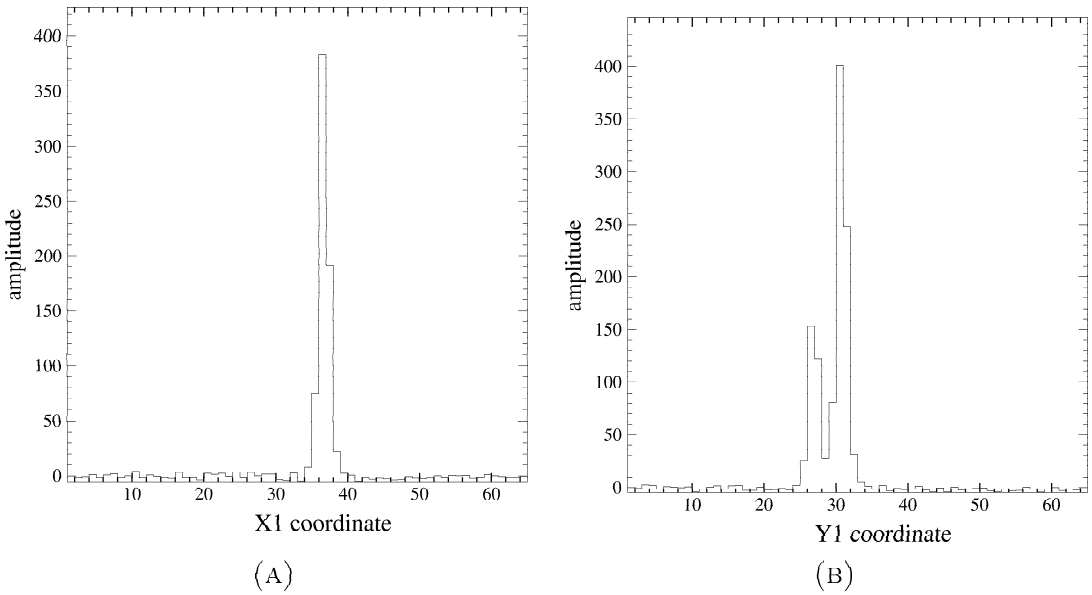

Figure 3.4: Proportional chamber signals. (A) Single signal. To determine the coordinate of the particle it is analyzed with the center of gravity method for three strips. (B) Double signal. The signal is fitted with a sum of Gatti functions in order to correct for the influence of the small second signal on the coordinate or the event is completely neglected from the further analysis (for details see text).

All events where three or more particles are observed as well as the ones where $S_1 < 3S_2$ were neglected. The parameters which were used for calculating the coordinates are listed in Table 3.1. The position resolution of the MWPCs was of the order of $\sigma = 150$ μm.

Chamber	N strips	W, cm	C_1	K_3
Small	64	0.25	1.27135	0.75
Big	86	0.30	1.18	0.846

Table 3.1: Parameters for calculating the particle coordinates from the proportional chamber signals using the Gatti function method.

In this way coordinates relative to the first strip in each chamber were determined. Then they were transformed to absolute coordinates with the zero position determined with an alignment procedure using the direct beam. For this the beam profiles of the direct beam in all planes of the MWPCs were used. Examples for the ^{8}B beam at MWPC1 and MWPC2 are shown in Fig. 3.5. The center of gravity of the beam was taken as the zero of the coordinate system. These beam profiles were also used to control the beam quality during the run. From the absolute coordinates the incoming and outgoing angles of the projectiles were calculated together with the corresponding scattering angle θ_s using simple geometry rules taking as a reference point the zero determined from the alignment. In Fig. 3.6 the trajectory of the projectile before and after the interaction is shown and the corresponding coordinates measured with the MWPCs are marked (x_1 to x_4 and y_1 to y_4). The

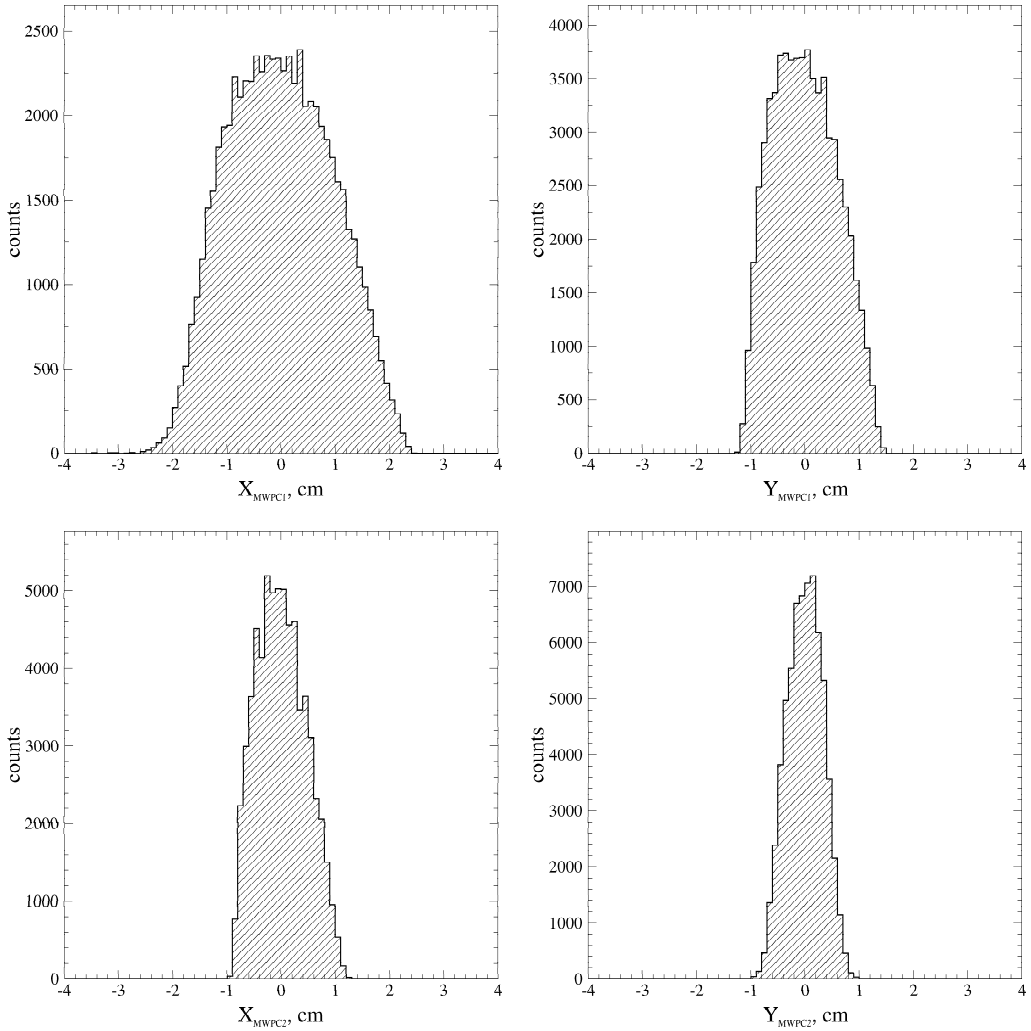

Figure 3.5: Beam profiles. The distribution of the coordinates of the beam particles in MWPC1 and MWPC2 are shown. The beam is focused at the center of IKAR.

absolute positions of the chambers, z_1 to z_4, with respect to the exit window of the beam line (defined as $z = 0$) were measured directly at the experimental setup. To calculate the scattering angle the following trigonometric equations are used:

$$\begin{aligned} tan\theta_x &= \frac{x_4 - x_3}{z_4 - z_3} - \frac{x_2 - x_1}{z_2 - z_1} \\ tan\theta_y &= \frac{y_4 - y_3}{z_4 - z_3} - \frac{y_2 - y_1}{z_2 - z_1} \\ \theta_s &= \sqrt{\theta_x^2 + \theta_y^2} \end{aligned} \tag{3.4}$$

The resolution for the scattering angle is determined by the position resolution of the proportional chambers and the angular spread due to the multiple Coulomb scattering of the projectiles. The resolution function for the case of ^{14}Be deduced from the unscattered beam is shown in Fig. 3.7. The contribution of the multiple Coulomb scattering to the uncertainty in this case is $\sigma_{ms} \approx 0.49$ mrad and the

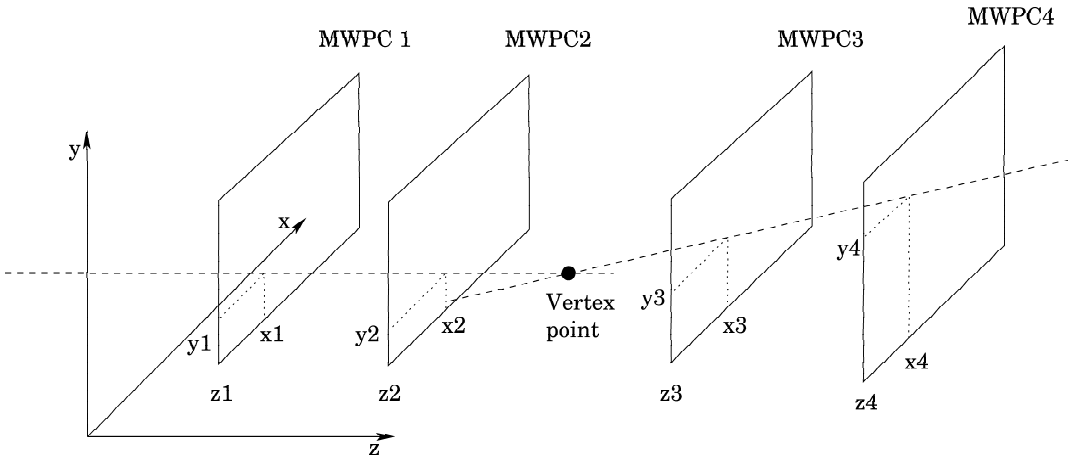

Figure 3.6: Geometry for projectile tracking and coordinate determination necessary for calculating the scattering angle θ_s.

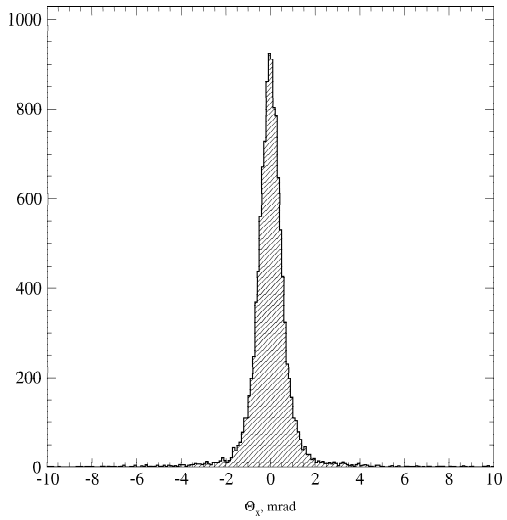

Figure 3.7: Angular resolution function of the tracking system of MWPCs, deduced from data on unscattered particles for the case of ^{14}Be beam. The determined resolution is $\sigma_{ms} \approx 0.61$ mrad including the multiple Coulomb scattering and the resolution of the MWPCs.

total uncertainty including the position resolution of the proportional chambers is $\sigma_{ms} \approx 0.61$ mrad.

With the information from the MWPCs the vertex point of the interaction can also be calculated. The detailed description of the procedure is given in Appendix B. This calculation has very big uncertainty and the values were not used for obtaining the cross section. They were only used during the analysis to check the consistency of the response of the different detectors in the setup (MWPC and IKAR).

The two-body kinematics for elastic scattering directly connects the scattering angle of the projectile with the proton recoil energy:

$$T_R = T_p(T_p + 2M)\frac{m + (T_p + M)sin^2\theta_s - cos\theta_s\sqrt{m^2 - M^2sin^2\theta_s}}{(T_p + m + M)^2 - T_p(T_p + 2M)cos^2\theta_s} \quad , \qquad (3.5)$$

where T_R is the recoil energy of the target nucleus, T_p is the energy of the projectile, M is the mass of the projectile, m is the mass of the target nucleus and θ_s is the scattering angle of the projectile (description of the scattering kinematics is given in Appendix C). For all variables the values in the laboratory system are used.

3.3 Detection of the recoil protons

From the IKAR detector three types of signals are obtained (Fig. 3.8(A)). The pulser signals were used to check the stability and linearity of the response of the electronics section. The energy calibration and the correction for the adhesion of electrons on the electro-negative impurities in the gas were obtained from α-particle signals. Signals from the recoil protons from different reactions were recorded as well. It should be noted that the energy and the amplitude of the signals in IKAR are not proportional as the shape of the signal depends on the angle between the ionization track and the chamber axis. For example, the α-particles, which always have the same energy, produce signals with different amplitude as they are emitted isotropically from the source in a 2π solid angle.

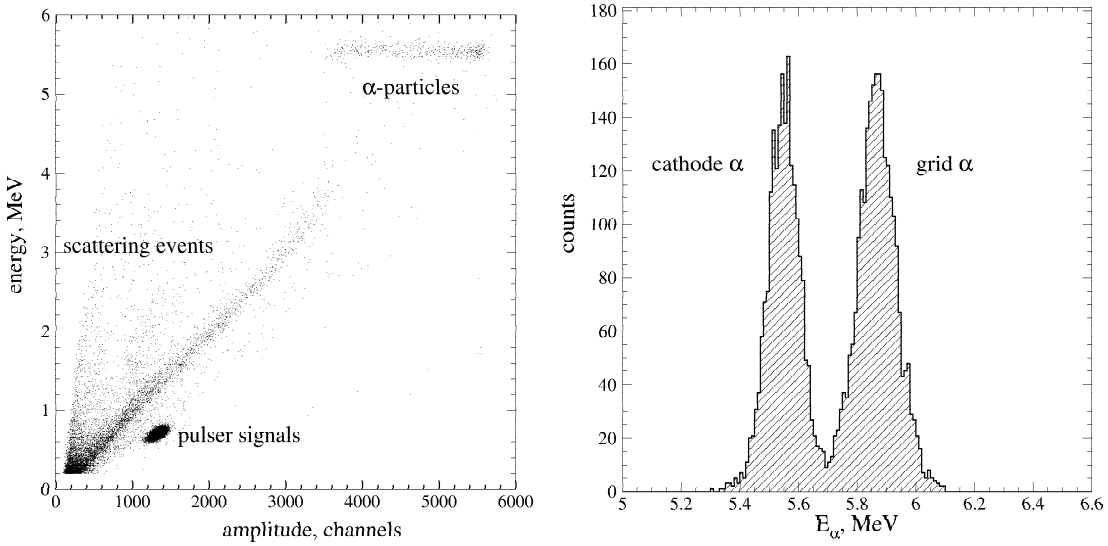

Figure 3.8: (A) 2D correlation between the energy measured in the IKAR detector and the amplitude of the signals. (B) Energy spectrum of α-particles measured in the fifth module. An average energy resolution $\sigma = 60 - 65$ keV for the whole detector was obtained.

The ^{241}Am source used for calibration in this experiment has an α-line with an energy $E_\alpha = 5486$ keV. The starts of the α-signals were located in random positions in the FADC spectra due to the fact that their appearance was not correlated with the trigger signal starting the data acquisition. The energy scale was calibrated using the cathode alphas. The dependence of the amount of ionization in the hydrogen gas on the energy of the particle has been thoroughly investigated [65]. It has been found that the charge on the anode is in good approximation a linear function of the

recoil energy almost in the whole energy range (except for very low energies) but this linear function does not go trough the zero of the coordinate system. The value of the energy where the charge becomes zero (the linear function crosses the energy axis) depends on the type of the ionization gas and for hydrogen it is -50 keV. This has to be taken into account in the calibration. When using α-particles to calibrate proton energies one should also take into account the different amount of ionization produced by α-particles and protons with the same energy. When both effects are taken into account the energy to which the signal from the α-particle has to be calibrated changes according to the equation:

$$E_{\alpha,1} = (E_\alpha - T_0)\frac{Q_R}{\gamma Q_\alpha} + T_0 \ , \tag{3.6}$$

where $T_0 = -50$ keV, Q_α and Q_R are the integrals of the signals from the α-particle and the proton, respectively, and $\gamma = 0.992$ is a coefficient to take into account the different ionization produced from the protons and the α-particles. Thus, we get a value $E_{\alpha,1} = 5530.6$ keV for the cathode α-particles to which the energy scale has to be calibrated. Due to the fact that the α-particles are emitted isotropically from the source and the distribution of the ionization along the track follows the Bragg curve distribution, the center of gravity of the charge from their ionization track effectively is not located on the cathode but at a distance $R/3$, where R is the range of the α-particle in the gas. For this reason a correction of the energy $E_{\alpha,1}$ has to be made to account for the adhesion in this distance ($R/3$) and the energy is increased to $E_{\alpha,2} = 5554$ keV which is the final value for calibration. Based on the information obtained from all modules of IKAR an average energy resolution of $\sigma = 60 - 65$ keV was achieved (Fig. 3.8(B)) for the IKAR detector.

The adhesion coefficient was determined by comparing the signals of the α-particles located at the grid and at the cathode. The energy of the alpha particles coming from the cathode source is a little bit lower than the one of the grid alphas due to the fact that their drift path is longer and more ionization electrons are lost. The difference between their paths until the signal appears on the anode were calculated taking again into account the isotropy of the emitted particles and a correction coefficient $\varrho = 0.00663$ cm^{-1} was determined. The energy of the protons was corrected according to:

$$E^{corr}_{IKAR} = E_{IKAR} e^{-\varrho d} \ , \tag{3.7}$$

where d is the distance between the center of gravity of the ionization track and the cathode in cm. In the present case the losses due to electron adhesion were less than 1 % per 10 cm drift path.

The FADC signals from events where no scattering took place (projectile passing through IKAR without any reaction happening) contain information about the geometry and time parameters of the chamber. The average of many such signals is shown in Fig. 3.9. The peak at the beginning of the signal is due to the different electron drift velocities in the cathode-grid and grid-anode volumes, and the slope of the plateau is due to the electronic response of the system. This signal can be

parameterized with the function:

$$I_A(t) = \begin{cases} 0, & t < t_{start} \\ \frac{Q_{tot}}{6t_{GA}}\left(1 - \frac{t-t_{start}}{t_{GA}} + \frac{5(t-t_{start})}{t_{GA}}\right), & t_{start} < t < t_{GA} \\ \frac{5Q_{tot}}{6t_{GA}}, & t_{GA} < t < t_{KG} \\ \frac{5Q_{tot}}{6t_{GA}}\left(1 - \frac{t-t_{start}}{t_{GA}} + \frac{t_{KG}}{t_{GA}}\right), & t_{KG} < t < t_{GA} + t_{KG} \\ 0, & t_{GA} + t_{KG} < t \end{cases}$$

which is obtained from the integrating of the different parts of the ionization track inside IKAR assuming a uniform distribution of the charge along the track. The factors 1/6 and 5/6 simply mean that 5/6 of the ionization is generated in the cathode-grid volume and 1/6 of it in the grid-anode volume. The indices KG and

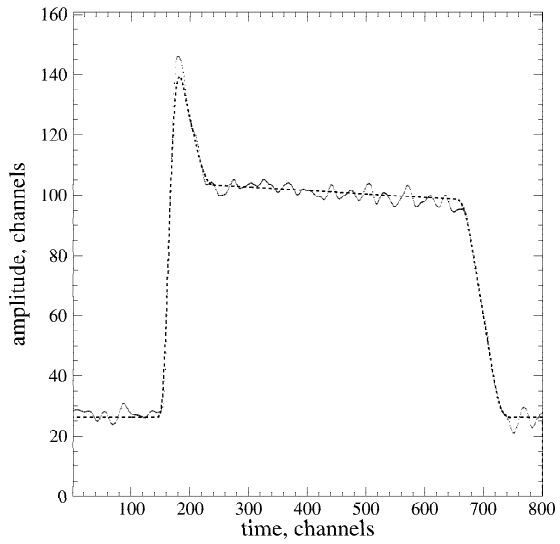

Figure 3.9: Average projectile signal from the sixth IKAR module (dotted line). The time parameters of the signal are determined with a fit to it (dashed line).

GA refer to cathode-grid and grid-anode variables, respectively. Q_{tot} is the total charge produced in IKAR and I_A is the current induced on the anode from the charge Q_{tot}. The anode signals from the projectiles were fitted with the above function and the distance between the grid and the cathode (given by the time difference between t_{GA} and t_{KG}) was determined for each of the six modules. Then the average distance was determined to be V_{KG}=500.35 channels. Using the fact that the geometric distance between the grid and the cathode is 10 cm (known with very high precision) this gives a conversion factor 0.1999 mm/channel, later used for determination of the target thickness.

A typical recoil proton signal is shown in Fig. 3.10. The projectile signal as determined above is already subtracted and the signal was smoothed. The parameters of the signal which were used further in the analysis in order to determine the energy of the recoil proton and vertex point of the interaction, and to separate the elastic from the inelastic events are marked. The begin and end of the signal are determined from the points where the tangents to the signal cross the baseline.

Then a trapezoid is build in such a way that its integral is equal to the integral of the original signal and the width of the signal is determined from the FWHM of the trapezoid. The amplitude of the signal is determined from the maximum of the original signal.

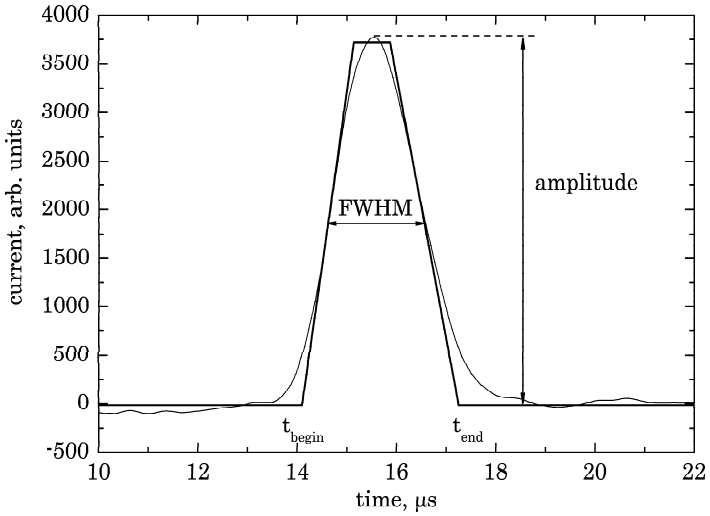

Figure 3.10: Proton signal taken with the FADC. It corresponds to a proton with recoil energy of 2.95 MeV. Smoothing and subtraction of the projectile signal was already applied to the raw signal. The parameters of the signal used for the further analysis, determined by approximating the signal with trapezoidal shape, are shown.

The vertex point of the interaction Z_v can be calculated from the beginning or end of the FADC signals (depending on the geometry of the modules). In Fig. 3.11 the two possible geometries are shown schematically. The beam always comes from the left. Depending on the drift direction, the vertex point appears to be at the beginning or at the end of the signal, respectively. For the calculation of the vertex

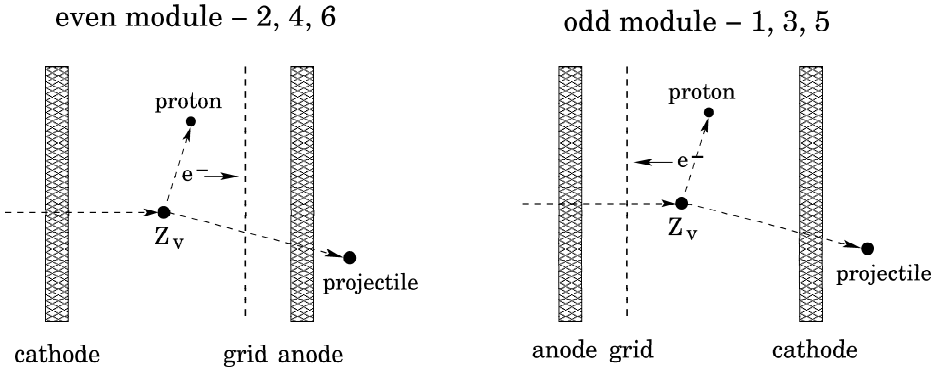

Figure 3.11: Geometry of the modules in IKAR with respect to the beam. A scattering event and the directions of the scattered projectile and the recoil proton are also indicated.

point Z_v the following relations are used:

$$\begin{aligned} Z_v &= Z_G - \frac{(t_{end} - t_{GA})d_{KG}}{V_{KG}}, \text{ even modules} \\ Z_v &= Z_G + \frac{t_{begin}d_{KG}}{V_{KG}}, \text{ odd modules} \end{aligned} \tag{3.8}$$

where Z_G is the position of the grid in mm, d_{KG} is the distance between the grid and the cathode in mm, t_{begin} and t_{end} are the begin and end of the signal in the FADC spectrum in channels, V_{KG} is the distance between the grid and the cathode in channels and t_{GA} is the grid-anode drift time of the electrons. The uncertainty of the vertex point determination varies with recoil energy and it starts from 0.5 mm for low T_R up to 3 mm for $T_R \approx 30$ MeV. This uncertainty increases with the increase of the recoil energy T_R because in that case the energy left in the IKAR detector decreases and becomes comparable with the noise level thus, making more inaccurate the determination of the signal parameters and the total recoil energy itself.

3.4 Effective target length

The effective target length V(T_R) is different from the length determined by the distance between the cathode and the grid and is important for the absolute normalization of the cross section $\mathrm{d}\sigma/\mathrm{d}t$. For its determination Monte Carlo simulations were made. There are two conditions which must be fulfilled in order to have a useful event. First, the scattering must take place far enough from the electrode's surface which assures that scattering on proton and not on the electrode's material happened. In addition, the effective length also depends on the recoil energy of the proton. The proton should lose all its energy or leave IKAR without entering the grid-anode volume. To comply with these conditions the region where useful events can be detected is limited and is a function of the proton energy (recoil angle). In Fig. 3.12 the energy dependence of the begin of the signal t_{begin} (which is analogous to the effective length) is shown for odd modules. Correspondingly, the length in the even modules is determined from the end t_{end} of the signal. For odd modules, at the side of the grid the limit is set to a constant value of 2 mm which assures that scattering on hydrogen and not on the electrode's material takes place. For even modules the same condition is applied on the side of the cathode. On the cathode side (for odd modules) the limit is expressed as an energy dependent function:

$$t_{begin} = \begin{cases} C_0 + C_1 T_R + C_2 T_R^2, & T_R < 5 \text{ MeV} \\ B_0 + B_1 T_R, & 5 \text{ MeV} < T_R < 30 \text{ MeV} \end{cases}$$

where the coefficients B_i and C_i are determined for each module and beam isotope individually. For even modules, similar function is used on the grid side. The functions and their parameters were determined with the help of Monte Carlo simulation. The uncertainty which the determination of the effective target length contributes to the absolute normalization of the cross section was estimated to be 0.5%.

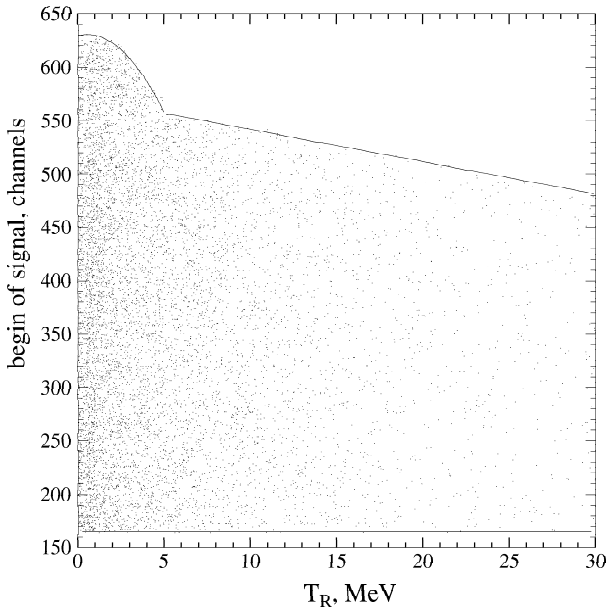

Figure 3.12: 2D plot of the begin of the signal in IKAR versus the recoil energy determined with the MWPCs for odd modules. Data points together with the energy dependence of the effective target length determined with a Monte Carlo simulation (solid lines) are potted. The effective target length is given between the solid lines. The target length in even modules is determined from analog correlations between the end of the signal and the recoil energy.

3.5 Selection of the elastic scattering events

This section explains the steps to be performed in order to obtain the absolute differential cross section for elastic scattering.

First, the projectile isotope impinging on the target is selected (Section 3.1). Then, the correlation between the coordinate measured at the scintillator wall after the ALADIN magnet and the scattering angle measured with the proportional chambers is used to discriminate the break-up reaction channels from the scattering events. This correlation is used instead of the absolute coordinates on the scintillator wall in order to compensate for the different entering angles in the magnetic field. This selection assures that the isotope survived after the reaction in the target. The energy loss in the scintillator wall is used to select the charge Z of the isotope and then the magnetic rigidity is used to separate the different masses. Examples for this selection for the cases of the isotopes presented in this work are shown in Fig. 3.13. In the case of ^{8}B there are no other boron isotopes present as this is the lightest one and only charge selection is sufficient.

As a next step, the elastic scattering events have to be separated from the inelastic events (in case the excited state is particle stable) and from other background events. For this purpose the parameters of the signals in IKAR and the recoil energy calculated from the MWPCs' signals are used. In Fig. 3.14 the two-dimensional correlation of the energy measured in IKAR versus the energy of the recoil proton determined from the scattering angle measured with the MWCPs and the effect of the event selection is shown. This selection is done using the amplitude, width, be-

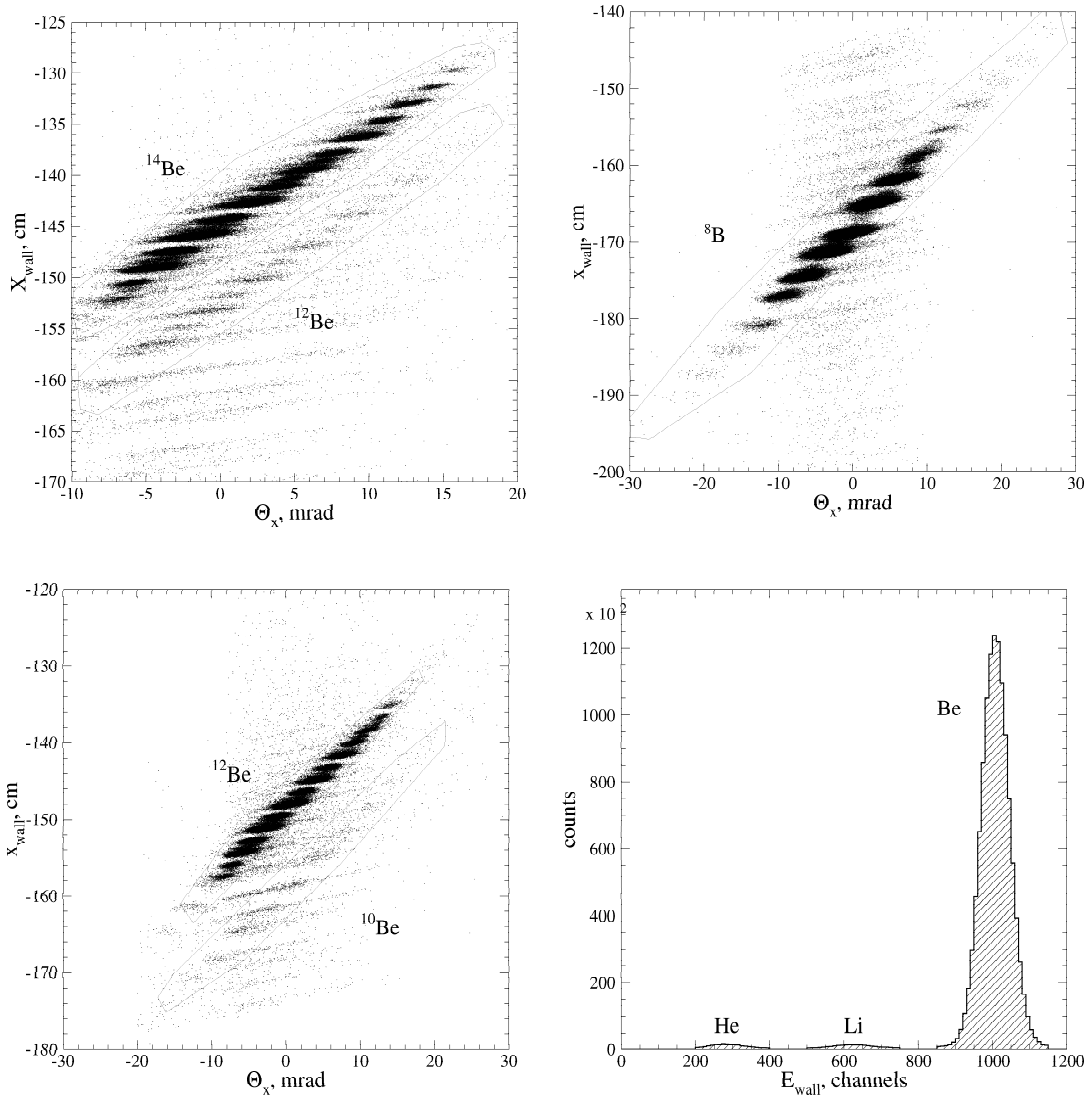

Figure 3.13: Correlation of the coordinate x behind the ALADIN magnet vs. the scattering angle θ_x (corresponding to the entering angle in the magnetic field) for the cases of ^{14}Be, ^{8}B and ^{12}Be beam. The magnetic field separates the isotopes with different magnetic rigidity thus, the break-up reaction channels are separated from the scattering events. In the case of ^{8}B there are no other isotopes as this is the lightest one. Additional determination of the isotope charge Z is done by the energy loss in the scintillator wall (plotted for the case of ^{12}Be beam).

gin and end of the signals in IKAR. A Monte Carlo simulation was made to establish the correlations between these variables which correspond to elastic events and then the proper cuts were applied to the data.

The recoil energy is measured in IKAR with much bigger accuracy than the one determined from the data from the proportional chambers. Thus, the energy T_R determined from the scattering angle has to be calibrated. For this purpose elastic scattering events with energy lower than 5 MeV were used (as in this case the protons are fully stopped in IKAR and their total energy is measured). In the correlation

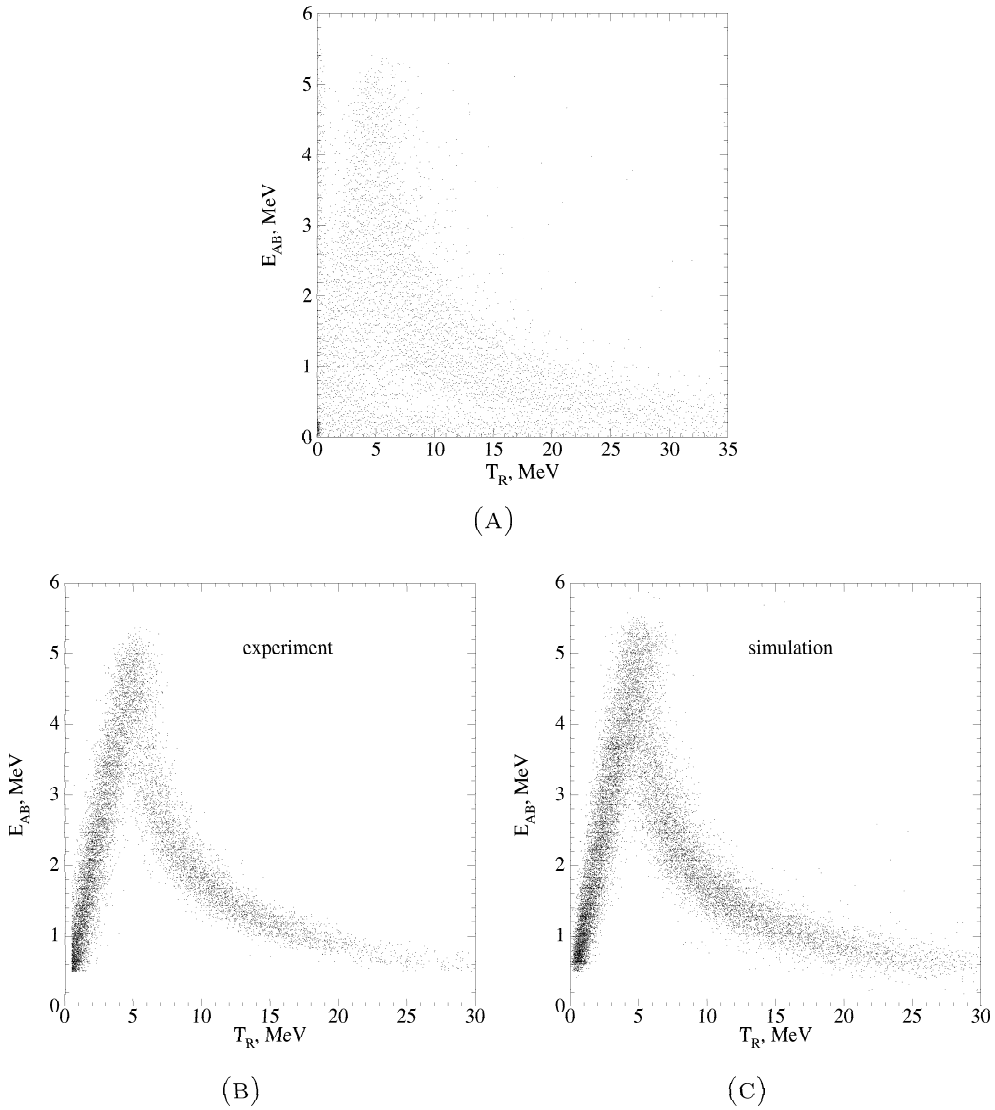

Figure 3.14: Correlation between the energy E_{AB} measured in IKAR versus the recoil energy T_R determined with the multi-wire proportional chambers for the case of a ^{12}Be beam. (A) before selection of elastic events; (B) after selection cuts are applied; (C) Monte Carlo simulation of the same correlation for elastic scattering events.

between E_{IKAR} and E_{MWPC} the scale of E_{IKAR} was divided in equidistant bins with a width of 0.250 MeV, and the MWPC energy corresponding to it was determined with a fit with a Gauss function. The correlation between the bin energy and the one determined with the Gaussian function (see Fig. 3.15) was then fitted with a linear function:

$$E_{IKAR} = aE_{MWPC} + b \ , \tag{3.9}$$

and T_R was calibrated according to this equation.

The last step before determining the number of elastic scattered events N_{el} corresponding to a certain recoil energy is the background subtraction of events which were not removed by the selection cuts. For very low momentum transfer the inelastic scattering cross section is several orders of magnitude smaller than the elastic

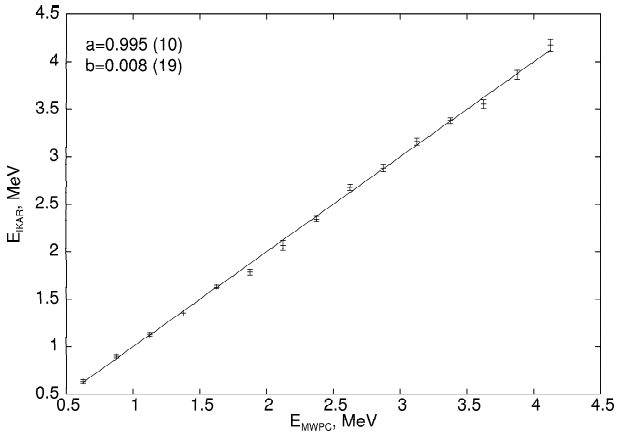

Figure 3.15: Plot of the recoil energy measured in IKAR versus the recoil energy determined with the MWPCs for the case of ^{12}Be isotope. For the calibration a linear function is used: $E_{IKAR} = aE_{MWPC} + b$.

one and can be neglected [8]. For the background subtraction, the correlation E_{AB} vs T_R (Fig. 3.14(B)) was divided in 0.5 MeV bins at the T_R scale for $T_R > 5$ MeV and the projection on E_{AB} was plotted (Fig. 3.16). From there, the corresponding number of elastic events and inelastic background were determined. For lower energies, similar procedure was used – 0.25 MeV bins were cut in the E_{AB} scale and the background was determined from the spectra projected on T_R.

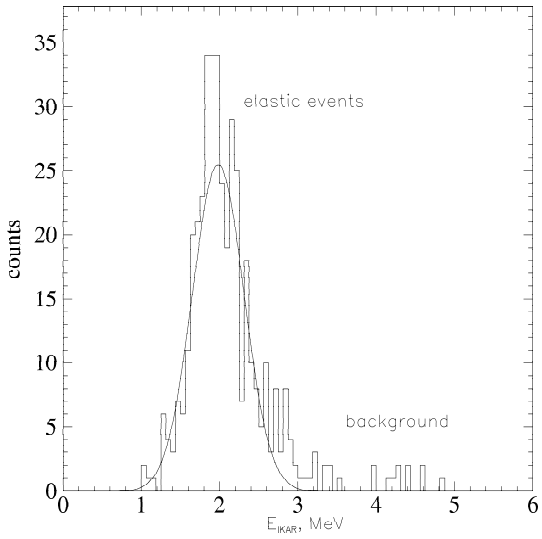

Figure 3.16: Example for background subtraction. For each interval $\Delta T_R = 0.5$ MeV of the recoil energy determined with the proportional chambers the energy distribution measured with IKAR is plotted ($E_{AB} \equiv E_{IKAR}$). The background events which do not correspond to elastic scattering are clearly separated.

The differential cross section is build from the experimental data from the number of elastic scattered events N_{el} in an interval Δt of the momentum transfer squared

through the formula:

$$\frac{\mathrm{d}\sigma}{\mathrm{d}t} = \frac{N_{el}}{\Delta t N_T M(1-\epsilon)} \ \mathrm{mb/(GeV/c)^2} \ , \tag{3.10}$$

N_T is the target thickness in part./cm^2, M is the number of incident particles (monitor) and ϵ is the inefficiency of the event selection. The Mandelstam variable t, which is equal to the square of the momentum transfer taken with a negative sign, can be calculated from the recoil energy of the protons using simple kinematics formula (Eq. 3.11), with m_p the proton mass in (GeV/c)^2 and T_R the recoil energy of the proton in MeV.

$$-t = q^2 = 2m_p T_R 10^{-3} \ \mathrm{(GeV/c)^2} \tag{3.11}$$

Analogously, the four-momentum transfer can be calculated from the momentum $\mathbf{p}$ and the scattering angle θ_s of the incident particle via:

$$|t| = \mathbf{p}^2 \theta_s^2 \ . \tag{3.12}$$

For normalizing the cross section one needs to know the thickness of the target N_T. It can be calculated from the target particle density n and the effective length of the target V(T_R):

$$N_T = n \frac{V(T_R)}{V_{KG}} d \ \mathrm{part/cm^{-2}} \ , \tag{3.13}$$

where V_{KG} is the distance between the cathode and the grid in channels (see Section 3.4) and d is the distance between the cathode and the grid in cm. The particle density of the target was determined through the Van der Waals equation:

$$n = \frac{N}{V} = \frac{p}{kT} \frac{1}{1 + B'(T)p^*} \ . \tag{3.14}$$

The temperature T in K and the pressure p in hPa were measured constantly during the experiment. The values for the first virial coefficient $B'(T)$ were calculated by G. Korolev [66] (at 300 K, $B'(T) = 0.000524$), $k = 1.38 \cdot 10^{-23}$ J/K is the Boltzmann constant. The value p^* is the pressure in technical atmospheres $p^* = p/980.655$. In this experiment the density of the hydrogen target was $n = 0.80839$ mg/cm^3.

The number of incident particles M is given by:

$$M = N_{coinc} - N_{EKR} - N_{LEKR} \ , \tag{3.15}$$

where N_{coinc} is the total number of beam particles which give first level trigger. The numbers N_{EKR} and N_{LEKR} denote particles killed by the control unit (CU) after a candidate for good event and after a killed event, respectively. The control unit provides pile-up protection in IKAR before and after the scattering events (see Section 2.3). The final number of monitors is obtained from the scaler value when the isotope of interest is selected in the off-line analysis and the contaminations from other isotopes are cleaned.

The correction ϵ depends on the amount of rejected elastic events from the selection cuts applied during the analysis and was determined with the Monte Carlo

simulations. The simulations take into account the finite size and angular spread of the incident beam, the multiple Coulomb scattering and the detector geometry. The simulated events were analyzed in the same manner as the experimental data and the efficiency of the event selection was evaluated. This efficiency depends on the recoil energy.

The total uncertainty in the absolute normalization of the differential cross section does not exceed 4 %. To this error contribute the uncertainty from the t-scale calibration which is ≈2%, the error in the determined number of incident particles of the order of ≈1 % and the error in the target length and density which are ≈2 % and ≈1 %, respectively. The total error was calculated as a quadratic sum of the individual errors.

The differential cross sections for p-^{12}Be, p-^{14}Be and p-^{8}B elastic scattering obtained as a result from the analysis are shown in Fig. 3.17. The energy given in the figure corresponds to the equivalent proton energy for the case of normal kinematics which is connected to the projectile energy in inverse kinematics through:

$$E_p = T_p \frac{m_p}{M} \ . \tag{3.16}$$

The obtained cross sections were analyzed within the Glauber multiple-scattering theory and the nuclear matter density distributions and *rms* matter radii were deduced (see Chapter 4 and 5).

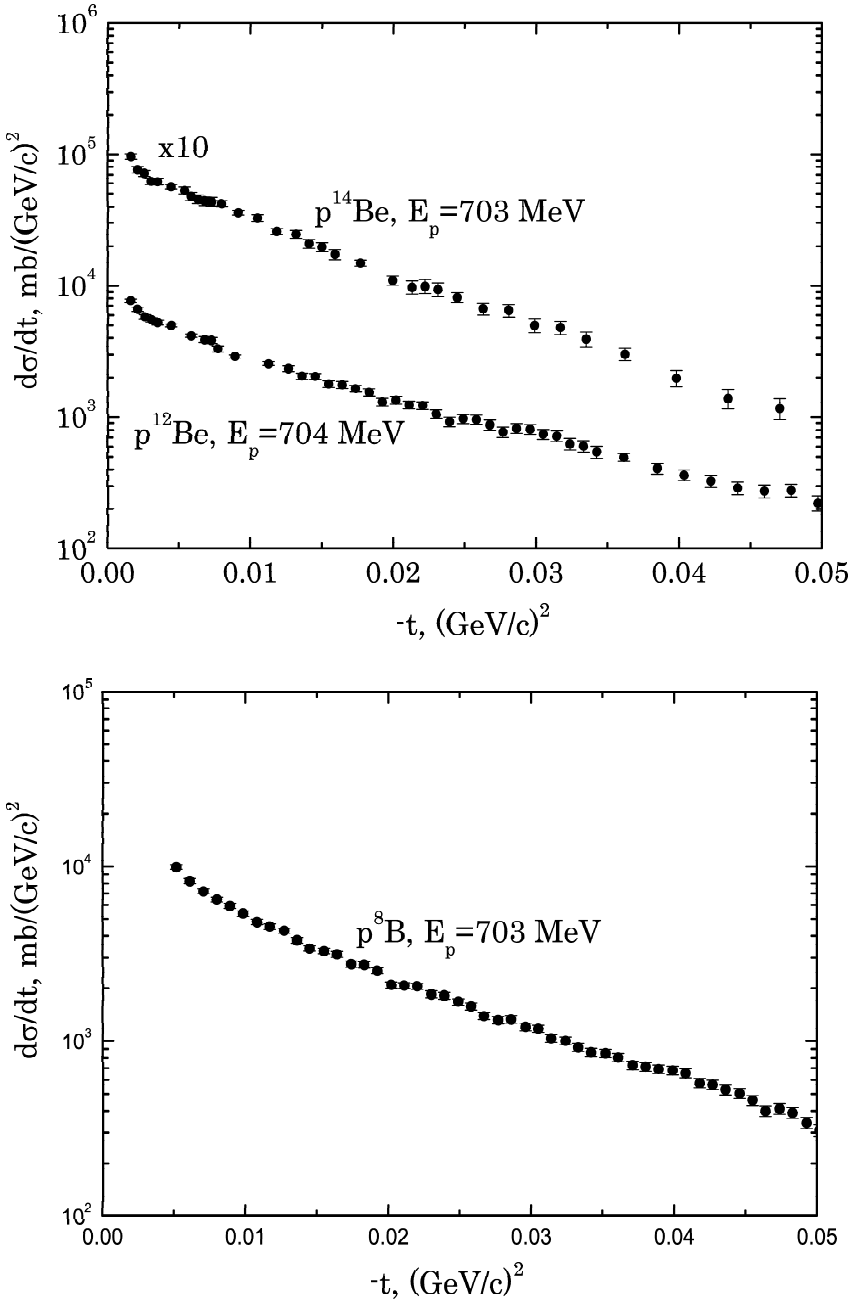

Figure 3.17: Experimental absolute differential cross sections for p-^{12}Be and p-^{14}Be elastic scattering versus the four-momentum transfer squared (top) and for p-^{8}B elastic scattering (bottom). The indicated energies correspond to the equivalent proton energies in direct kinematics. Statistical error-bars are plotted only.

CHAPTER 4

Theoretical background for the interpretation of the data

Elastic scattering on complex nuclei was used for a long time to study the nuclear structure of stable and exotic nuclei. The use of protons as projectile reduces the ambiguities in the theoretical description as no correlations between the nucleons in the projectile have to be taken into account. Such investigations were performed in a broad range of energies – from energies around the Coulomb barrier up to intermediate and high energies.

At low energies, in the region of the Coulomb barrier ($E \approx 5 - 30$ MeV/u), the scattering of particles can be described as potential scattering. The experimental data can be fit using complex potential functions which often bring ambiguities to the results. On the contrary, at higher energies around ≈ 1 GeV (much higher than the Fermi energy) the scattering processes are much better understood and can be described in terms of diffraction scattering in analogy to optics. Due to the high energy, the scattering between the nucleons in the projectile and the target can be approximated by the free nucleon-nucleon scattering amplitudes which is well studied in this energy region. Due to the short wavelength of the projectile smaller structures in the nuclear matter distribution can be studied which is not the case of potential scattering. Depending on the energy, an absorbing black disk approximation or multiple scattering are used. At energies of the order of 10 MeV and higher the wavelength of the relative particle motion is comparable to the nuclear size. Then the nucleus can be regarded as an absorbing black disc and the processes can be described in terms of diffraction scattering [67]. At higher energies (about 1 GeV or greater) the free path of the nucleon becomes smaller than the nuclear radius and it can be regarded as a transparent body. In this case multiple diffraction from the individual nucleons in the nucleus should be considered.

4.1 The Glauber multiple-scattering theory

The Glauber multiple-scattering theory is a diffractive theory which describes the scattering of nuclei at intermediate energies (500 MeV to 1 GeV) [7, 68, 69]. It connects the many-body density distribution of a nucleus with the differential cross section for nuclear scattering. The two main assumptions of the theory are the eikonal approximation and the adiabatic approximation. When a very energetic particle passes through the nucleus it is hardly deflected and it leaves the nucleus before any changes in the arrangement of the nucleons can take place. Thus, the trajectory of the projectile inside the nucleus can be approximated with a straight line (eikonal approximation) [7]. Due to the fact that the particle energy is so much higher than the energy of the internal motion of the nucleons they can be regarded as stationary during the collision (adiabatic approximation). The incident particle tends to lose only a small fraction of its energy and momentum in each individual collision and with the above approximations the total phase shift can be written as the sum of the individual phase shifts for scattering on single nucleons. For the elementary scattering amplitudes of the free proton-proton (pp) and proton-neutron (pn) scattering the experimental values are used.

The differential cross section for elastic scattering in a single scattering approximation is given by:

$$\frac{\mathrm{d}\sigma}{\mathrm{d}\Omega} = A^2|f(\mathbf{q})|^2 S^2(\mathbf{q}) \quad , \tag{4.1}$$

$$S(\mathbf{q}) = \int e^{i\mathbf{q}\cdot\mathbf{r}}\rho(\mathbf{r})\mathrm{d}^3 r \quad , \tag{4.2}$$

where $f(\mathbf{q})$ is the amplitude for scattering by a single nucleon with a momentum transfer $\mathbf{q}$[1] ($\mathbf{q} = \mathbf{p_i} - \mathbf{p_f}$, $\mathbf{p_i}$ and $\mathbf{p_f}$ being the initial and final momentum of the proton, respectively), A is the nuclear mass number and $S(\mathbf{q})$ is the nuclear form factor. This approximation gives only qualitative description as also screening effects between the nucleons and multiple collisions influence the measured cross section. To treat these effects the diffraction theory of multiple scattering is used.

When the momentum of the incident particle $\mathbf{p_i}$ is sufficiently high so that its wavelength is smaller than the interaction range between the proton and the nucleus, the individual scattering amplitudes contribute coherently to the scattering. The partial wave expansion of the scattering amplitude then is given by the two dimensional Fourier integral of the profile function $\gamma(\mathbf{b})$:

$$f(\mathbf{q}) = \frac{ik}{2\pi}\int e^{i\mathbf{q}\cdot\mathbf{b}}\gamma(\mathbf{b})\mathrm{d}^2 b \quad , \tag{4.3}$$

where $\mathbf{b}$ is the impact parameter and integration is made on a plane perpendicular to the direction of the momentum of the incident proton. This expression is accurate as long as the momentum transfer $\mathbf{q}$ is small compared to the incident momentum $\mathbf{p_i}$ of the particle. Correspondingly, the nucleon profile function can be calculated from the inverse Fourier transform:

$$\gamma(\mathbf{b}) = \frac{1}{2\pi ik}\int e^{-i\mathbf{q}\cdot\mathbf{b}} f(\mathbf{q})\mathrm{d}^2 q \quad . \tag{4.4}$$

[1] For simplicity a system with $c = \hbar = 1$ is used.

The profile function depends on the impact parameter $\mathbf{b}$ and the projections of the nucleons' positions $\mathbf{r_1}, \ldots, \mathbf{r_A}$ on the plane perpendicular to the direction of the projectile momentum, which are denoted as $\mathbf{s_1}, \ldots, \mathbf{s_A}$ (Fig. 4.1(A)). The diffraction

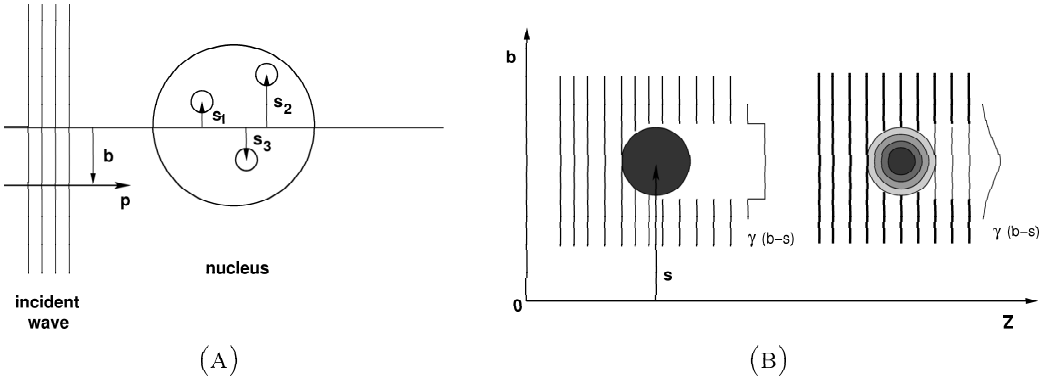

(A) (B)

Figure 4.1: (A) Scheme of proton-nucleus interaction (the proton is shown as a plane wave). The impact parameter b and the transverse components s_j of the nucleons' coordinates are defined. (B) Scattering on a nucleon, described as a black disk with uniform density (left) and with a density distribution increasing towards the center (right). The corresponding profile functions, describing how the amplitude of the initial wave is attenuated are also shown.

amplitude for a scattering process in which the nucleus is transformed from an initial state $|i\rangle$ to a final state $|f\rangle$ with a momentum transfer $\mathbf{q}$ is:

$$F_{fi}(\mathbf{q}) = \frac{ik}{2\pi} \int e^{i\mathbf{q}\cdot\mathbf{b}} \langle f|\Gamma(\mathbf{b}, \mathbf{s_1}, \ldots, \mathbf{s_A})|i\rangle \mathrm{d}^2 b \quad , \tag{4.5}$$

where $\Gamma(\mathbf{b}, \mathbf{s_1}, \ldots, \mathbf{s_A})$ is the nuclear profile function. We can evaluate the profile function using a simple optical analogy (Fig. 4.1(B)). The nucleus can be regarded as a collection of refractive/absorbing objects, each with a refractive index close to unity. In this case the incident wave is not distorted much when passing through the nucleus and the phase shifts χ_j produced by the individual nucleons combine additively. The total phase shift function is:

$$\chi(\mathbf{b}, \mathbf{s_1}, \ldots, \mathbf{s_A}) = \sum_j \chi_j(\mathbf{b} - \mathbf{s_j}) \quad , \tag{4.6}$$

and the nuclear profile function becomes:

$$\begin{aligned} \Gamma(\mathbf{b}, \mathbf{s_1}, \ldots, \mathbf{s_A}) &= 1 - e^{i\chi(\mathbf{b}, \mathbf{s_1}, \ldots, \mathbf{s_A})} \\ &= 1 - \prod_j e^{i\chi_j(\mathbf{b}-\mathbf{s_j})} \\ &= 1 - \prod_j^A [1 - \gamma_j(\mathbf{b} - \mathbf{s_j})] \end{aligned} \tag{4.7}$$

This function describes scattering from nucleons with fixed positions. When the product in Eq. (4.7) is expanded we get the combination law for the profile functions:

$$\Gamma(\mathbf{b}, \mathbf{s_1}, \ldots, \mathbf{s_A}) = \sum_j \gamma_j(\mathbf{b} - \mathbf{s_j}) - \sum_{j<m} \gamma_j(\mathbf{b} - \mathbf{s_j})\gamma_m(\mathbf{b} - \mathbf{s_m}) + \ldots \quad . \tag{4.8}$$

In this way a multiple scattering series is generated. If position correlations between the nucleons in the nucleus are neglected and we write the many-body density function of the nuclear ground state in factorized form from the one-body densities ($\rho(\mathbf{r_1},\ldots,\mathbf{r_A}) = \prod_{j=1}^{A}\rho(\mathbf{r_j})$), the profile function averaged over all the nucleons becomes:

$$\Gamma(\mathbf{b}) = 1 - e^{i\chi(\mathbf{b})} = 1 - \left(1 - \frac{1}{2\pi ik}\int e^{-i\mathbf{q}\cdot\mathbf{b}} f(\mathbf{q})S(\mathbf{q})\mathrm{d}^2q\right)^A \tag{4.9}$$

with $\chi(\mathbf{b})$ being the nuclear phase shift function also averaged over all the nucleons and $S(\mathbf{q})$ - the form factor of the one-body density.

With the sum (4.8) we are able to construct the overall scattering amplitude (4.5) from the knowledge of the profile functions γ_j of the individual nucleons calculated from the inverse Fourier transform of the free scattering amplitudes $f_{pN}^j(\mathbf{q})$ which are known from measurements.

Free pp and pn scattering amplitudes

The free pp and pn scattering amplitudes consist of a scalar part (central term), coming from the strong interaction, and a vector contribution from the spin-orbit and spin-spin interaction. At energies close to 1 GeV the vector part is negligible compared to the scalar one [7]. The scalar amplitudes are approximated with the following distribution:

$$f_{pN}^c(\mathbf{q}) = \frac{\mathbf{k}\sigma_{pN}}{4\pi}(\epsilon_{pN} + i)e^{-\frac{q^2\beta_{pN}^2}{2}} \quad . \tag{4.10}$$

The parameter σ_{pN} is the total pN scattering cross section, β_{pN} is the slope of the differential cross section, ϵ_{pN} is the ratio between the imaginary and the real part of the scattering amplitude (N replaces the corresponding nucleon proton or neutron) and $\mathbf{k}$ is the wave vector of the projectile:

$$|\mathbf{k}| = \frac{T_1^2 + 2MT_1}{\sqrt{\frac{2T_1}{m} + (1 + \frac{M}{m})^2}} \ , \tag{4.11}$$

where T_1 is the projectile kinetic energy per nucleon and M and m are the projectile and target masses, respectively. This parameterization corresponds to scattering by an optical potential and for $\mathbf{q} = 0$ we get the Optical theorem:

$$Im(f(0)) = \frac{\mathbf{k}\sigma_{pN}}{4\pi} \tag{4.12}$$

For calculating the pp and pn scattering amplitudes the results from the Phase Shift Analysis [70] of data from experiments at different energies have been extrapolated [9]. In Fig. 4.2 the available data on the elementary cross sections σ_{pN} for free pp and pn scattering and the ratios ϵ_{pN} are displayed as a function of the proton energy E_p [9]. The slope parameters in the present analysis were chosen to be $\beta_{pp} = \beta_{pn} = 0.17$ fm^2. The values of the parameters of the pN scattering amplitudes used for the present analysis are listed in Table 4.1.

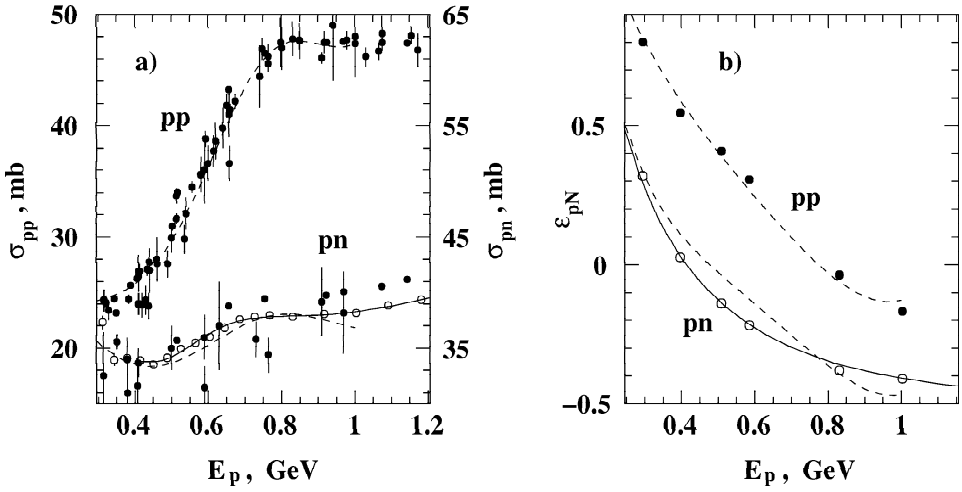

Figure 4.2: (a) Energy dependence of the total cross section σ_{pN} for free pp and pn scattering. (b) Energy dependence of the ratios ϵ_{pN}. Details about the fits to the data can be found in Ref. [9].

Nucleus	T_p, MeV	σ_{pp}, mb	ϵ_{pp}	σ_{pn}, mb	ϵ_{pn}	$\beta_{pp} = \beta_{pn}$, fm^2
^{12}Be	703.5	43.63	0.092	37.58	-0.298	0.17
^{14}Be	702.9	43.59	0.093	37.58	-0.298	0.17
^{8}B	703.4	43.62	0.092	37.58	-0.298	0.17

Table 4.1: Parameters of the free pp and pn scattering amplitudes used in the present analysis. T_p represents the equivalent proton laboratory energy in direct kinematics.

Contribution of the Coulomb interaction

Besides the strong interaction, the Coulomb interaction between charged particles also has a noticeable effect on the scattering cross section at very small momentum transfer where the interference between the Coulomb and the strong amplitudes is the strongest. In order to describe properly the cross section at small momentum transfer the Coulomb interaction has to be taken into account. One can write the pp phase shift as the sum of purely strong and Coulomb phase shifts [7]:

$$\chi_p(\mathbf{b}) = \chi_p^N(\mathbf{b}) + \chi_p^C(\mathbf{b}) \quad . \tag{4.13}$$

The Coulomb phase shift $\chi_p^C(\mathbf{b})$ can be calculated with:

$$\chi_p^C(\mathbf{b}) = -\frac{1}{\hbar v} \int_{-\infty}^{\infty} U(\mathbf{b}, z) \mathrm{d}z \ , \tag{4.14}$$

where $U(\mathbf{b}, z)$ is the Coulomb pp potential. For calculating the p-nucleus scattering amplitude a more simple approach giving practically the same result can be used. In this case the interaction of the projectile proton with the averaged Coulomb field of the nucleus is used. In the present analysis the averaged Coulomb field method was used and details about the calculation can be found in [7, 9].

Center of mass correlations

In the above considerations no correlations between the nucleons in the target nucleus were taken into account. The center of mass (CM) motion of the nucleus has an appreciable contribution to the cross section in the region of high momentum transfer (large scattering angles), with the effect decreasing with increasing mass number A [7]. The correlations between the nucleons in the nucleus can be expressed in mathematical terms with the condition $\sum_{j=1}^{A} \mathbf{r_j} = 0$ (with $\mathbf{r_j}$ being the CM coordinates of the nucleons). The correction factor is calculated according to Eq. (4.15):

$$H_{CM}(\mathbf{q}) = e^{\frac{q^2\langle r^2\rangle}{6(A-1)}} \quad . \tag{4.15}$$

This equation gives an exact correction for a Gaussian density. For a non-Gaussian density the CM motion is taken into account to a good approximation up to the second diffraction minimum [7]. With this factor the corrected scattering amplitude is:

$$F(\mathbf{q}) = H_{CM}(\mathbf{q})F'(\mathbf{q}) \tag{4.16}$$

The CM correlations are especially important for light nuclei [9].

Clusterization correlations

A dynamic correlation which may exist in the nuclear matter is due to possible α-clusterization [7]. The α-cluster structure is supposed to be similar to the one of the free α-particle. Calculations show that clusterization without repulsion between the the α-clusters brings a considerable reduction of the cross section near the maxima, while when repulsive correlations are included the effects from the clusterization become less. Due to the significant compensation of the effects from proper α-clusterization and α-cluster repulsion it is difficult to study them separately. The differential cross section calculated when these correlations are included differs very little from the one where only center of mass correction is included. The influence of the correlations between the halo neutrons on the cross section were investigated for the ^{6,8}He isotopes and it was shown that they have only small effect on the deduced matter radii [9]. Thus, in the present analysis these correlations were not taken into account in the cross section calculations and fits.

Other effects contributing to the cross section

For nuclei with a non-zero spin the cross section depends on the spin-orbit interaction. The spin-orbit amplitude increases the cross section in the maximum while at the minimum it can be both increased or decreased [7]. In the case of light nuclei, the cross section for intermediate energy proton elastic scattering at low momentum transfer ($t < 0.05$ (GeV/c)^2) is not affected by this effect and does not exhibit any spin dependence [7].

The nuclear deformation also affects the cross section by filling the diffraction minima [7] but is not crucial for the low momentum transfer region.

As these two effects are negligible for the region of small momentum transfer, they were not taken into account in the present analysis.

4.2 Density parameterizations

4.2.1 *Phenomenological parameterizations*

Single Gaussian (SG) parameterization

In the single Gaussian parameterization the point density of each nucleon in the nucleus is approximated with a Gaussian function:

$$\rho(r) = \left(\frac{3}{2\pi R_m^2}\right)^{3/2} e^{\left(-\frac{3r^2}{2R_m^2}\right)} , \tag{4.17}$$

where the parameter R_m is the *rms* matter radius of the nucleus. This approximation is good in the cases of light nuclei with a compact structure.

Symmetrized Fermi (SF) parameterization

The standard Fermi density distribution:

$$\rho_F(r) = \rho_0 \left(1 + e^{\left(\frac{r-R}{a}\right)}\right)^{-1} \tag{4.18}$$

describes well the radial shape of nuclear matter in medium and heavy nuclei. In order to make it suitable for the description of light nuclei it has been modified and in this case a symmetrized Fermi density is used [71]:

$$\begin{aligned} \rho_m(r) &= \rho_0 \left[\left(1 + e^{\left(\frac{r-R}{a}\right)}\right)^{-1} + \left(1 + e^{\left(\frac{-r-R}{a}\right)}\right)^{-1} - 1\right] \\ &= \rho_0 \frac{sinh(R/a)}{cosh(R/a) + cosh(r/a)} \end{aligned} \tag{4.19}$$

with a normalization:

$$\rho_0 = \frac{3}{4\pi R^3} \frac{1}{1 + (\pi a/R)^2} , \tag{4.20}$$

where R is the "half-density radius" ($\rho(R) = \rho(0)/2$) and a is the width of the nuclear density surface layer. The *rms* nuclear matter radius R_{rms} is connected to R and a by the relation:

$$R_m = \left(\frac{3}{5}\right)^{1/2} R[1 + \frac{7}{3}\left(\frac{\pi a}{R}\right)^2]^{1/2} . \tag{4.21}$$

This function has exponential decrease at large r and flattens out at the center of the nucleus which is the characteristic behaviour of the nuclear density distribution.

Gaussian - Gaussian (GG) parameterization

In the case of halo nuclei it is reasonable to parameterize the core and halo densities separately. In the GG parameterization both core and halo distributions are described by Gaussian functions:

$$\begin{aligned} \rho_c(r) &= \left(\frac{3}{2\pi R_c^2}\right)^{3/2} e^{\left(-\frac{3r^2}{2R_c^2}\right)} , \\ \rho_h(r) &= \left(\frac{3}{2\pi R_h^2}\right)^{3/2} e^{\left(-\frac{3r^2}{2R_h^2}\right)} . \end{aligned} \tag{4.22}$$

Here R_c and R_h are the *rms* radii of the core and halo nucleon distributions. The total matter distribution ρ_m, normalized to one nucleon, and the matter radius R_m are given by:

$$\begin{aligned} \rho_m(r) &= [N_c\rho_c(r) + (A - N_c)\rho_h(r)]/A \quad , \\ R_m &= \Big(\frac{N_c R_c^2 + (A - N_c)R_h^2}{A}\Big)^{1/2} \quad , \end{aligned} \tag{4.23}$$

where N_c is the number of nucleons in the core and A is the atomic mass number.

Gaussian - Harmonic oscillator (GO) parameterization

In the GO parameterization the core is again described by the Gaussian function (4.22) while for the halo a harmonic oscillator density distribution for an oscillator function with angular momentum $l = 1$ is used:

$$\rho_h(r) = \frac{5}{3}\Big(\frac{5}{2\pi R_h^2}\Big)^{3/2}\Big(\frac{r}{R_h}\Big)^2 e^{\left(-\frac{5r^2}{2R_h^2}\right)} \tag{4.24}$$

The matter distribution and the matter radius are again calculated by Eq. (4.23).

Gaussian - Halo (GH) parameterization

The GH density distribution [9] is defined by the form factor:

$$S(t) = (1 + \alpha z^2)e^{-z} \quad , z = t\frac{R_m^2}{6} \quad , \tag{4.25}$$

with a parameter α in the range [0,0.4]. For $\alpha = 0$ the GH density distribution coincides with a Gaussian function, while for $\alpha = 0.4$ it describes a distribution with a pronounced halo component. The parameter R_m which is equal to the nuclear matter radius is related to the slope in the t-dependence of the differential cross section and α is related to its curvature. The GH density distribution is:

$$\begin{aligned} \rho_m(r) &= \Big(\frac{3}{2\pi R_m^2}\Big)^{3/2}[1 + \alpha\varphi(r)]e^{\left(-\frac{3r^2}{2R_m^2}\right)} \quad , \text{with} \\ \varphi(r) &= \frac{3}{4}[5 - 10\Big(\frac{r}{R_m}\Big)^2 + 3\Big(\frac{r}{R_m}\Big)^4] \ . \end{aligned} \tag{4.26}$$

Gaussian - Exponential (GE) parameterization

In the case of Gaussian plus exponential density parameterization, the core of the nucleus is parameterized with the usual Gaussian function with a parameter R_c, describing the core radius, whereas the distribution of the valence nucleon/s is described with an exponential function of the form:

$$\rho_h(r) = \frac{r^2}{R_h^5}e^{-\sqrt{30}\frac{r}{R_h}} \ , \tag{4.27}$$

with a parameter R_h corresponding to the radius of the valence nucleon/s (halo radius).

4.2.2 *Sum of Gaussian parameterization*

The method for analyzing the differential cross section using a Sum of Gaussian (SOG) density parameterization was first used very successfully in electron scattering experiments for determining the charge distributions of nuclei [72, 73]. In contrast to the previously mentioned phenomenological densities this method is in principle model independent as no constraint on the shape of the nucleus are made a priori, rather the density distribution is expanded on a basis of Gaussian functions. In such a way any shape can be described.

In this approach the density is parameterized with the following sum:

$$\rho(r) = \frac{Ze}{2\pi^{3/2}\gamma^3} \sum_{i=1}^{N} \frac{A_i}{1 + 2R_i^2/\gamma^2} (e^{-\frac{(r-R_i)^2}{\gamma^2}} + e^{-\frac{(r+R_i)^2}{\gamma^2}}) \quad , \tag{4.28}$$

where A_i is the relative weight of the i^{th} Gaussian, R_i is the position of the i^{th} Gaussian and γ is the width of all Gaussians. The normalization condition for the density is:

$$\int_0^\infty \rho(r) 4\pi r^2 dr = A \quad . \tag{4.29}$$

The parameter γ is defined by the width (FWHM) $\Gamma = 2\gamma\sqrt{\ln 2}$ which is the minimal width of the admissible structures in the density distribution. The choice of a Gaussian for the basis has been made because the theoretical radial wave functions show peaks which roughly have Gaussian shape, and because this function falls rapidly with increasing $|R_i - r|$ hence, small interferences between the densities at radii $|r_1 - r_2| > 1/2\Gamma$ are obtained [72]. Due to the flexibility of the shape (4.28) local variations of $\rho(r)$ are possible, however, they are independent of the behaviour of $\rho(r)$ at other radii far away.

This analysis gives accurate results when there is information about the cross section in the whole range of momentum transfer. In real experiments that is never the case and only limited data are available thus, in the analysis some constraints on the parameters must be placed. In order to reduce the model dependence to minimum several hundreds of different sets of R_i are chosen by random numbers in the analysis procedure. The widths of all Gaussians are fixed to the same value and equal to γ. For every set of R_i the amplitudes A_i are fitted to the data. A condition $A_i > 0$ is set so that no structures narrower than γ are created by the sum in Eq. (4.28). Then all distributions with a good χ^2 [2] are accepted and a superposition of them defines a band of possible values for $\rho(r)$. The average density together with a 1σ error band is taken as significant in the analysis. More accurate density distributions with smaller uncertainties can be obtained when data with bigger range of momentum transfer are analyzed.

[2] all densities with $\chi^2 < \chi^2_{min} + 1$ construct the average density with a one σ error-band

4.3 Fitting procedure

As it was discussed before, the differential cross section in the frame of the Glauber multiple-scattering theory is given by:

$$\frac{\mathrm{d}\sigma}{\mathrm{d}\Omega} = |F_{fi}(\mathbf{q})|^2 \quad , \text{ with}$$
$$F_{fi}(\mathbf{q}) = \frac{ik}{2\pi}\int \mathrm{d}^2b e^{i\mathbf{q}\cdot\mathbf{b}}\Gamma(\mathbf{b},\mathbf{s_1},\ldots,\mathbf{s_A})\rho_A^{fi}(\mathbf{s_1},\ldots,\mathbf{s_A})\prod_{j=1}^{A}\mathrm{d}^2s_j \tag{4.30}$$

The measured differential cross sections are obtained as a function of the four-momentum transfer squared q^2. For determining the cross section as a function of the solid angle Ω the following conversion equation was used (see Appendix C):

$$\frac{d\sigma}{dt} = \frac{\pi}{\mathbf{k}^2}\frac{d\sigma}{d\Omega} \ . \tag{4.31}$$

The aim of the fitting procedure is to find, for a given density parameterization, those parameter values for which the differential cross section calculated according to Eq. (4.30) describes the experimental data the best way. For the fit the χ^2 method was applied with the following χ^2 function:

$$\chi^2 = \sum_{j=1}^{N}\left(\frac{A_n\sigma_{exp}(t_j) - \sigma_{th}(t_j)}{\Delta\sigma_{exp}(t_j)}\right)^2 + \left(\frac{A_n - 1}{\Delta A_{exp}}\right)^2 \ . \tag{4.32}$$

Here N is the number of cross section data points, $\sigma_{exp}(t_j)$ and $\Delta\sigma_{exp}(t_j)$ are the experimental differential cross section for a given momentum transfer t_j and its error, $\sigma_{th}(t_j)$ is the corresponding calculated cross section value for the same momentum transfer t_j and A_n is a normalization factor, which was used as an additional free parameter, with ΔA_n being the systematic uncertainty in the absolute normalization of the experimental data. In the ideal case a normalization $A_n = 1$ should be obtained. The reduced chi-square χ_r^2 is then:

$$\chi_r^2 = \frac{\chi^2}{N - N_{free}} \ , \tag{4.33}$$

where N_{free} is the number of free parameters used in the density parameterization. The χ_r^2 estimates the quality of the fit, the optimal value being close to 1.

In the case of two free parameters a and b the absolute uncertainty of the obtained matter distribution $\rho_m(r)$ is calculated using the error propagation formula:

$$\Delta\rho_m(r) = \left((\frac{\partial\rho_m(r)}{\partial a}\cdot\sigma_a)^2 + (\frac{\partial\rho_m(r)}{\partial b}\cdot\sigma_b)^2 + (2\frac{\partial\rho_m(r)}{\partial a}\cdot\frac{\partial\rho_m(r)}{\partial b}\sigma_a\cdot\sigma_b\cdot\kappa_{a,b})\right)^{1/2} \ , \tag{4.34}$$

where σ_a and σ_b are the corresponding *rms* errors of the fit parameters and $\kappa_{a,b}$ is their correlation parameter. Thus, the density $\rho(r) \pm \Delta\rho(r)$ with its error band is obtained.

From the results obtained with different parameterizations the average value for the radius which is taken as a final result from the analysis is calculated using the

weighted mean method. The weighted mean and error of a number of uncorrelated measurements of a given quantity is given by:

$$\bar{x} \pm \delta\bar{x} = \frac{\sum_i \omega_i x_i}{\sum_i \omega_i} \pm \frac{1}{\sqrt{\sum_i \omega_i}} , \tag{4.35}$$

where

$$\omega_i = 1/(\delta x_i)^2 . \tag{4.36}$$

Here x_i and δx_i are the value and error obtained by the i^{th} measurement (in our case the fits with different density parameterizations) and the sum runs over the N measurements. Then $\chi^2 = \sum \omega_i(\bar{x} - x_i)^2$ is calculated and compared with $N - 1$. If $\chi^2/(N-1)$ is less than or equal to 1 and there are no known sources of big systematical errors, the results are accepted. Otherwise, if $\chi^2/(N-1)$ is very large the related result is not accepted. In the case of correlated data one should keep in mind that the error of the average value may be underestimated. More detailed information about the topic can be found in the Introduction of *Review of Particle Physics* by the *Particle Data Group* [74].

The SG, SF and GH parameterizations use the same one-body density distribution for all the nucleons in the nucleus. The GG, GO and GE parameterizations divide the nucleus a in core and halo component and use different one-body densities for the core and halo nucleons. In this case the number of nucleons in the halo is not a free parameter but is fixed a priori. In Table 4.2 are given the fit parameters for each density parameterization. From all the used densities only the SG parameterization does not allow a halo component in the density distribution and as will be seen later it gives a rather poor description of the experimental data for the isotopes of interest.

Parameterization	Fit parameters	N_{free}
SG	A_n, R_m	1
SF	A_n, R_0, a_0	2
GG	A_n, R_c, R_h	2
GO	A_n, R_c, R_h	2
GH	A_n, R_m, α	2
GE	A_n, R_c, R_h	2
SOG	A_n, $Amp_{G,i}$	$N_{gauss} + 1$

Table 4.2: Free parameters for the different density parameterizations. A_n is the overall normalization of the cross section, $Amp_{G,i}$ is the amplitude of the i^{th} Gaussian used in the SOG analysis and N_{gauss} is the number of Gaussian functions used.

It should be noted that connection between the form of the density and the angular distribution of the scattering is not reversible. If the density distribution is known one can calculate unambiguously the angular distribution of the cross section. But in the opposite case, when the angular distribution of the cross section for the scattering is measured it is possible that many densities with different form and parameters lead to the same angular distribution.

4.4 Sensitivity of the differential cross section for elastic proton scattering to the radial shape of the nucleus

The differential cross section for proton elastic scattering at small momentum transfer is particularly sensitive to the nuclear shape at the nuclear periphery but less sensitive to details of the shape in the central region of the nucleus. This makes it very useful for investigating halo nuclei where the surface is the most interesting part. With several simulation calculations based on the Glauber theory the sensitivity of the differential elastic scattering cross section to the halo structure of the nucleus can be investigated.

For the calculations the one-body densities have been parameterized with Gaussian functions. The calculations were performed for the nucleus ^{12}Be and only the region of low momentum transfer has been investigated.

In a first series of calculations it was assumed that ^{12}Be does not have a halo structure and for the nuclear density Gaussian distributions with radii 2.7, 2.8 and 2.9 fm were used. Then the corresponding scattering cross sections were calculated. In Fig. 4.3 the results are displayed, the density distributions on the left side and the

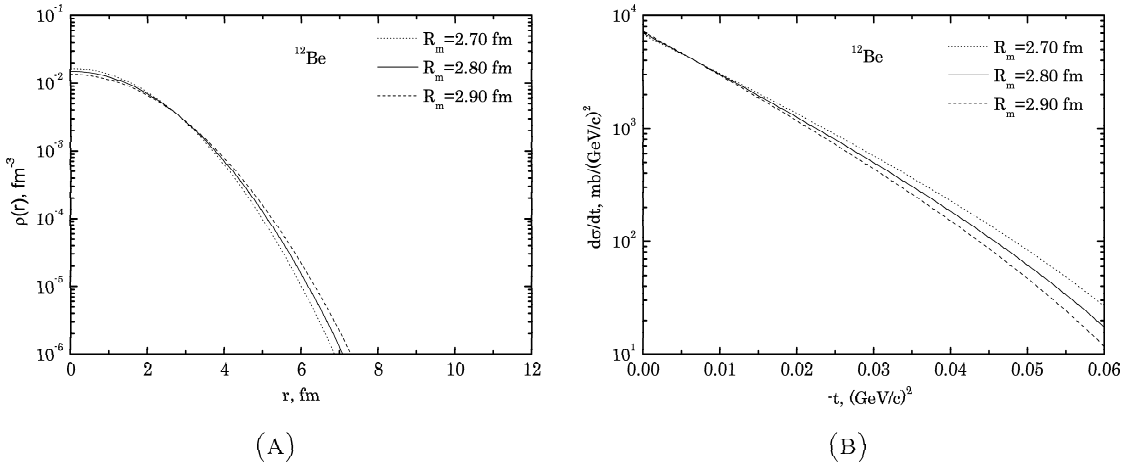

Figure 4.3: (A) Matter density distributions for ^{12}Be for a compact structure with different radii of the Gaussian function. (B) Differential cross sections corresponding to the matter distributions in (A). The slope of the cross section is strongly affected by the change in the matter radius.

cross sections on the right side. In a second series of calculations a halo structure of ^{10}Be core plus 2 valence neutrons was assumed and compared to the non-halo case. The core was approximated again with a Gaussian function with a radius 2.1 fm, and for the distribution of the valence particles a Gaussian density with a radius 5.0 fm was used. The *rms* radius of the core+2n system was again chosen to be 2.8 fm. The calculated densities and scattering cross sections are shown in Fig. 4.4 for the halo and no halo cases with the same matter radii. In this case the cross sections have been divided by an exponential function $C_0 exp(B_0 t)$ which makes the effect of the halo structure better visible. The coefficients C_0 and B_0 are the absolute value of the nuclear part of the scattering cross section at momentum transfer $t = 0$ (GeV/c)^2, and the slope of the cross section at low momentum transfer, respectively.

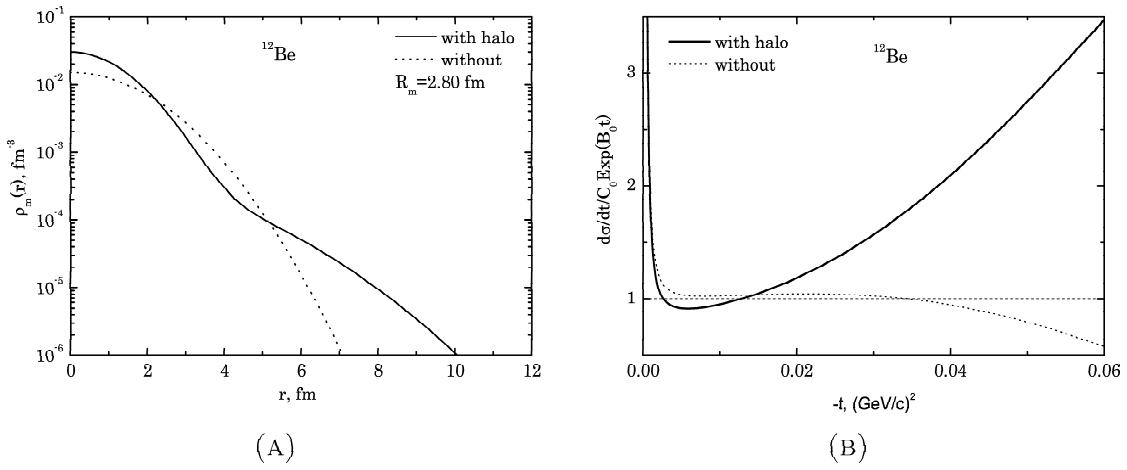

(A) (B)

Figure 4.4: (A) Matter density distributions for ^{12}Be assuming a one Gaussian parameterization (dotted line) and two Gaussian parameterization with separate core and halo distributions (solid line), both distributions having a matter radius R_{rms}=2.8 fm. (B) Differential cross section corresponding to the density distributions in (A). The presence of a halo structure leads to strong deviations from exponential behaviour of the cross section.

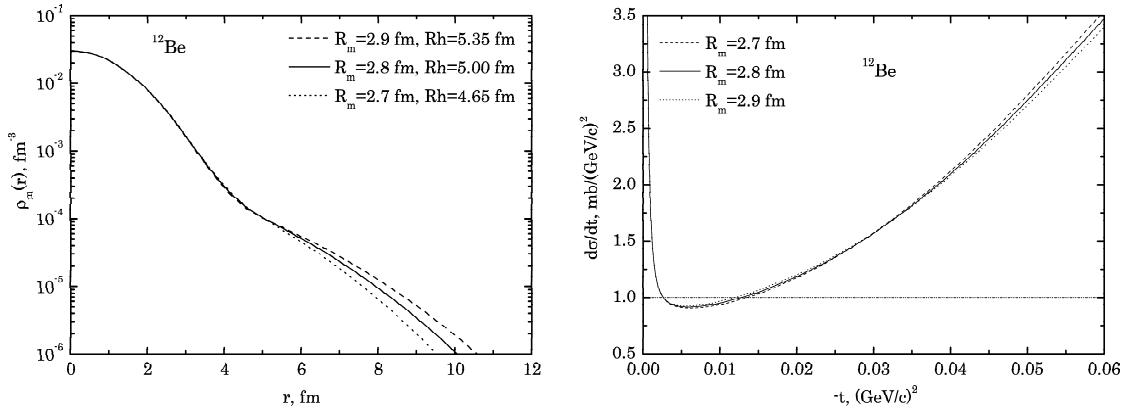

(A) (B)

Figure 4.5: (A) Matter density distributions for ^{12}Be assuming two Gaussian parameterization having the same core radius R_c=2.1 fm and different halo radii R_h. (B) Differential cross section corresponding to the density distributions in (A). The cross section is not sensitive to the behaviour of the tail at the far periphery.

From these results one comes to the conclusion that the slope of the cross section is directly related to the root mean square matter radius of the nucleus R_{rms} (see Fig. 4.3) and its curvature (deviation from exponential shape) reflects the presence of a halo component (see Fig. 4.4). On the other side it was found that the differential cross section at low momentum transfer is not sensitive to the behaviour of the halo at very large radii where the density becomes very small [9] (and where for halo nuclei an exponential behaviour with a slope of the exponent related to the halo nucleons separation energy is expected). In Figs. 4.5 and 4.6 densities with

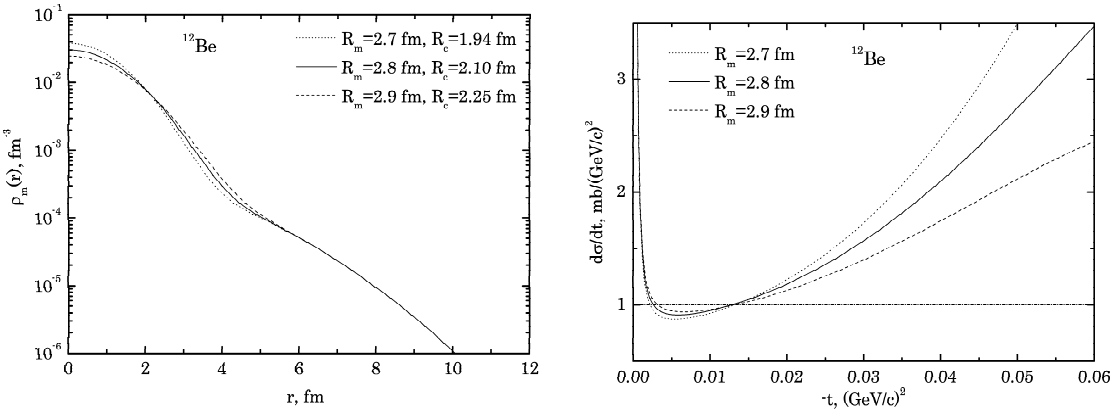

(A) (B)

Figure 4.6: (A) Matter density distributions for ^{12}Be assuming two Gaussian parameterization having the same halo radius R_h=5.0 fm and different core radii R_c. (B) Differential cross section corresponding to the density distributions in (A). The cross section shows sensitivity to the different matter radius which in this case is caused by different core radii.

different matter radii but the same core or halo radii are plotted, respectively. The conclusion is that differences in the matter radius which come from the different halo structure at the far periphery of the nucleus cannot be investigated with the present method as the differences in the cross section are very small (within the experimental error-bars) and our data are not sensitive to them. A good precision data at higher momentum transfer would reduce the uncertainties in the determined density distributions.

4.5 Theoretical predictions on the nuclear matter density distributions

Besides determining the density distributions by fitting the parameters of probe density functions to the experimental data, also matter densities calculated in microscopic nuclear models were used to calculate the differential cross section and compare it with the experimental one. In this case no fitting to the data was performed. A χ^2 method was used to estimate the quality of the theoretical description. This procedure can be used to test the theoretical predictions of different microscopic nuclear models. In this work densities from microscopic calculations within the fermionic molecular dynamics model and a few-body model were used.

4.5.1 *Matter density distributions calculated within the fermionic molecular dynamics model*

Molecular dynamics methods are used when correlations and fluctuations become important in the dynamical evolution of a many-body system. In the molecular dynamics the constituents of the system are represented by a few classical degrees

of freedom – like center of mass position and momentum, angle of rotation etc. – and interact through potentials.

In Fermionic Molecular Dynamics (FMD) the A-body basis states are parity and angular momentum projected Slater determinants $|Q\rangle$ [75, 26]:

$$|Q^{J^\pi}_{MK}\rangle = P^{J^\pi}_{MK}|Q\rangle \ , \tag{4.37}$$

of single-particle states $|q_l\rangle$:

$$|Q\rangle = \mathcal{A}\{|q_1\rangle \otimes \cdots \otimes |q_A\rangle\} \ . \tag{4.38}$$

The single-particle wave functions are described by Gaussian wave packets which are localized in phase-space:

$$\langle \mathbf{x}|q\rangle = \sum_i c_i \exp\{-\frac{(\mathbf{x}-\mathbf{b}_i)^2}{2a_i}\}|\chi_i\rangle \otimes |\xi\rangle \ . \tag{4.39}$$

The complex width a of the Gaussians is considered as an additional degree of freedom. The spins $|\chi_i\rangle$ of each packet can take any direction. The single-particle parameter $\mathbf{b} = \mathbf{r} + ia\mathbf{p}$ is related to the mean position and the mean momentum. The isospin part $|\xi_l\rangle$ is taken to be time independent and identifies either a proton or a neutron. A superposition of two Gaussian wave packets is used for each single-particle state $|q_i\rangle$ which gives improved description for light nuclei.

The many-particle state is determined by minimizing the intrinsic energy of the parity projected Slater determinant:

$$E[|Q^\pi\rangle] = \frac{\langle Q^\pi|H_{eff} - T_{cm}|Q^\pi\rangle}{\langle Q^\pi|Q^\pi\rangle} \tag{4.40}$$

with respect to the parameters of all single-particle states. Additional configurations are created by imposing constraints, like a certain radius or quadrupole moment, on the states. The symmetries of the Hamiltonian are restored by performing projections on parity, angular momentum and a center of mass momentum of zero. A multi-configuration calculation is done by diagonalizing the Hamiltonian in this subspace. In all cases effective interaction derived from the realistic Argonne V18 potential by means of the Unitary Correlation Operator Method (UCOM) is used. From the multi-configuration ground state the nuclear matter density is calculated as the Fourier transform of the form factor. Within the FMD model, ground-state properties like binding energies and *rms* radii can be reproduced well for light nuclei [26].

4.5.2 *Few-body model calculations*

Within the three-body model used to calculate the ground state properties of ^{12}Be and ^{14}Be these nuclei are represented as a *core*+2*n* system and the total wave function has the form $\Phi = \phi_c(\xi_c)\Psi^\pi_{JM}(1,2)$ [76]. The total wave function is a product of the intrinsic wave function ϕ_c of the inactive core (depending on the intrinsic coordinates ξ_c) and the active part $\Psi(1,2)$ which depends on the relative coordinates and

spins of the valence neutrons. $\Psi(1,2)$ is the solution of the three-body Schrödinger equation:

$$(\hat{T} + \hat{V} + E)\Psi(1,2) = 0 \quad , \text{ where } \quad \hat{V} = \hat{V_{c1}} + \hat{V_{c2}} + \hat{V_{12}} \ . \tag{4.41}$$

Within the few-body representation the ^{12}Be nucleus is sought as a solution of a three-body problem for two neutrons located outside a ^{10}Be core [25]. The potentials are defined such that the two-body subsystem n+^{10}Be has the known eigenstates of ^{11}Be. Several potentials are used for calculating the ground state binding energy in ^{12}Be starting from a potential that describes ^{11}Be and increasing the s-, p- and d-wave strengths, separately and together, in order to reproduce the experimental binding energy of ^{12}Be:

- **A:** reproduces all the eigenstates in ^{11}Be,
- **B1:** increased p-wave potential,
- **B2:** increased s-wave potential,
- **B3:** increased s- and p-wave potentials together,
- **B4:** increased d-wave potential,
- **B5:** increased s-, p- and d-wave potentials; reproduces the experimental binding energy in ^{12}Be.

In a similar way different density distributions were calculated for ^{14}Be [25]. This isotope is represented in a three-body model as a ^{12}Be closed p shell core plus two valence neutrons. As the p shell is full the valence neutrons of ^{14}Be can occupy orbitals in the sd shell ($1s_{1/2}$ and $0d_{5/2}$). The different calculations assume different mixing between these orbitals:

- **C4:** the valence neutrons occupy mainly the d shell (96%), with 1% in the s shell; reproduces the experimental two-neutron separation energy,
- **C7:** mixing with 29% s-wave and 67% d-wave,
- **C9:** 83% s-wave plus 14% d-wave,
- **D4:** mainly s state, with 86% s-wave and 10% d-wave.

Details about both calculations can be found in [25, 77].

CHAPTER 5

Experimental results

5.1 Results for ^{14}Be

5.1.1 *Nuclear matter density distribution and matter radius of ^{14}Be*

The obtained differential cross section for p-^{14}Be elastic scattering was analyzed using a number of density parameterizations with the Glauber theory (see Section 4.2). The results from the fitting with the different parameterizations are listed in Table 5.1. The single Gaussian parameterization, which does not allow for an extended matter distribution, does not give a good description of the experimental data (Fig. 5.1).

On the other side, a good description of the experimental cross section is obtained with the symmetrized Fermi parameterization (Fig. 5.2). A very big value for the diffuseness parameter $a = 0.8$ is obtained which is an indication for the existence of a halo structure in ^{14}Be.

The results from the analysis with the GH parameterization are shown in Fig. 5.3. The parameter α determines the contribution of the halo component which is the biggest when $\alpha = 0.4$. In the case of ^{14}Be the obtained value is $\alpha = 0.14$ which indicates the presence of a relatively small halo component.

Further analysis was done assuming core plus halo structure of ^{14}Be. First a ^{12}Be core plus two halo neutrons structure was assumed. The core was parameterized with a Gaussian function and the two halo neutrons consecutively with Gaussian, harmonic oscillator and exponential functions. The three model densities give equally good description of the experimental data and the results for the radii are consistent (Table 5.1). The obtained densities and the fits to the experimental cross section are presented in Figs. 5.4, 5.5 and 5.6 for the GG, GO and GE models, respectively. For the core a mean radius $R_c = 2.65 \pm 0.02 \pm 0.12$ fm was determined and for the halo $R_h = 5.40 \pm 0.31 \pm 0.21$ fm. The first error includes the statistical

Parameterization	R_m, fm	Fit parameters A_n	Density parameters		χ^2/N
SG	2.86(3)	1.12(1)	-	-	48/32
SF	3.06(8)	1.07(1)	$R_0 = 1.00(40)$	$a = 0.80(1)$	25/32
GG	3.20(13)	1.06(2)	$R_c = 2.67(3)$	$R_h = 5.39(54)$	28/32
GO	3.15(10)	1.07(2)	$R_c = 2.62(3)$	$R_h = 5.30(37)$	26/32
GH	3.10(6)	1.06(2)	$R_m = 3.10(6)$	$\alpha = 0.14(2)$	24/32
GE	3.28(16)	1.06(2)	$R_c = 2.67(3)$	$R_h = 5.70(64)$	28/32
SOG	2.95(4)	0.96(3)	-	-	22/26

Table 5.1: Parameters obtained by fitting the experimental cross section for p-^{14}Be elastic scattering using the parameterizations SF, SG, GG, GO, GII, GE and SOG of the density distribution. The presented parameters refer to point-nucleon density distributions. Only statistical errors are given. The parameters are as follows: R_m - root mean square matter radius; R_c - radius of the nuclear core; R_h - radius of the halo; N - number of degrees of freedom; A_n - normalization of the calculated cross section. A_n and α are dimensionless, all other fit parameters are in fm.

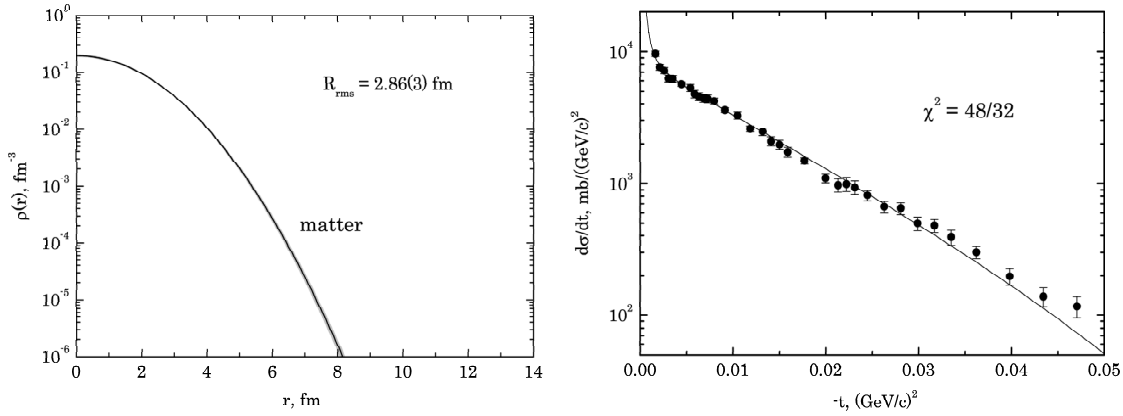

Figure 5.1: Results obtained with the Single Gaussian parameterization. Total nuclear matter density distribution of ^{14}Be (left); comparison between the experimental data and the fit with the SG parameterization (right).

error and the model uncertainties (the weighted mean of the errors from different parameterizations) and the second error is the systematical error which includes the 4% error in the absolute normalization of the cross section and the error coming from the use of the experimentally known free pN scattering amplitudes in the theoretical analysis which is evaluated to 0.04 fm [9].

An independent sum of Gaussian analysis was performed using seven Gaussian functions distributed from 0 to 12 fm with a width of $\gamma = 1.2$ fm. The results from the analysis are shown in Fig. 5.7. This parameterization also gives a good description of the experimental data and shows a small halo component in the matter distribution.

A comparison of the cross sections calculated with all the density parameterizations with the experimental data is shown in Fig. 5.8. The cross sections are divided by an exponential function to enhance the halo effect on the cross section. The C_0

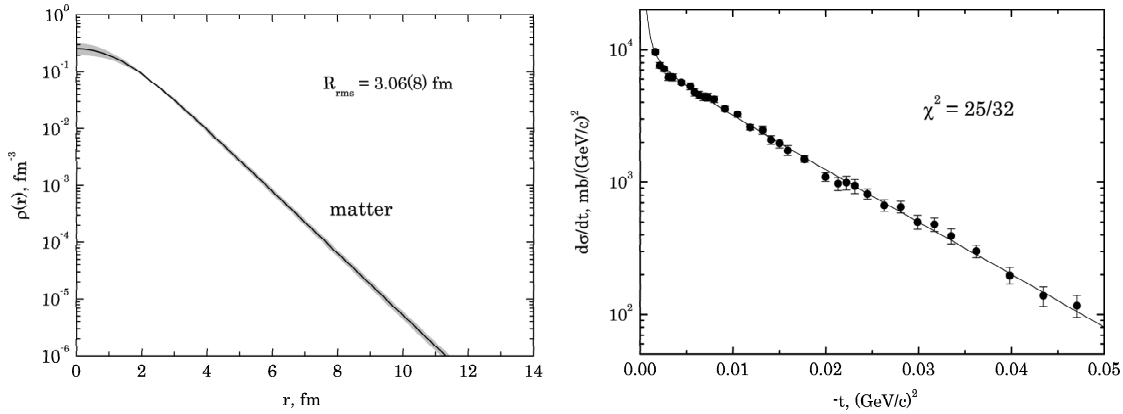

Figure 5.2: Results obtained with the Symmetrized Fermi parameterization. Total nuclear matter density distribution of ^{14}Be (left); comparison between the experimental data and the fit with the SF parameterization (right).

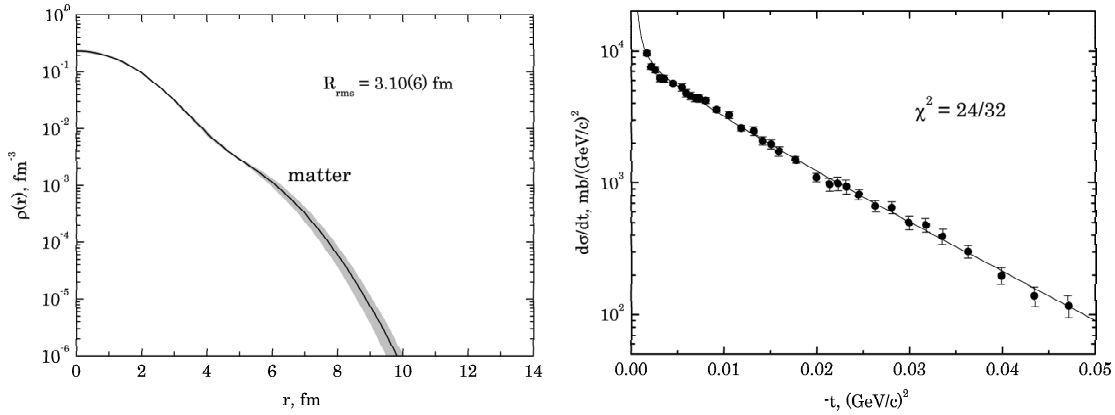

Figure 5.3: Results obtained with the Gauss-halo parameterization. Total matter density distribution of ^{14}Be (left); comparison between the experimental data and the fit with the GH parameterization (right).

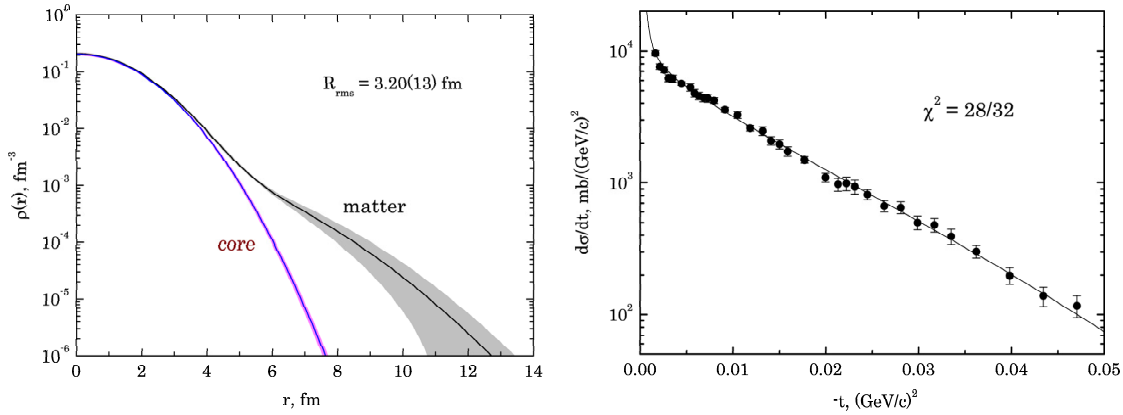

Figure 5.4: Results obtained with the Gauss-Gauss parameterization. Core and matter density distribution of ^{14}Be (left); comparison between the experimental data and the fit with the GG parameterization (right).

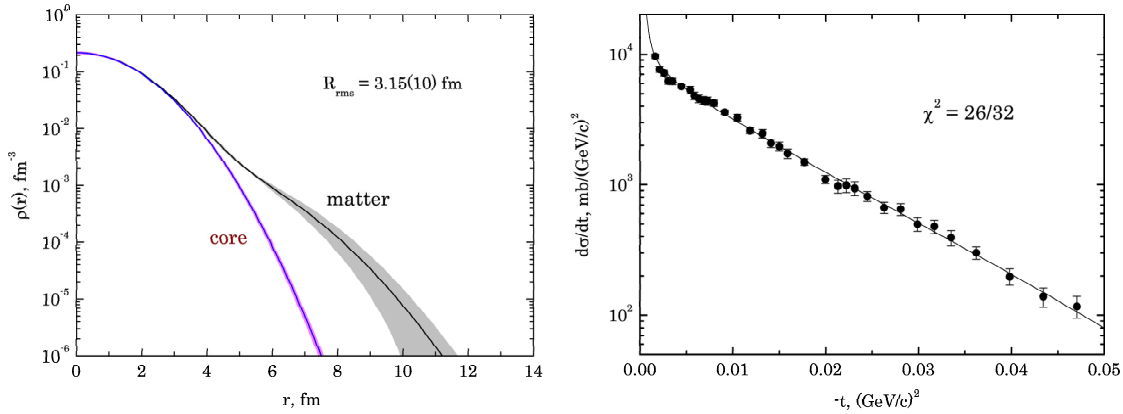

Figure 5.5: Results obtained with the Gauss-oscillator parameterization. Core and matter density distribution of ^{14}Be (left); comparison between the experimental data and the fit with the GO parameterization (right).

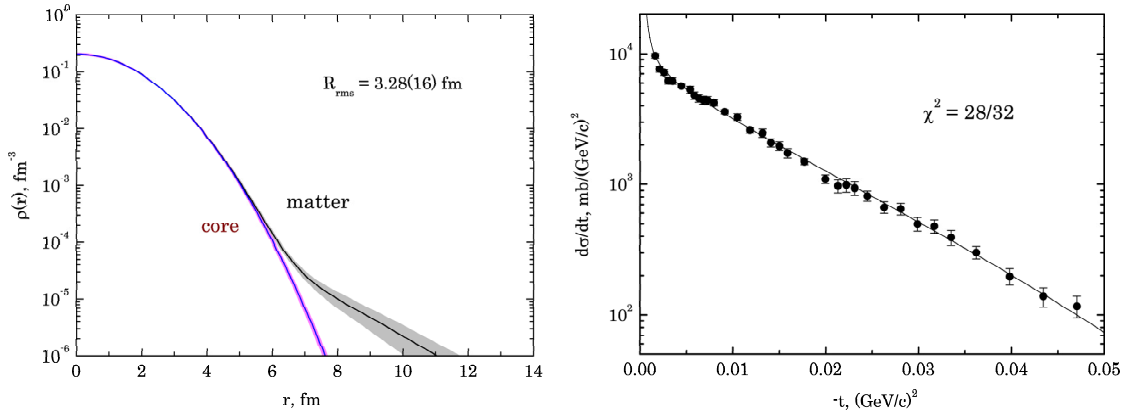

Figure 5.6: Results obtained with the Gauss-Exponential parameterization. Core and matter density distribution of ^{14}Be (left); comparison between the experimental data and the fit with the GE parameterization (right).

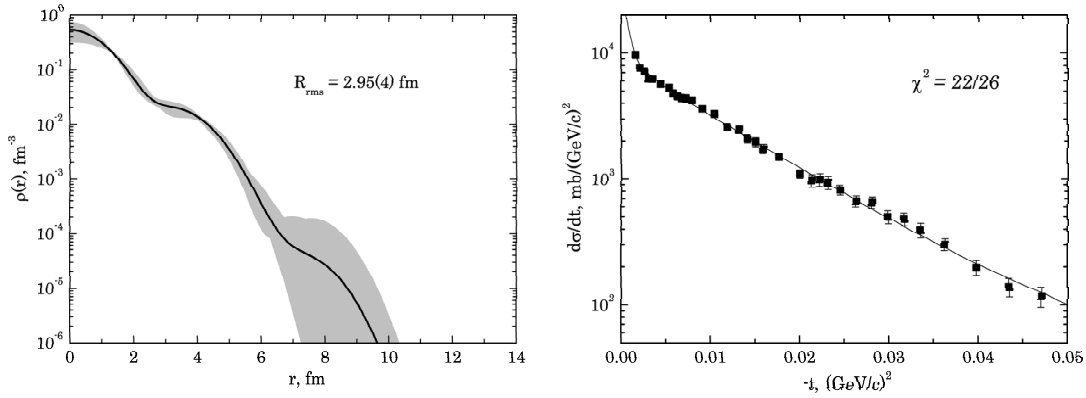

Figure 5.7: Results obtained with the sum of Gaussian analysis. Total nuclear matter density distribution of ^{14}Be (left); comparison between the experimental data and the fit with the SOG parameterization (right).

coefficient is the value of the nuclear part of the differential cross section calculated with the GO parameterization at four-momentum transfer $t = 0$ $(\mathrm{GeV/c})^2$ and B_0 is the slope of this cross section at small momentum transfer. The results show the characteristic behaviour for a halo structure except for the SG model which does not describe the data well. This behaviour is interpreted as due to the fact that the SG parameterization does not allow for a halo structure.

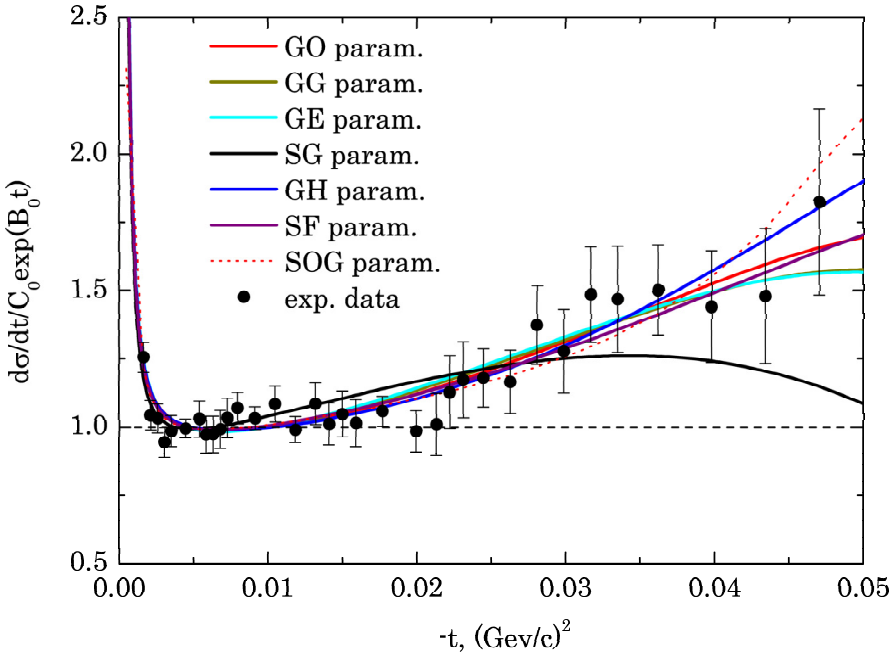

Figure 5.8: Experimental differential cross section for proton elastic scattering on ^{14}Be as a function of the four momentum transfer $-t$ (black points), compared with the fitted cross sections obtained on the basis of different density parameterizations (lines). All data are divided by an exponential function to better visualize the halo structure. Note that the SG parameterization gives a bad description due to the fact that no halo structure can be described with it.

The values for the deduced matter radius R_m with the different density parameterizations are consistent within errors except for the SG (see above) and SOG parameterizations. There is no good explanation yet why the SOG analysis gives inconsistent results even though the χ^2 of the fit is good. The fact that this model gives completely different absolute normalization was a reason not to include it when calculating the average density and matter radius. The GE parameterization gives bigger radius than the rest of the parameterizations due to the different behaviour of the density tail at large radii. Due to the exponential fall of the density the contribution of the tail to the *rms* radius is much bigger than in the other cases. As the data from this experiment are not sensitive to the behaviour of the density at large radii this parameterization was also not included when calculating the average values which might lead to a systematically underestimated matter radius.

To construct an average density the results from the SF, GG, GO and GH parameterizations were used. The average matter density with its error-band, given as the sum of the error-bands from all the models, is plotted in Fig. 5.9. From the

results obtained with this models a weighted mean *rms* radius for ^{14}Be:

$$R_m = 3.11 \pm 0.04 \pm 0.13 \ \text{fm} \tag{5.1}$$

was deduced including the statistical and systematical errors.

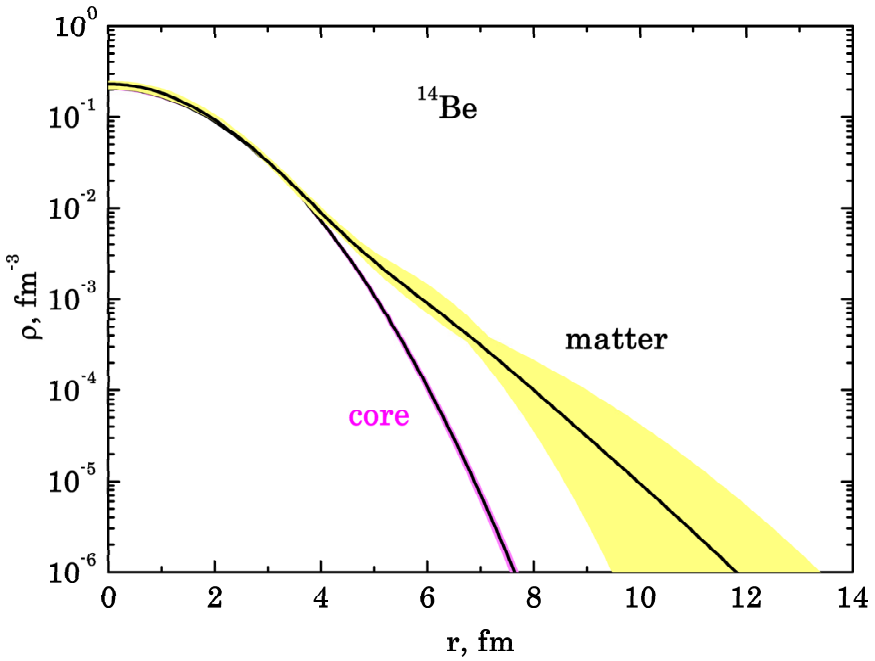

Figure 5.9: Average density distribution of ^{14}Be isotope. For the average the densities deduced with the SF, GG, GH and GO parameterizations were used and the error-band was created as the sum of all the individual error-bands.

Another analysis was performed assuming ^{10}Be core plus four neutron structure of ^{14}Be. This analysis gives consistent results for the matter radius R_m and the normalization A_n with the ones obtained when a two-neutron halo is assumed. This leads us to the conclusion that the data from this experiment are not sensitive to the number of halo particles but only to the total matter density.

5.1.2 *Comparison with experimental results from other experiments*

In Table 5.2 a comparison is made between the value obtained for the matter radius of ^{14}Be in this experiment and the results from previous experimental studies performed with different experimental methods. Within errors the present result is consistent with the results from the other experiments. One can see from Table 5.2 that the results obtained from the measurement of the total interaction cross section depend very much on the model and the parameterizations used for the analysis and different results are obtained. The present results are least model dependent as many density parameterizations were used and their average was taken as a final result, and they have very good accuracy (one of the smallest errors).

Experimental method	Analysis model	R_m, fm	Ref.
Elastic scattering	Glauber theory	3.11(14)	this work
Interaction cross section	Glauber theory	3.11(38)	[19]
Interaction cross section	Glauber theory	3.16(38)	[19]
Interaction cross section	few-body description	3.10(15)	[22]
Interaction cross section	optical limit Glauber	2.94(9)	[22]
Reaction cross section	microscopic model	3.36(19)	[21]

Table 5.2: Comparison of the current results for the isotope ^{14}Be with results obtained in previous experimental studies. When the Glauber theory was used for the analysis, different density parameterizations were used in the different cases.

5.1.3 *Comparison with theoretical calculations from microscopic models*

The experimental cross section was used to probe several theoretical predictions on the nuclear matter density distribution of ^{14}Be. Microscopic theoretical densities were used to calculate the differential cross section within the Glauber theory. In this case no fitting was performed. The calculated cross sections when few-body densities were used are plotted in Fig. 5.10 and the densities are compared with the average density obtained from the present analysis. For the case when microscopic density from FMD calculation was used, the results are shown in Fig. 5.11. Both theoretical models suppose a halo structure of the nucleus. In Table 5.3 the theoretical radii and the χ^2 of the calculated cross sections compared to the experimental data are given. The best description of the experimental data is obtained with the C9 and D4 versions of the few-body calculations. In this case there is also a very good agreement between the theoretical and experimental values for the total matter radius, the halo and the core radius. The comparison between theory and experiment supports a structure for ^{14}Be where the valence nucleons occupy mainly the $s_{1/2}$ orbital with 10-15% admixture of $d_{5/2}$ [25].

Model	R_m, fm	R_h, fm	R_c, fm	χ^2	Ref.
Elastic scattering	3.11(14)	5.40(37)	2.65(12)	–	this work
C4	2.80	3.68	2.59	7.30	[25]
C7	2.96	4.41	2.59	5.07	[25]
C9	3.44	6.30	2.59	2.06	[25]
D4	3.18	5.35	2.59	2.92	[25]
FMD	2.94	–	–	4.35	[26, 78]

Table 5.3: The root mean square radii R_m, R_h and R_c for ^{14}Be determined with different versions of theoretical model calculations and χ^2 from a comparison of the calculated cross section with the experimental one.

Within the FMD model the α-clustering in the nucleus is studied [26]. In this case the theoretical calculation does not agree very well with the experimental data, therefore no final conclusions about that can be made on the basis of the present experiment.

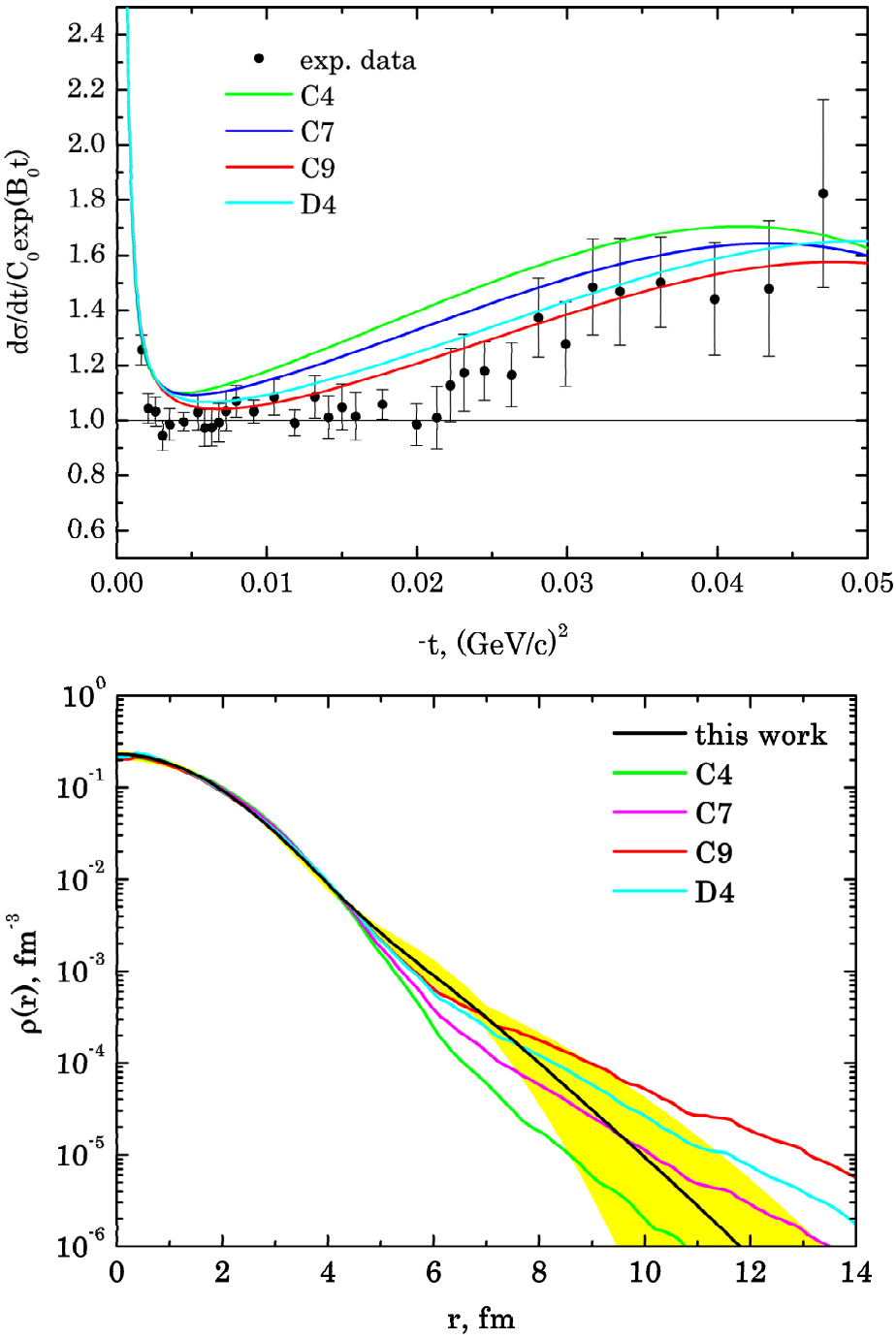

Figure 5.10: Differential cross section for p-^{14}Be elastic scattering calculated with a theoretical density distribution from few-body calculations compared to the experimental one (top). Few-body nuclear matter density distributions compared to the average matter distribution of ^{14}Be deduced from the present experiment (bottom). Best agreement with the experimental data is obtained with the C9 and D4 theoretical densities.

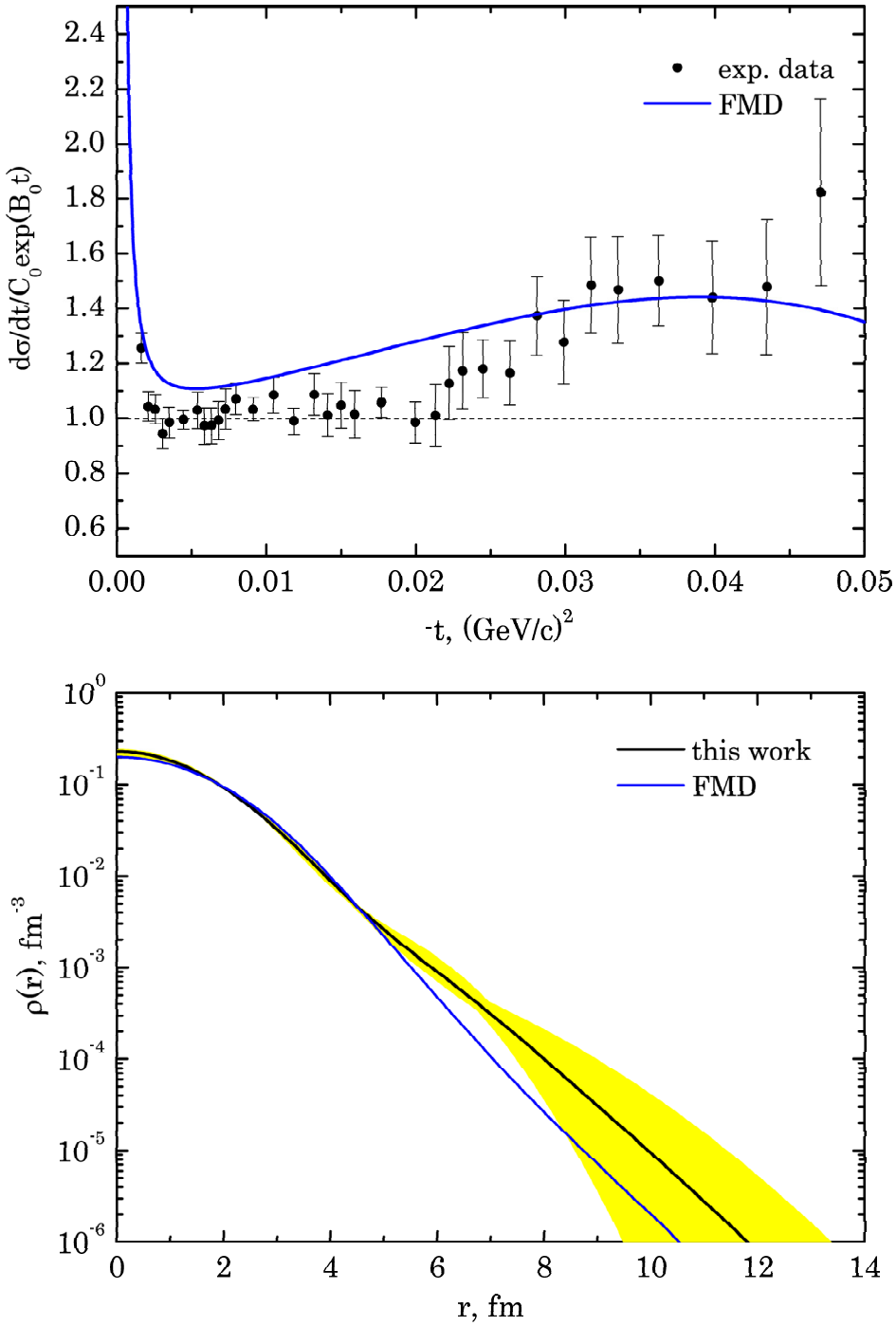

Figure 5.11: Differential cross section for p-^{14}Be elastic scattering calculated with a theoretical density distribution from FMD calculations compared to the experimental one (top). FMD nuclear matter density distribution compared to the average matter distribution of ^{14}Be deduced from the present experiment (bottom).

5.2 Results for ^{12}Be

5.2.1 *Nuclear matter density distribution and matter radius of ^{12}Be*

The results from the analysis of the experimental data for the nucleus ^{12}Be using different density parameterizations are presented in Table 5.4. In the case of ^{12}Be both symmetrized Fermi and single Gaussian parameterizations give bad description of the experimental data. The fits and the deduced density distributions are shown in Figs. 5.13 and 5.12 for both parameterizations, respectively. In these cases, the calculation substantially differs from the experiment at high momentum transfer t. The discrepancy with the experimental data is a strong indication for the presence of a halo component in the ^{12}Be structure.

Parameterization	R_m, fm	Fit parameters A_n	Density	parameters	χ^2/N
SG	2.43(2)	1.08(1)	-	-	127/42
SF	2.55(9)	1.04(1)	$R_0 = 1.00(36)$	$a = 0.65(1)$	74/42
GG	3.00(13)	1.00(1)	$R_c = 2.20(2)$	$R_h = 5.47(40)$	38/42
GO	2.91(9)	1.00(1)	$R_c = 2.14(2)$	$R_h = 5.28(26)$	34/42
GH	2.78(5)	0.99(1)	$R_m = 2.78(5)$	$\alpha = 0.25(2)$	33/42
GE	3.09(15)	1.00(2)	$R_c = 2.20(2)$	$R_h = 5.75(46)$	41/42
SOG	2.80(5)	1.02(3)	-	-	36/36

Table 5.4: Parameters obtained by fitting the experimental cross section for p-^{12}Be elastic scattering using the parameterizations SF, SG, GG, GO, GH, GE and SOG of the density distribution. The presented parameters refer to point-nucleon density distributions. Only statistical errors are given. The parameters are as follows: R_m - root mean square matter radius; R_c - radius of the nuclear core; R_h - halo radius; N - number of degrees of freedom; A_n - normalization of the calculated cross section. A_n and α are dimensionless, all other fit parameters are in fm.

The GH parameterization gives one of the best fits. The results are presented in Fig. 5.14. This parameterization supports an extended matter distribution in ^{12}Be (the parameter $\alpha = 0.26$ is very close to the upper limit of 0.4).

Other density parameterizations were used for ^{12}Be as well, where its structure was assumed to be a ^{10}Be core and two valence neutrons. For the core again a Gaussian function was used and for the valence neutrons Gaussian, harmonic oscillator and exponential functions. The results are plotted in Figs. 5.15, 5.16 and 5.17, respectively. All of them indicate a rather large halo component. The GE parameterization gives a relatively large matter radius, comparable with the ^{14}Be matter radius, which is due to the slow exponential fall of the density at large radii. The results for the core and halo radii obtained with these three parameterizations are consistent within errors (see Table 5.4). The core radius was determined to be $R_c = 2.18 \pm 0.02 \pm 0.10$ fm and the halo radius – $R_h = 5.41 \pm 0.23 \pm 0.22$ fm.

The more model independent sum of Gaussian analysis was also performed. For the analysis a basis of ten Gaussian functions distributed in the range of 0 to 15 fm

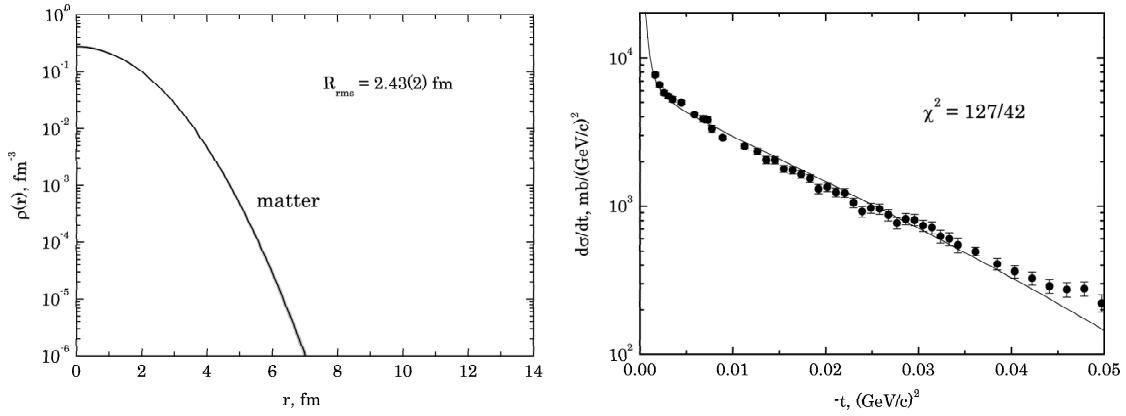

Figure 5.12: Results obtained with the Single Gaussian parameterization. Total nuclear matter density distribution of ^{12}Be (left); comparison between the experimental data and the fit with the SG parameterization (right).

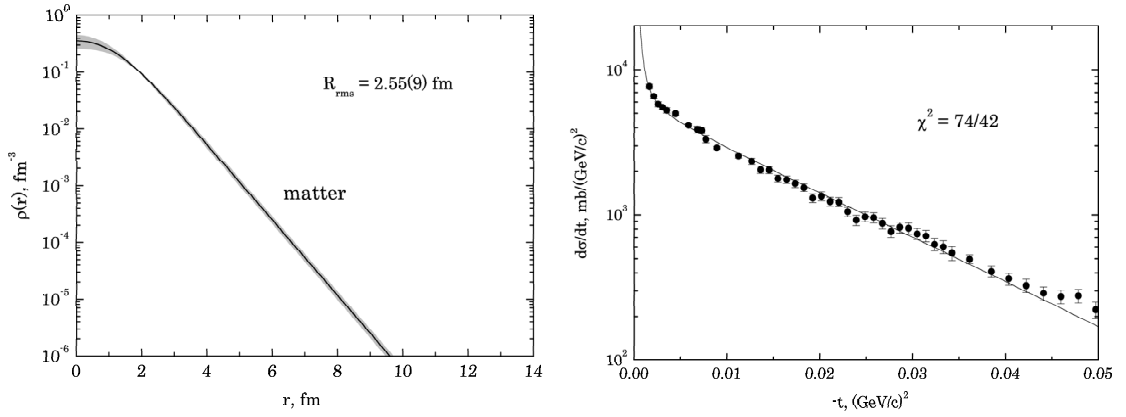

Figure 5.13: Results obtained with the Symmetrized Fermi parameterization. Total nuclear matter density distribution (left); comparison between the experimental data and the fit with the SF parameterization (right).

with a width $\gamma = 1.4$ fm was used. The resulting description is very good and comparable to the one with GH density parameterization. For the fit 200 different sets of positions for the Gaussians were generated and the amplitudes of the Gaussians were fitted to the experimental data. The deduced density distribution with its 1σ error-band and the corresponding calculated cross section are plotted in Fig. 5.18.

The differential cross sections calculated with the different density parameterizations are compared in Fig. 5.19. The cross sections are again divided by an exponential function and from the plot the presence of a halo structure is obvious. The SG and SF parameterizations which do not allow a halo component apparently do not describe the cross section well at high momentum transfer t. The present analysis strongly suggests that the last two neutrons in ^{12}Be have an extended distribution. This supports the hypothesis of shell breaking around the $N = 8$ magic number (see Section 1.3). ^{12}Be does not have the low separation energy typical for a halo nucleus and ^{11}Be is bound but due to the observed extended distribution a non-Borromean halo structure of ^{12}Be is supported [79].

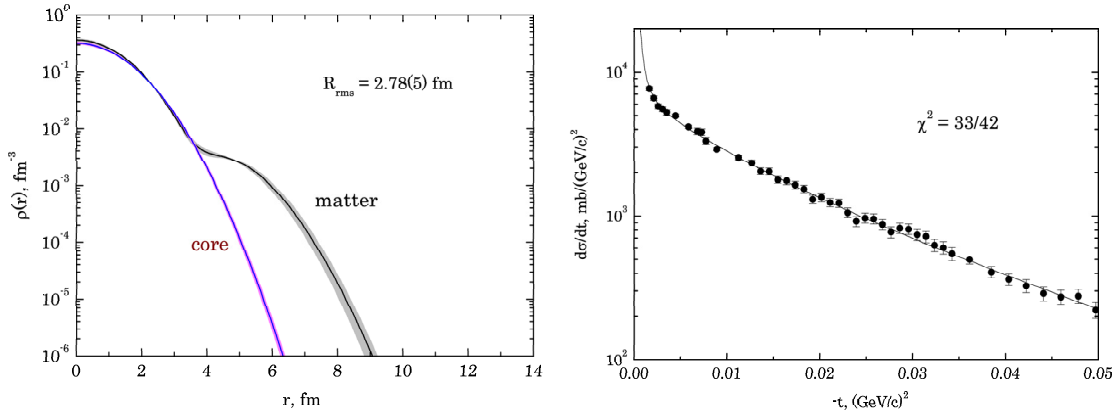

Figure 5.14: Results obtained with the Gauss-halo parameterization. Total matter density distribution of ^{12}Be (left); comparison between the experimental data and the fit with the GH parameterization (right).

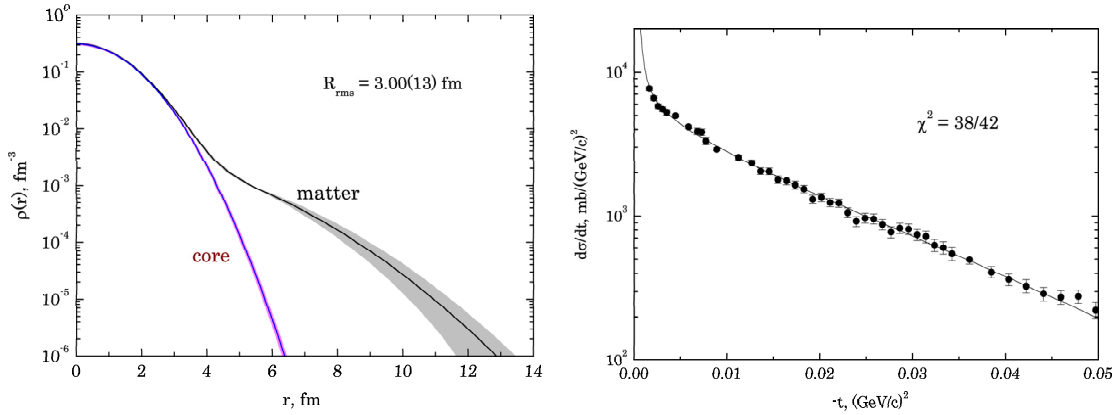

Figure 5.15: Results obtained with the Gauss-Gauss parameterization. Core and matter density distribution of ^{12}Be (left); comparison between the experimental data and the fit with the GG parameterization (right).

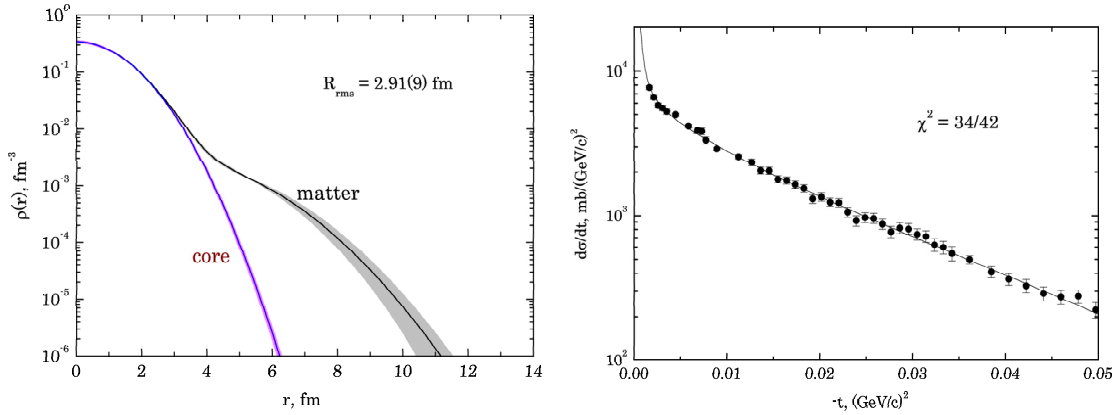

Figure 5.16: Results obtained with the Gauss-oscillator parameterization. Core and matter density distribution of ^{12}Be (left); comparison between the experimental data and the fit with the GO parameterization (right).

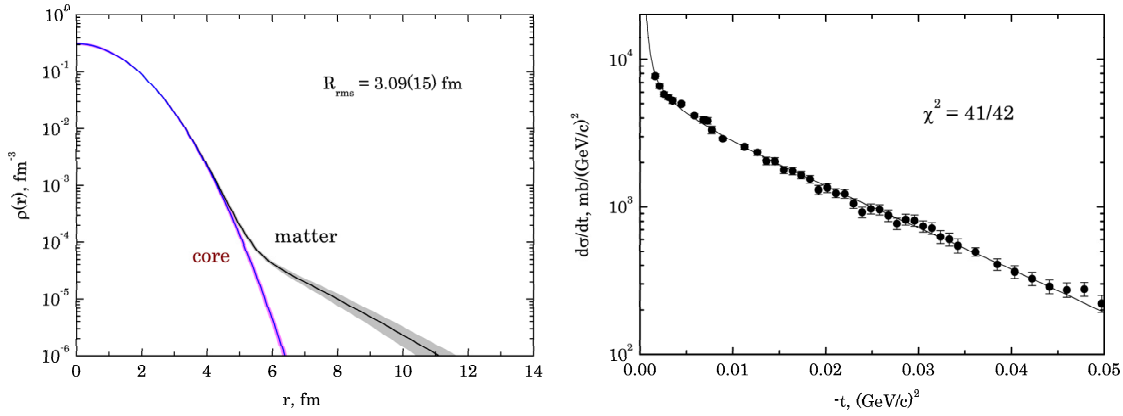

Figure 5.17: Results obtained with the Gauss-Exponential parameterization. Core and matter density distribution of ^{12}Be (left); comparison between the experimental data and the fit with the GE parameterization (right).

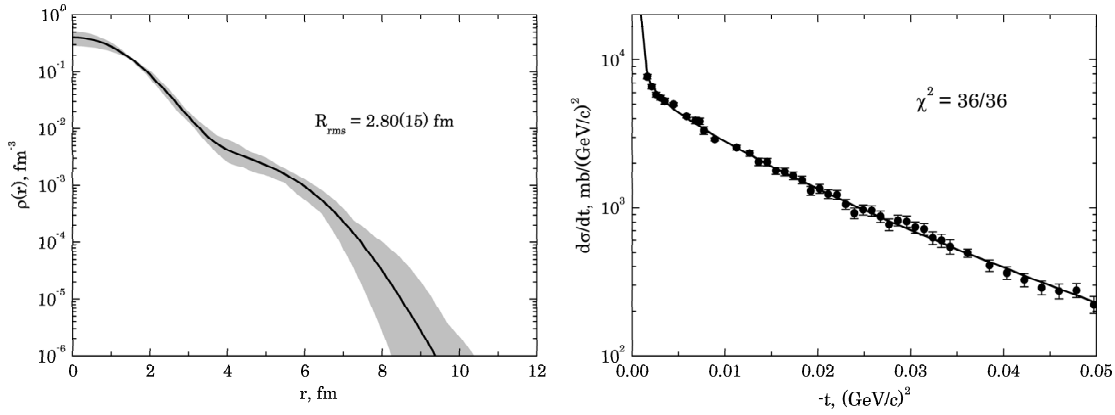

Figure 5.18: Nuclear matter density distribution of ^{12}Be deduced with the sum of Gaussian analysis. Total nuclear matter density distribution of ^{14}Be (left); comparison between the experimental data and the fit with the SOG parameterization (right).

Except for the SG and SF parameterization, all other densities give consistent results within errors for the matter radius R_m of ^{12}Be and for the normalization of the calculated cross section A_n. This allows us to regard the average results as model independent. In Fig. 5.20 the average density of ^{12}Be is plotted. The average is constructed from the density parameterizations GG, GO, GH and SOG and the error-band is constructed as the sum of the error-bands of all the four densities. The GE parameterization was not included in the average due to the different behaviour of the density at large radii as discussed in the case of the ^{14}Be isotope.

The average matter root mean square radius deduced from the present analysis of the data was calculated from the radii deduced from the GG, GO, GH and SOG parameterizations. For ^{12}Be the *rms* radius is:

$$R_m = 2.82 \pm 0.03 \pm 0.12 \ \text{ fm} \ , \tag{5.2}$$

including the statistical error and a systematic error coming from the error in the absolute normalization and the errors introduced to the analysis from the free pp

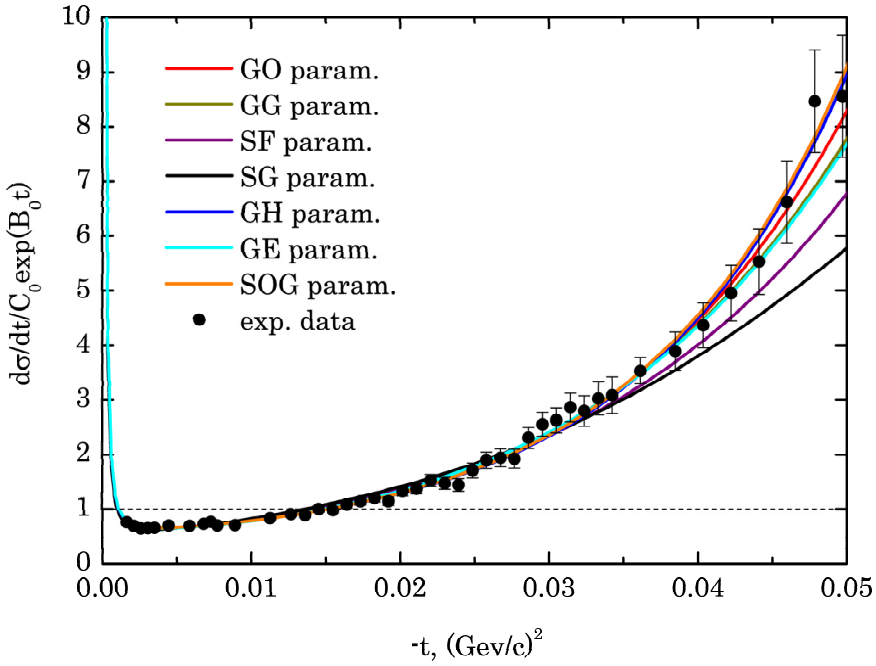

Figure 5.19: Experimental absolute differential cross section for proton elastic scattering on ^{12}Be as a function of the four momentum transfer $-t$ (black points), compared with the fitted cross sections obtained on the basis of different phenomenological density parameterizations (lines). All data are divided by exponential function to better visualize the halo structure. The SG and SF density distributions give the worst descriptions.

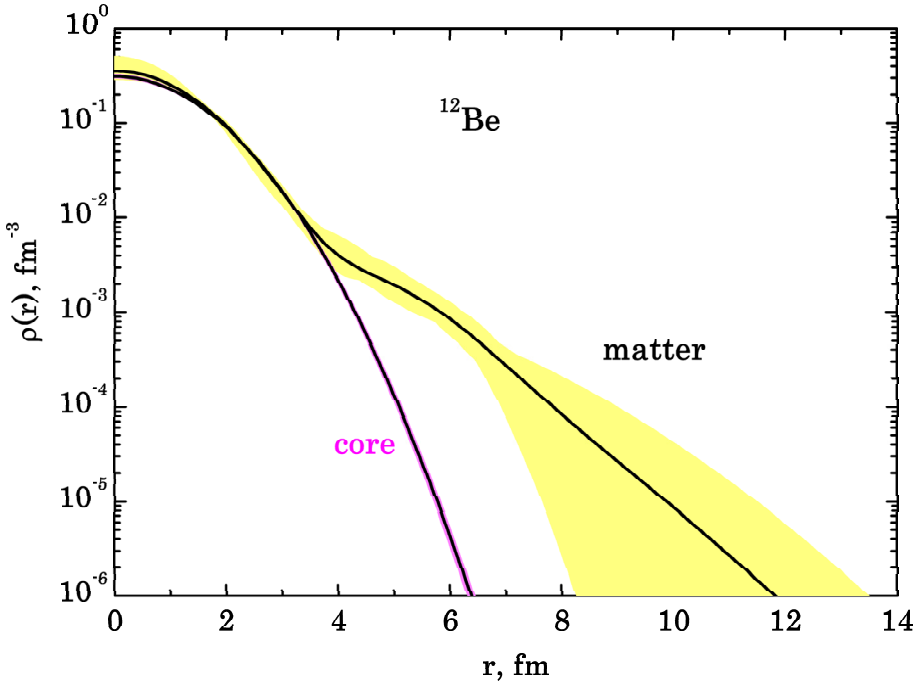

Figure 5.20: Average density distribution of ^{12}Be isotope. For the average the densities deduced with the GG, GH, GO and SOG parameterizations were used and the error-band was created as the sum of all the individual error-bands.

and pn scattering amplitudes.

^{12}Be is adopted as the core of the halo nucleus ^{14}Be. The comparison between the core size of ^{14}Be (R_c = 2.65(12) fm) and the matter radius of ^{12}Be (R_m = 2.82(12) fm) indicate that the free ^{12}Be and the core have different behavior (see Fig. 5.21). When free, ^{12}Be exhibits an extended structure. In this mass region

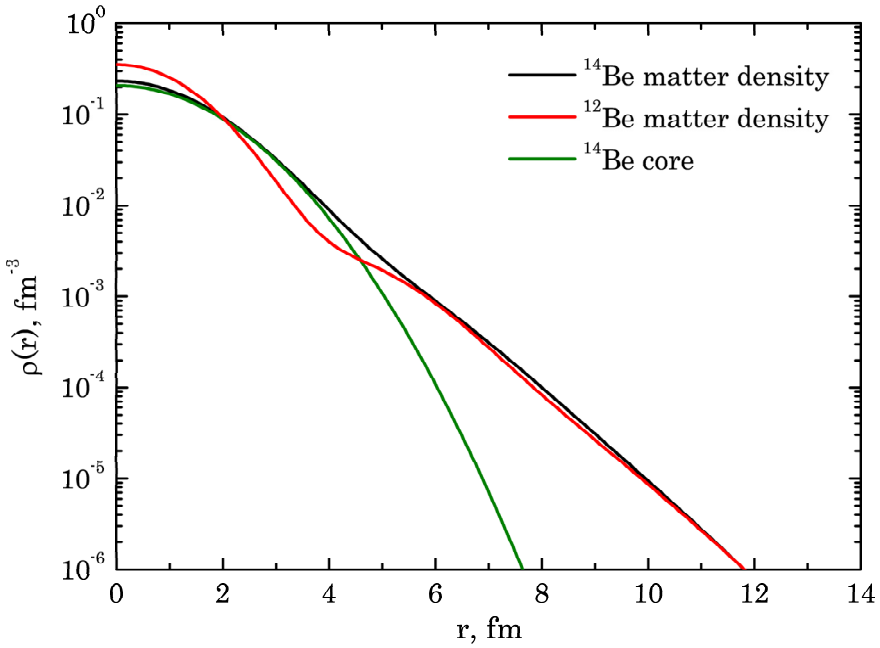

Figure 5.21: Comparison between the total matter density of ^{12}Be with the total matter density and the core density of ^{14}Be. When bound in ^{14}Be, the ^{12}Be nucleus has much more compact structure.

breaking of the $N = 8$ neutron shell closure is observed due to intruder orbitals from the next *sd* shell. This leads to an extended matter distribution due to neutrons on the $s_{1/2}$ orbital. While, when ^{12}Be is within the ^{14}Be nucleus most probably its last neutrons occupy the *p* shell which is the available one.

5.2.2 *Comparison with experimental results from other experiments*

The size of ^{12}Be has been investigated before in a number of experiments. In Table 5.5 the previous results are summarized and compared to the radius measured in this experiment. In this case we obtain slightly larger radius than the ones obtained with the previous measurements.

Experimental method	Analysis model	R_m, fm	Ref.
Elastic scattering cross section	Glauber theory	2.82(12)	this work
Interaction cross section	Glauber theory	2.57(5)	[19]
Interaction cross section	Glauber theory	2.59(6)	[19]
Reaction cross section	microscopic model	2.62(7)	[21]

Table 5.5: Comparison of the present results on R_m for the nucleus ^{12}Be with previous experimental studies. When the Glauber theory was used for the analysis different density parameterizations were used in the different cases.

5.2.3 *Comparison with theoretical calculations from microscopic models*

Theoretical densities were used to calculate the elastic scattering cross sections with the Glauber approach and the calculations were compared with the experimental data. The cross section corresponding to the few-body calculation and the calculated density [25] are shown in Fig. 5.22 and the FMD microscopic density and cross section [26, 78] are shown in Fig. 5.23, respectively. The theoretical radii and the obtained χ^2 from the comparison of the calculated cross sections with the experimental one are compared in Table 5.6. All these models do not describe the experimental data well in the whole region of momentum transfer, in particular at higher t. This is the reason for the inconsistency in the values for the *rms* radii. All models predict smaller halo than the one deduced from the present experiment. This leads to smaller matter radius, respectively. In the case of ^{12}Be no definite

Model	R_m, fm	R_h, fm	R_c, fm	χ^2	Ref.
Elastic scattering	2.82(12)	5.41(32)	2.18(10)		this work
A	2.72	4.02	2.30	4.96	[25]
B1	2.59	3.51	2.30	5.13	[25]
B2	2.75	4.16	2.30	4.60	[25]
B3	2.70	3.94	2.30	4.83	[25]
B4	2.57	3.42	2.30	5.56	[25]
B5	2.62	3.63	2.30	5.23	[25]
FMD	2.56	–	–	6.09	[26, 78]

Table 5.6: Root mean square radii of ^{12}Be determined with different versions of the three-body calculation and χ^2 of the calculated with the corresponding density distribution cross section relative to the experimental one.

conclusion about the structure of the nucleus can be made based on the comparison of the theoretical calculation with the experimental data. Further calculations using the data as an input may give more information.

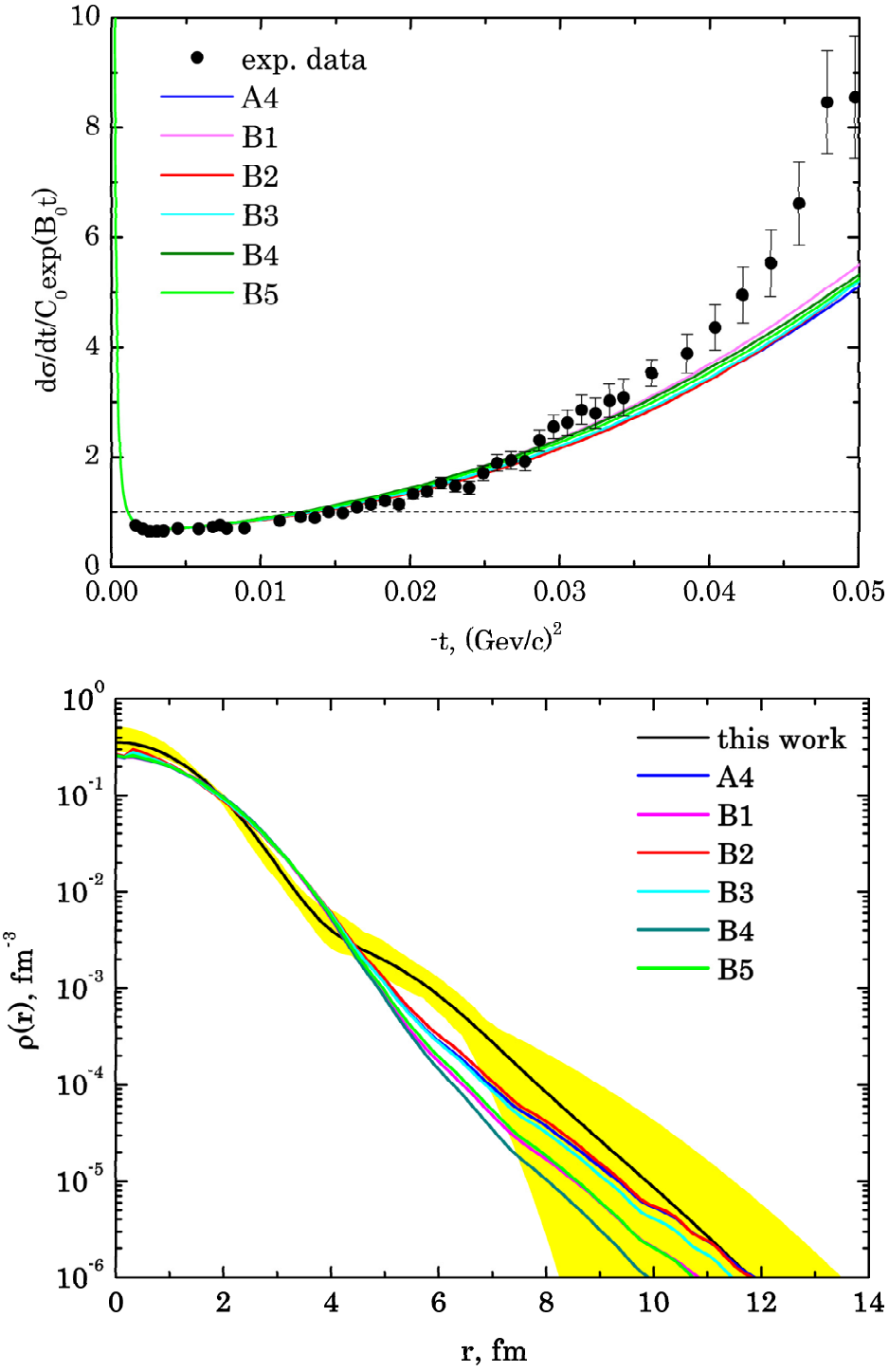

Figure 5.22: Differential cross section for p-^{12}Be elastic scattering calculated with a theoretical density distribution from few-body calculations compared to the experimental one (top). Few-body nuclear matter density distribution compared to the average matter distribution of ^{14}Be deduced from the present experiment (bottom).

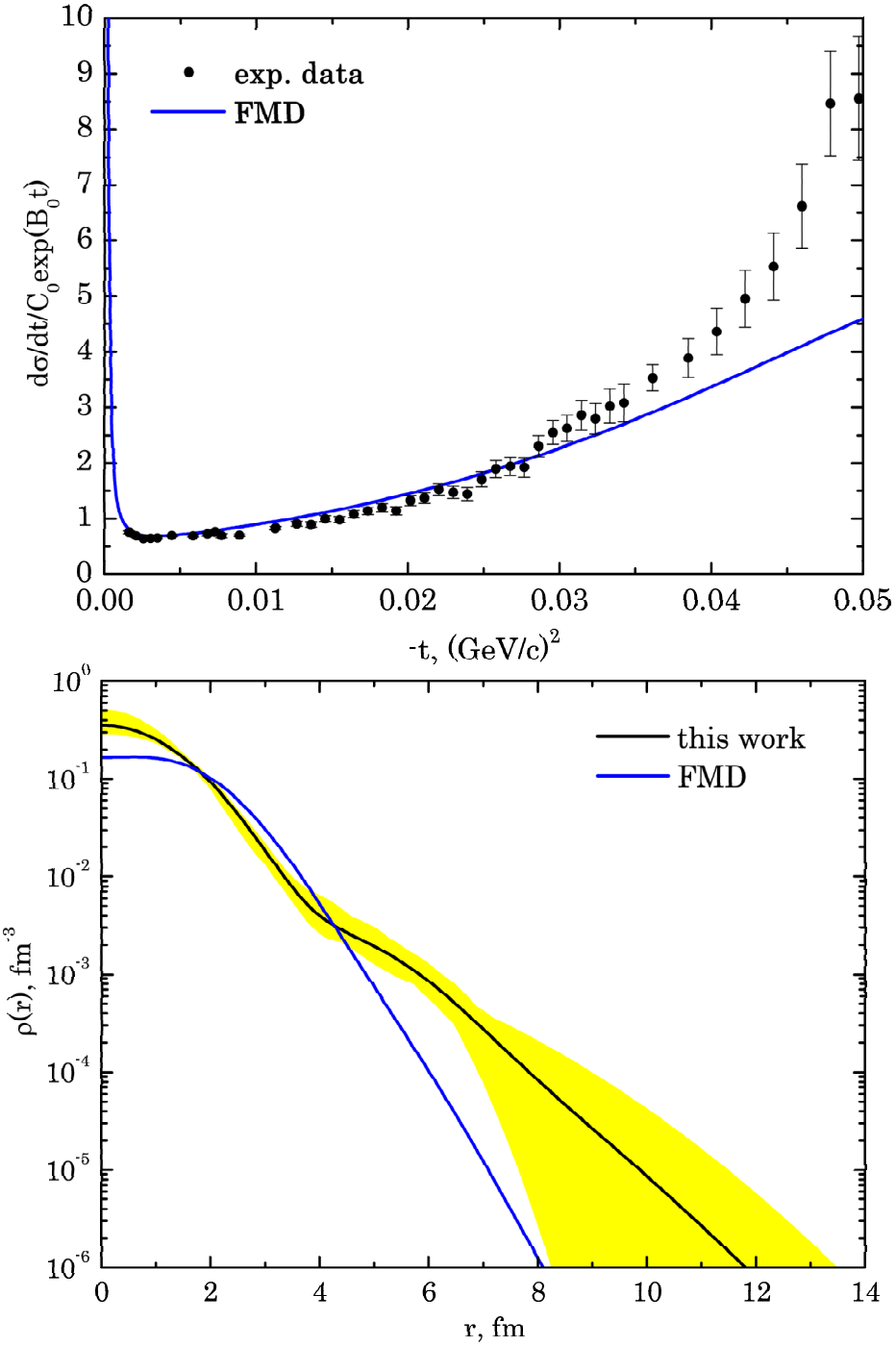

Figure 5.23: Differential cross section for p-^{12}Be elastic scattering calculated with a theoretical density distribution from FMD calculations compared to the experimental one (top). FMD nuclear matter density distribution compared to the average matter distribution of ^{14}Be deduced from the present experiment (bottom).

5.3 Preliminary results for ^{8}B

5.3.1 *Nuclear matter density distribution and matter radius of ^{8}B*

Preliminary analysis of the data for the nucleus ^{8}B was also performed. In contrast to the analysis of the data for the isotopes ^{12,14}Be, for ^{8}B the cross section was obtained only from information about the projectile scattering angle obtained from the MWPCs (see Eq. (3.5)). In this case the information from IKAR was not used in the selection procedure as the detector was not working properly and no signals from the B anodes were recorded during the ^{8}B run. For the case of ^{8}B this is not so crucial as the proton separation energy $S_p = 0.137$ keV is very small and practically no inelastic scattering is observed as there are no particle stable excited states in the nucleus. Thus, it is sufficient to separate the break-up events from the elastic scattering in order to obtain the preliminary cross section. As the recoil energy is determined with a bigger error from the MWPCs this leads to a bigger uncertainty in the measured cross section.

The preliminary experimental data were analyzed using the GG, GH and GO density parameterizations. The fit parameters of the analysis are given in Table 5.7. The deduced density distributions and the fitted cross sections are displayed in Figs. 5.24, 5.26 and 5.25 for the GG, GH and GO parameterizations, respectively. The average density distribution is shown in Fig. 5.28. Except for small values of the momentum transfer ($t \leq 0.01$ (GeV/c)^2) the cross section is described quite well but still a relatively bad χ^2 is obtained. The bad χ^2 also reflects the fact that a normalization coefficient much different than one is obtained.

Paramete-rization	R_m, fm	Fit parameters A_n	Density	parameters	χ^2/N
GG	2.57(5)	0.39(1)	$R_c = 2.35(1)$	$R_h = 3.78(29)$	369/47
GH	2.60(3)	0.39(1)	$R_m = 2.60(3)$	$\alpha = 0.08(2)$	362/47
GO	2.59(4)	0.39(1)	$R_c = 2.30(1)$	$R_h = 4.06(22)$	363/47

Table 5.7: Parameters obtained by fitting the experimental cross section for p-^{8}B elastic scattering using the density parameterizations GG, GO and GII. The presented parameters refer to point-nucleon density distributions. Only statistical errors are given. The parameters are as follows: R_m - root mean square matter radius; R_c - radius of the core ; R_h - halo radius; N - number of degrees of freedom; A_n - normalization of the calculated cross section. A_n and α are dimensionless, all other fit parameters are in fm.

The different density parameterizations give consistent results for the matter, core and halo radii within errors (Table 5.7). For ^{8}B a core radius of $2.33 \pm 0.01 \pm 0.23$ fm and a halo radius of $3.96 \pm 0.18 \pm 0.40$ fm were obtained. The core radius is consistent with the radius of the free ^{7}Be isotope which is $R_m = 2.31$ fm [19]. Due to the fact that the halo structure is composed of one proton, it is not so pronounced as in the case of the neutron halos and a smaller halo radius is observed. The behaviour of the cross section when divided by an exponential function though clearly shows the presence of the halo (see Fig. 5.27). The deduced weighted mean *rms* radius for

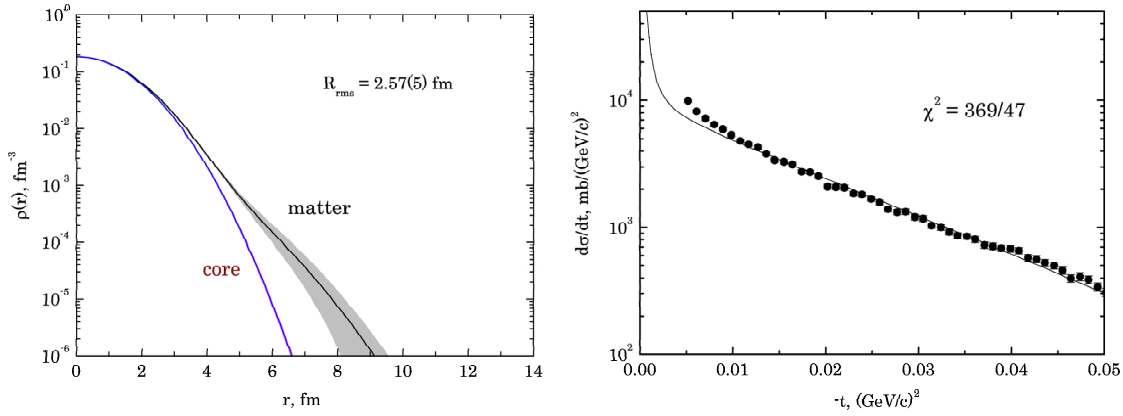

Figure 5.24: Results obtained with the Gauss-Gauss parameterization. Core and matter density distribution of ^{8}B (left); comparison between the experimental data and the fit with the GG parameterization (right).

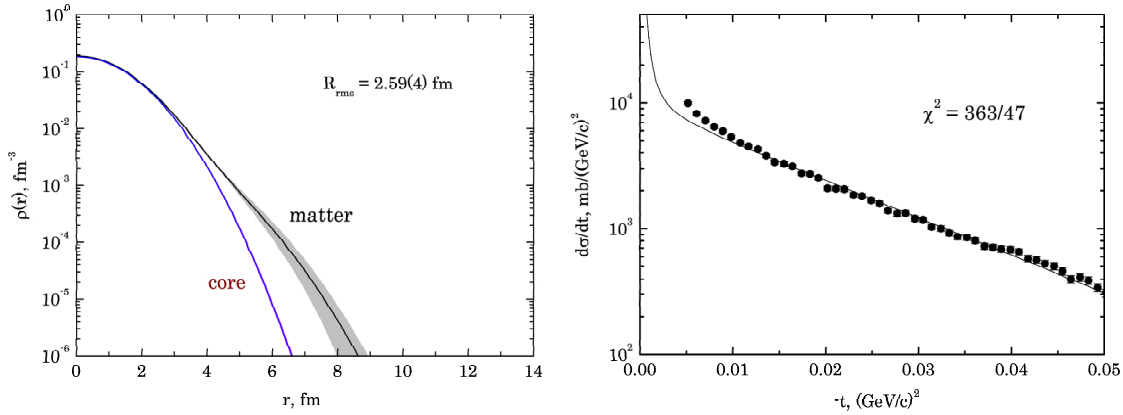

Figure 5.25: Results obtained with the Gauss-oscillator parameterization. Core and matter density distribution of ^{8}B (left); comparison between the experimental data and the fit with the GO parameterization (right).

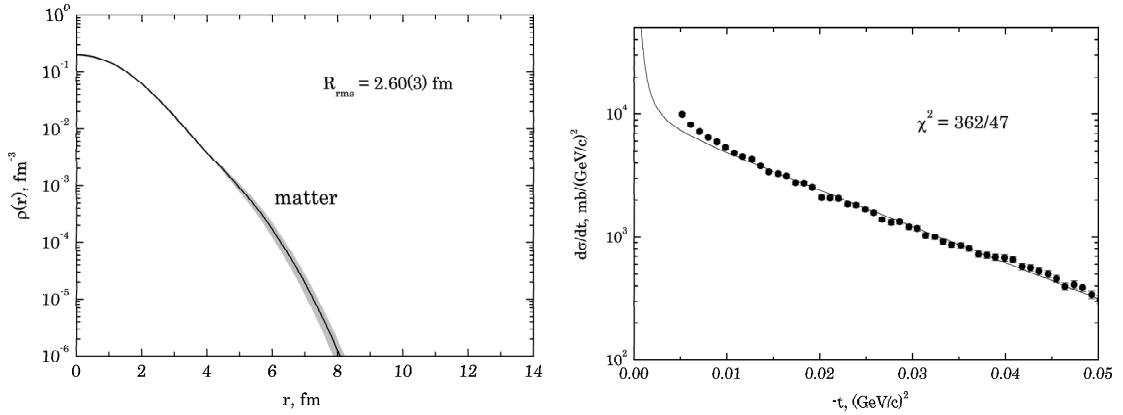

Figure 5.26: Results obtained with the Gauss-halo parameterization. Core and matter density distribution of ^{8}B (left); comparison between the experimental data and the fit with the GH parameterization (right).

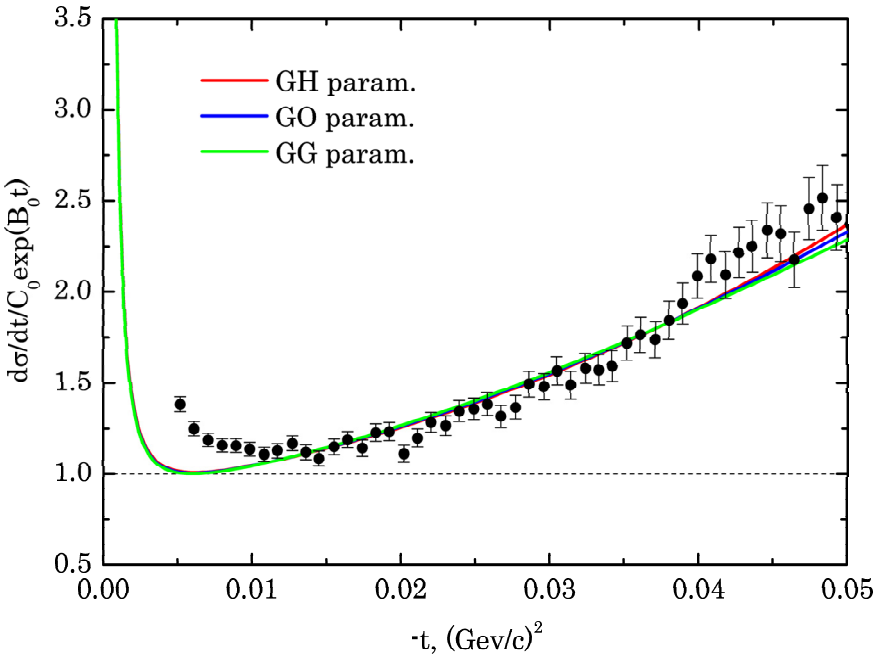

Figure 5.27: Experimental absolute differential cross section for proton elastic scattering on ^{8}B as a function of the four momentum transfer $-t$ (black points), compared with the fitted cross sections obtained on the basis of different phenomenological density parameterizations (lines). All data are divided by exponential function to better visualize the halo structure.

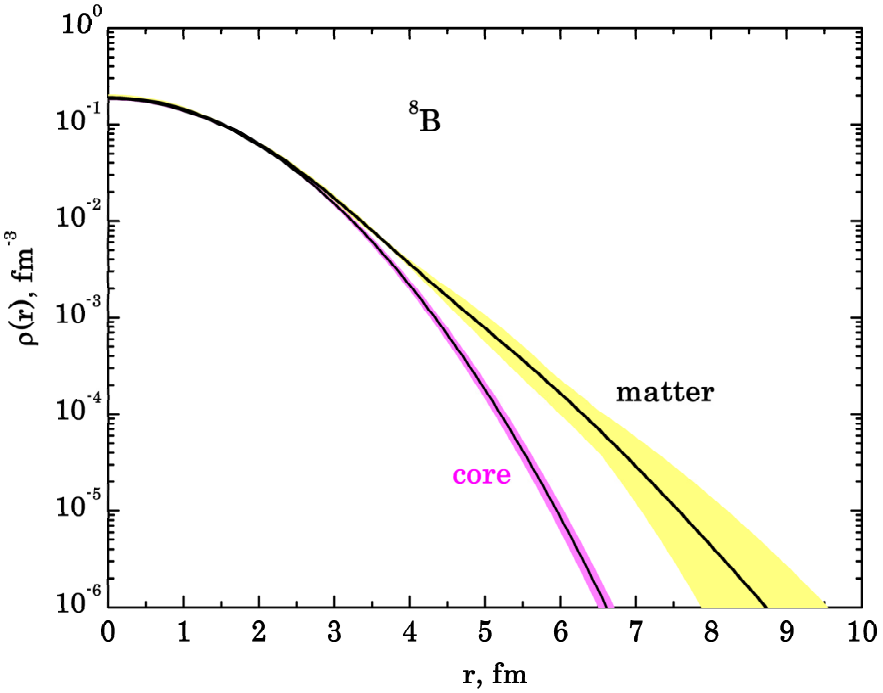

Figure 5.28: Average matter density distribution of ^{8}B. For the average the densities obtained with the GG, GO and GH parameterizations were used and the error-band was created as the sum of all the individual error-bands.

^{8}B is $R_m = 2.60 \pm 0.02 \pm 0.26$ fm and was obtained using the results from the three density parameterizations GG, GO and GH. The average matter density distribution is shown in Fig. 5.28 and the small halo tail can be seen. The error in the density is constructed as the sum of the errors from all the densities.

The preliminary analysis of the data for the p-^{8}B elastic scattering gives strong evidence for the presence of a proton halo. Such structure is for the first time investigated with the present experimental method.

5.3.2 *Comparison with other experimental results and with microscopic theoretical calculations*

The previous experimental and theoretical studies of the structure of ^{8}B show controversial results for its matter radius (see Table 5.8). Radii in the range from 2.38 fm up to 2.60 fm were determined. The analysis of experiments on interaction cross section measurements gives systematically smaller values for the matter radius than the one obtained in this work. The present experiment is consistent with the results obtained from momentum distribution investigations and also with several theoretical calculations.

		R_m, fm	Ref.
Experimental method	Analysis model		
Elastic scattering	–	2.60(26)	this work
Interaction cross section	Glauber theory	2.38-2.39	[19]
Interaction cross section	Glauber theory	2.43-2.44	[37]
Interaction cross section	few-body model	2.50(4)	[80]
Momentum distribution	microscopic model	2.58-2.60	[39]
Theoretical model			
Dynamical microscopic cluster model		2.57	[81]
ANC		2.60(4)	[82]
FMD		2.53	[78]

Table 5.8: Comparison of the results for the nucleus ^{8}B with previous experimental studies and theoretical calculations. List is not comprehensive, more studies exist. (ANC - asymptotic normalization coefficient)

The experimental cross section was compared with a cross section calculated using density from FMD model calculations with a radius of $R_m = 2.53$ fm. In Fig. 5.29 the comparison between the experimental data and the FMD calculation is shown. The quality of the description with this model is quite reasonable and from the comparison of the experimental and calculated cross sections $\chi^2 = 7.69$ is obtained. There is a very good agreement between the theoretical density and the one deduced in the present experiment (Fig. 5.29(bottom)).

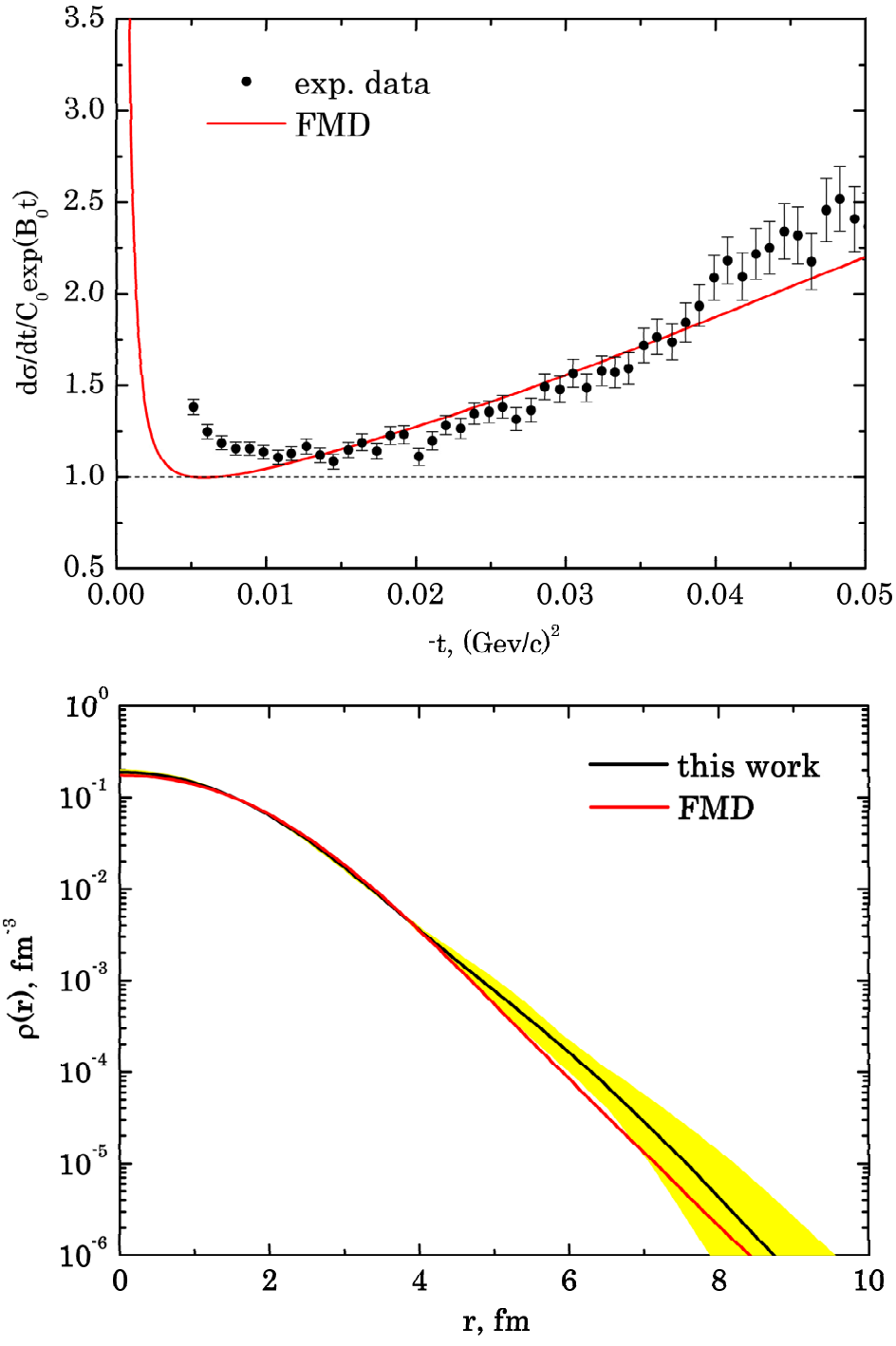

Figure 5.29: Comparison between the experimental data and the cross section calculated using a theoretical density from an FMD calculation. The cross sections are plotted on top, comparison between densities is plotted at the bottom.

CHAPTER 6

Feasibility studies of the EXL setup for FAIR

6.1 The EXL project at the future FAIR facility

At GSI a future international facility FAIR (Facility for Antiproton and Ion Research) [41, 42] is planned where the main interest are experiments with radioactive beams and experiments at storage rings. The FAIR facility has the advantage of providing beams with intensity up to four orders of magnitude higher than the presently available at GSI. The radioactive beams will be produced at the Super FRS [83] which is a system analogical to the present FRS at GSI (Fig. 6.1). The secondary beam afterwards can be used in direct experiments or in storage ring experiments. Within the EXL project (EXotic nuclei studied in Light-ion induced reactions at the NESR storage ring) [42, 43] for FAIR which is part of the NUSTAR (NUclear STructure, Astrophysics and Reactions) program [44], a universal detector system is proposed for the investigation of light-ion induced reactions.

In the frame of the EXL project, it is foreseen to install a universal detection system providing high resolution (due to the beam cooling) and large solid angle coverage at the internal target of the NESR storage cooler ring where very high luminosities (due to the beam recirculation) can be reached (Fig 6.2). This will allow the investigation of all kinds of reactions for nuclei with a lifetime long enough to survive the cooling time in the storage ring (of the order of 1 s). The use of a windowless internal target creates favourable conditions for high resolution measurements at very low momentum transfer where important information about the nuclear structure is contained (an advantage as compared to direct experiments like for example in the R^3B [42] project where due to the thicker target the low momentum transfer information will be lost).

Due to the very low production rate of exotic nuclei there is a limited possibility to study them. The storage ring experiments have advantage with respect to this be-

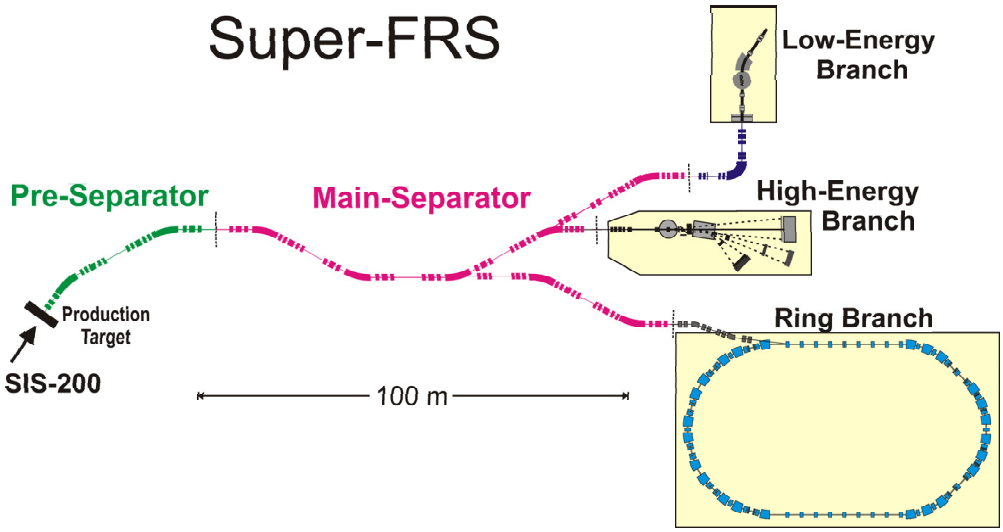

Figure 6.1: Super FRS and experimental areas at FAIR. The high-intensity radioactive beams are available for low and high energy direct experiments and for experiments at storage rings with cooled beams. The EXL project belongs to the ring branch.

cause of the higher luminosity reachable there. The accumulation and recirculation of the beam in the ring with a typical frequency of several MHz and the fact that there are no windows around the target, which reduces the matter with which the beam interacts, makes it possible to reach a luminosity several orders of magnitude higher than in a regular beam line experiment.

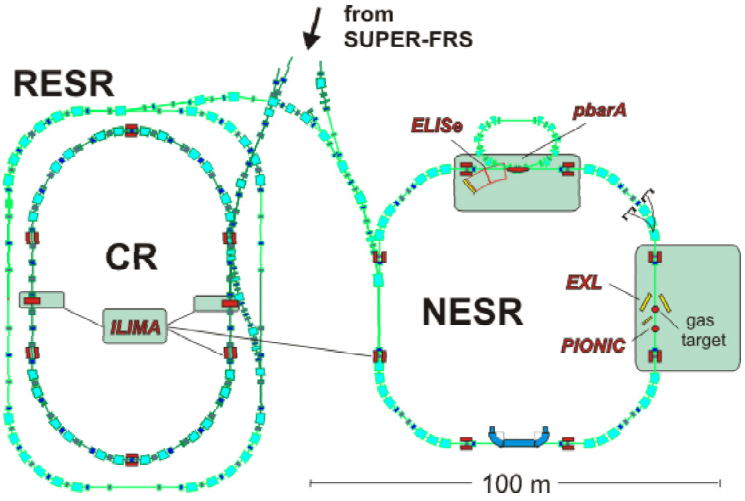

Figure 6.2: Ring branch at the FAIR facilities. High-intensity radioactive beams are supplied by the Super FRS. High precision and luminosity experiments are planned.

The key nuclear structure physics and astrophysics issues to be studied by the EXL setup are described in [43, 45]. The main topics concerning exotic nuclei to be addressed are as follows:

- Studies of the unusual matter distributions by using light-ion elastic scattering

in inverse kinematics, which gives access to the nuclear size and radial shape, and also to higher moments of the density distribution.

- Investigation of electric and magnetic giant resonances and other exotic collective modes due to different proton and neutron deformations. Thus, important information about the nuclear equation of state and a better understanding of the effective nucleon-nucleon interaction can be obtained.

- Studies of the nucleon-nucleon interaction and the spin and isospin effects on it can be made using charge-exchange reactions. Studies of the Gamow-Teller transitions give information about the weak interaction rates which are important for the nucleosynthesis.

- Investigation of the single-particle proton and neutron structure of neutron- and proton-rich nuclei by transfer reactions which gives getting insight in the evolution of the shell structure towards the drip-lines and finding spectroscopic information important for the astrophysical r- and rp-processes.

The information provided through such experiments is an important basis for tests of many nuclear structure and astrophysical theories.

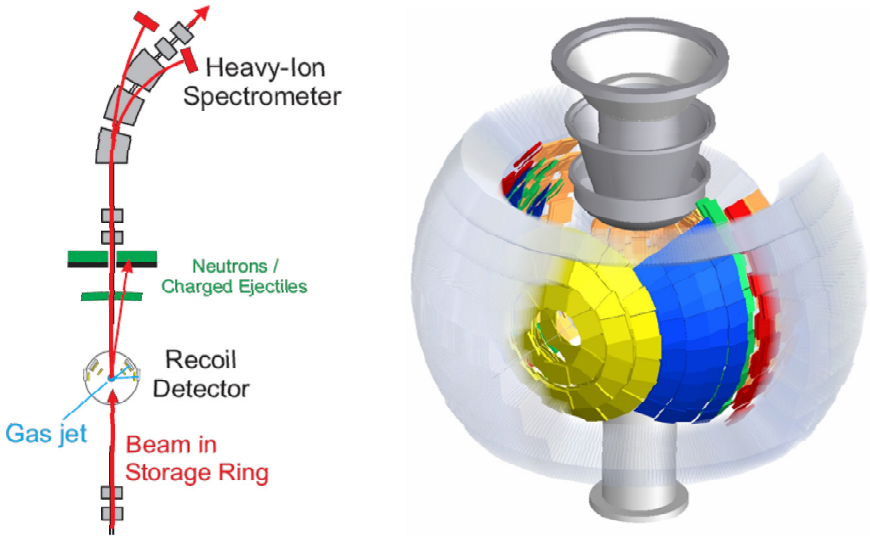

Figure 6.3: Detector setup planned to be installed at the NESR at FAIR in the frame of the EXL project. The setup foreseen consists of a large solid angle recoil detector system around the internal gas-jet target, a forward scintillator spectrometer for neutrons and light charged ejectiles placed downstream from the target and a heavy-ion spectrometer for identification of beam-like particles placed after the first dipole magnet of the storage ring.

The EXL detector system (Fig. 6.3) includes an array of double-sided Si strip detectors for recoil target-like reaction products for position and energy loss measurements, completed by Si(Li) detectors for total energy measurement of stopped particles. It will be surrounded by detectors for γ-rays and slow neutrons. Further downstream there will be scintillator detectors for fast ejectiles (neutrons and light charged particles). In forward direction, after the dipole magnet of the storage ring

there will be an in-ring spectrometer for the detection of beam-like reaction products. This detector system will allow for a full reconstruction of the kinematics of the reaction.

6.2 Feasibility studies of the EXL setup

6.2.1 *Experimental setup for the test experiment*

Within the frame of the present thesis a first test experiment for checking the feasibility of the EXL detector setup was performed at the Experimental Storage Ring ESR in GSI, Darmstadt [84]. The stable ^{136}Xe beam with an energy of 350 MeV/u was interacting with the internal hydrogen gas-jet target. Detectors representing all the major detector systems of EXL were installed (Fig. 6.4).

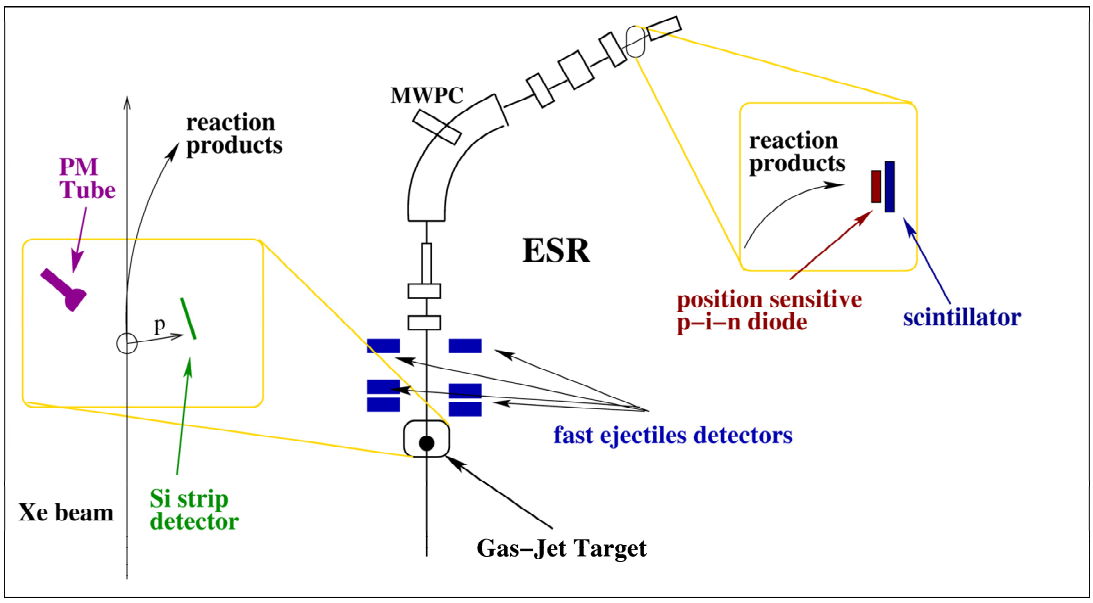

Figure 6.4: Experimental setup for the EXL test experiment performed at the present storage ring ESR at GSI. Around the gas-jet target a Si strip detector for the low momentum transfer recoil protons and a photomultiplier tube for monitoring the luminosity were installed. Further downstream a set of scintillator detectors with iron converters was placed for detection of fast light ejectiles. At the first dipole magnet a MWPC was placed to detect heavy-ions which have undergone atomic charge exchange. At the end of the setup, after the dipole, a position sensitive p-i-n diode and a scintillator, used for beam identification, were installed.

An UHV[1] compatible single-sided Si strip detector was mounted in the vacuum chamber around the internal gas-jet target to detect the recoil protons (Fig. 6.5). The detector was mounted on a special vacuum compatible ceramic support and the read-out was completed with custom made copper wires with glass pearls shielding. The high vacuum in the storage ring requires any equipment placed inside to be resistant to high temperatures. The Si strip detector was tested and it was shown

[1]UHV - Ultra High Vacuum

that it can withstand temperatures up to 200° [85]. The detector consists of 40 strips with a thickness of 1 mm and a width of 1 mm with a total area of 40×40 mm^2. The strips were read-out in groups of 8 using a charge division method (Fig. 6.5). The detector was first tested off-line with an Am α-source and an energy resolution of 25 keV at 5 MeV (0.5%) was obtained (Fig. 6.6(A)). The detector also showed a very good position resolution (Fig. 6.6(B)). To protect the detector from the light coming from the hydrogen target a thin Ni foil (1 μm) was mounted in front of it. The detector was mounted at 90° laboratory angle where the low momentum transfer recoil particles are to be detected and covers a solid angle of 0.077 sr.

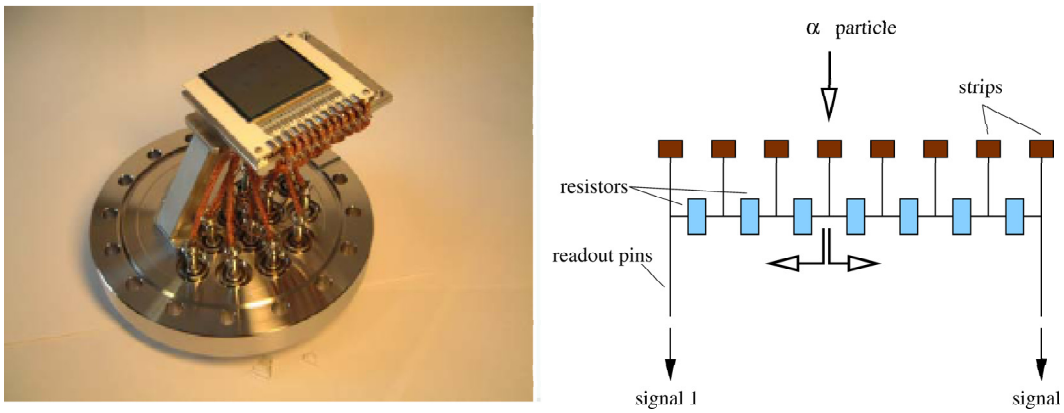

Figure 6.5: Photo of the Si strip detector used in the EXL test experiment, together with the mounting flanch and the wiring (left). Charge division read-out for the Si strip detector (right). The sum of signal 1 and signal 2 gives the energy deposited in the detector, and their ratio gives information about the coordinate of the particle.

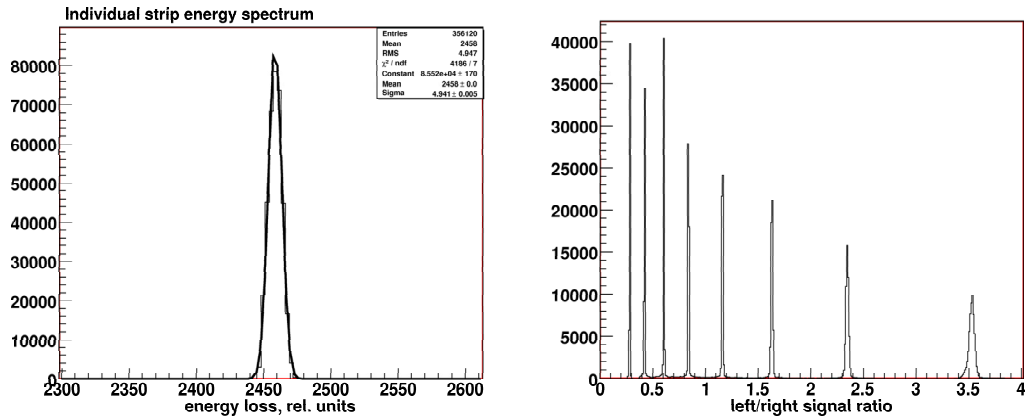

(A) (B)

Figure 6.6: (A) Energy resolution of individual strip of the Si strip detector. (B) Position resolution of one group of the Si strip detector. The individual strips are clearly separated.

Two walls of organic scintillators (Fast Ejectile Detectors Fig. 6.4) with iron converters have been installed at distances of 2.5 m and 4 m downstream after the

target. The scintillators are 50 cm long, 10 cm wide and have a thickness of 5 cm. The iron converters have a thickness of 5 cm. They were used to detect the fast ejectiles (i.e. neutrons and light charged particles).

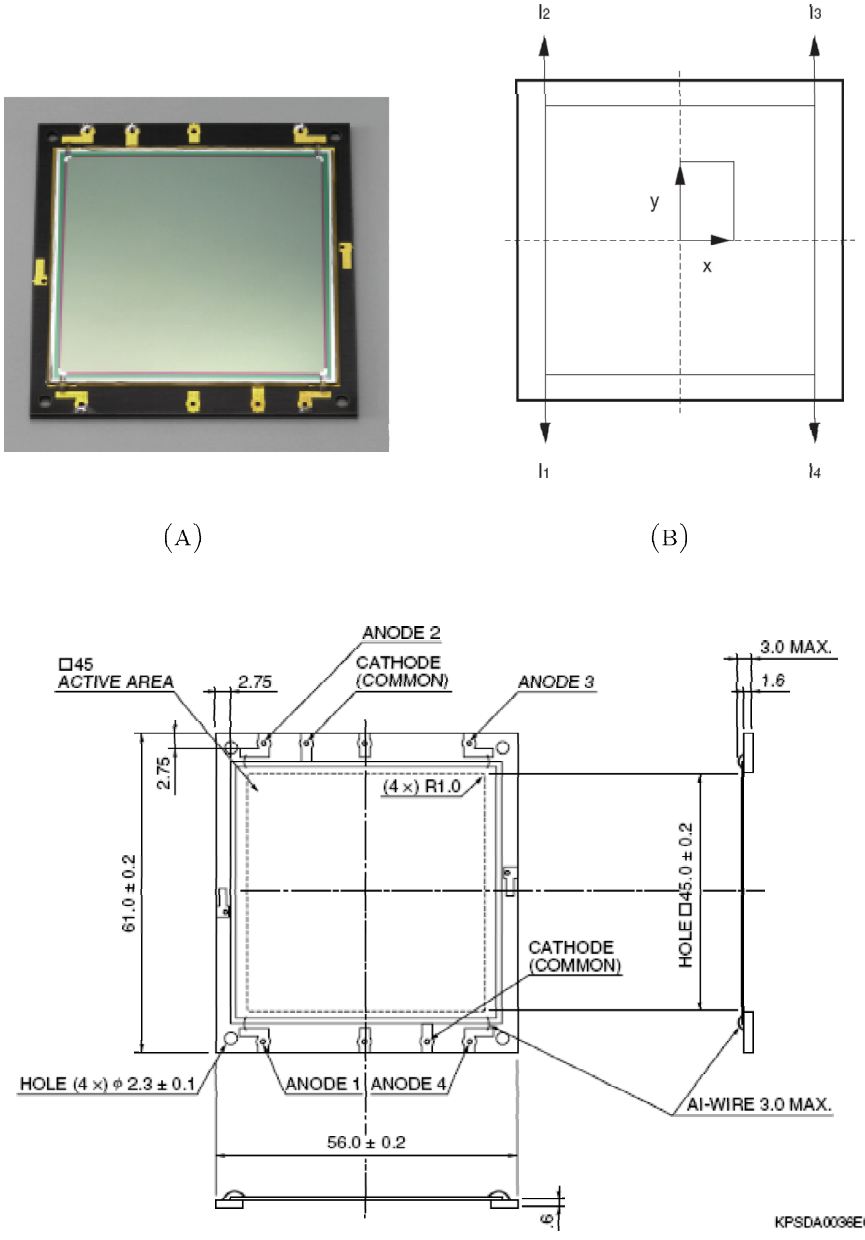

Figure 6.7: (A) Photo of the p-i-n diode used for projectile identification in the EXL test experiment. (B) Scheme for the coordinate determination (see Eq. 6.1 and text for details). (C) Electrodes scheme of the detector. The signals from the four cathodes were used to determine the coordinate of the particles while the signal from the back anode gave the energy loss of the projectiles.

A 1 mm thick scintillator and a position sensitive p-i-n silicon diode (Fig. 6.7(A), (C)) with a thickness of 300 μm were installed after the first dipole magnet of the

ESR in a movable vacuum pocket driven in and out of the beam tube. These detectors were used for identification and fast timing of the beam-like heavy ions. The active area of the p-i-n diode was 45×45 cm^2. The energy signal of the p-i-n diode was read-out from the back anode of the detector and the signals from the four corners of the cathode were used to determine the coordinates of the heavy ion (Fig. 6.7(B) and Eq. 6.1).

$$x = \frac{L}{2}\left(\frac{(l_3 + l_4) - (l_1 + l_2)}{l_1 + l_2 + l_3 + l_4}\right.$$
$$y = \frac{L}{2}\left(\frac{(l_2 + l_3) - (l_1 + l_4)}{l_1 + l_2 + l_3 + l_4}\right. \qquad (6.1)$$

A multi-wire proportional chamber (MWPC) was used as a luminosity monitor, detecting ^{136}Xe ions deflected out of central orbit due to atomic charge-exchange reactions. The luminosity has been also measured with a photomultiplier installed near the target, detecting light produced by the interaction of the heavy ions with the hydrogen atoms. The Si strip detector served as a third luminosity monitor.

The electronics scheme for this setup is shown in Fig. 6.8. The trigger for the read-out of the detectors was obtained by a logical OR from the signals from the Si strip, fast ejectile and scintillator detectors.

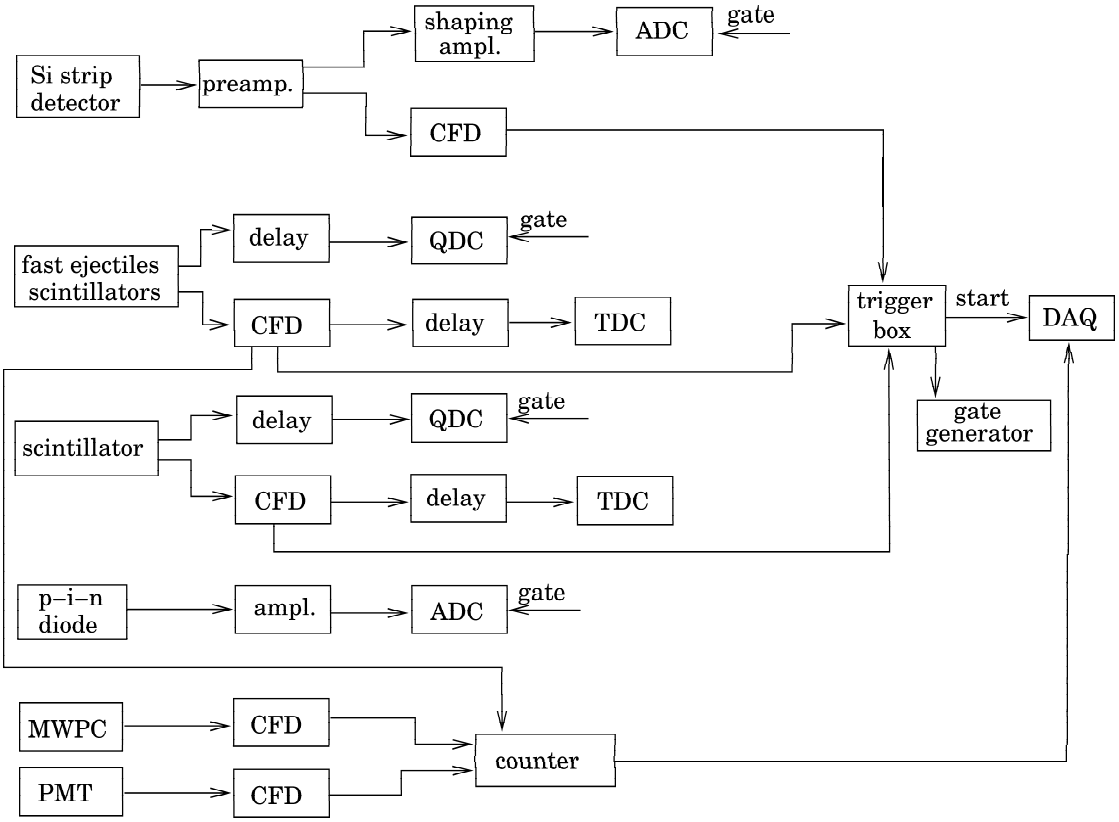

Figure 6.8: Electronics scheme for the EXL test experiment. (CFD - constant fraction discriminator; ADC - amplitude to digital converter; QDC - charge to digital converter; preamp. - preamplifier; TDC - time to digital converter)

6.2.2 *Data analysis and results*

During the test experiment the beam was scanned over the internal gas-jet target in order to obtain the target profile and check the consistency of all the luminosity monitors. The target profiles obtained with different detectors are plotted in Fig. 6.9. They are consistent with each other and give the profile of the overlap between the target and the beam. The size of the jet target after defolding the beam size (estimated to be 5 mm) was determined to be 7.0±0.2 mm (FWHM). The absolute luminosity has been deduced with the help of a current transformer measuring the beam intensity and by knowing the target density (which was constantly measured during the experiment), and reached the value $(6\pm2)\times10^{27}$ cm^{-2}s^{-1}. This luminosity is two orders of magnitude higher than the one typical for the IKAR experiments where the usual value is $(8 \pm 2) \times 10^{25}$ cm^{-2}s^{-1}.

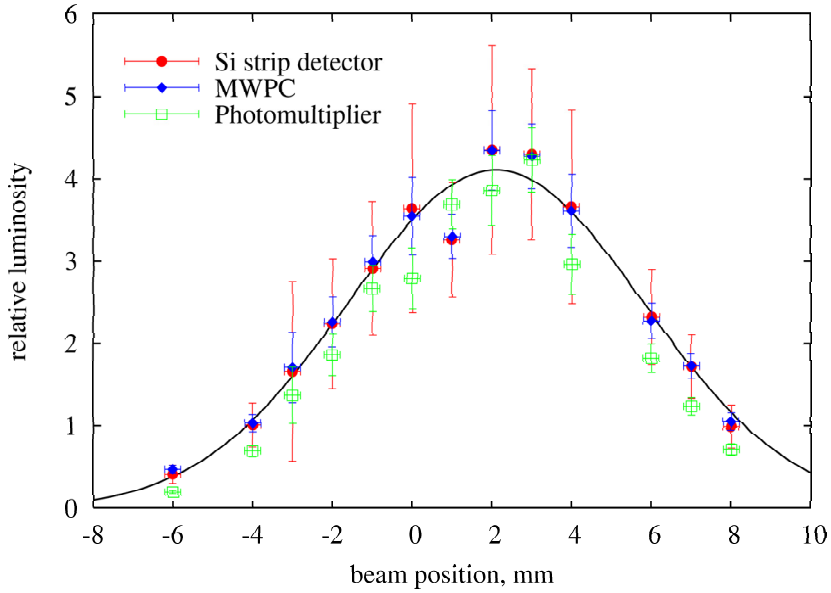

Figure 6.9: Target profile of the hydrogen gas-jet target installed at the ESR. The position of the beam was changed at the target position and the resulting change in event rate was observed with several detectors installed at different places of the setup. The determined target size was 7.0±0.2 mm FWHM.

For the analysis of the differential cross section for elastic scattering the data from the first group of the Si strip detector (the 8 strips placed closest to 90°, which corresponds to 0° c.m. angle) were taken. In the first group of the Si strip detector almost only elastic scattering events are detected as the cross section for the inelastic scattering is negligibly small at these angles [86]. To obtain the cross section the energy of the protons was corrected for their energy loss in the Ni foil placed in front of the detector and additionally, each data point was corrected for the effective solid angle. This correction is necessary due to the extended target. The correction was obtained from Monte Carlo simulations performed in KVI, Groningen [87, 88, 89]. In Fig. 6.10 the experimental data are compared with the simulation of the detector response for an extended target with FWHM equal to 8.5 mm and with the theoretical calculation of the elastic scattering cross section. This target size was chosen as it gives the best description of the experimental data. The inconsistency

with the measured target size comes from possible not correct estimation of the beam size. The experimental data points corrected for the target geometry are also shown. This correction is very important as due to the extended target the detector

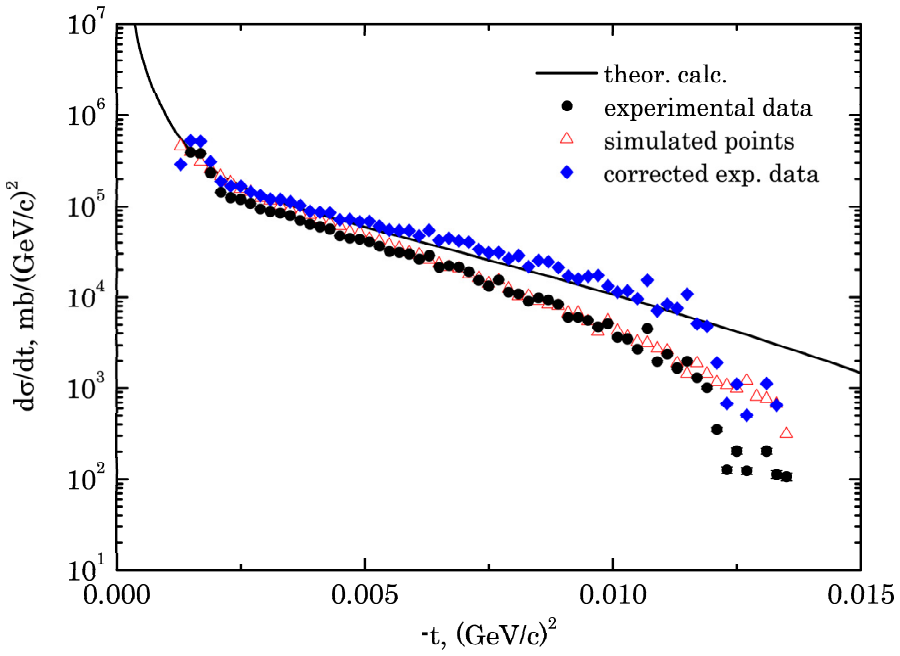

Figure 6.10: The differential cross section for p^{136}Xe elastic scattering (solid line) calculated with the Glauber theory is compared with the experimental data (full circles) from the first group of the Si strip detector and with a Monte Carlo simulation. The triangles correspond to a simulation of the detector response for a not point-like target (FWHM=8.5 mm) and the full diamonds are the experimental data corrected for the extended target effect according to the simulation.

covers different solid angle for different momentum transfer values t. The obtained differential cross section was analyzed within the Glauber multiple-scattering theory (see Chapter 4). The results are shown in Fig. 6.11. From the analysis with the symmetrized Fermi parameterization a matter radius $R_{rms} = 4.85 \pm 0.1$ fm was determined. The parameters of the symmetrized Fermi function are $R = 4.54 \pm 0.05$ fm and $a = 0.90 \pm 0.05$ fm. For a comparison the charge radius determined for ^{136}Xe is 4.8 fm [90]. Note that in order to compare both values the charge radius has to be defolded from the proton radius which leads to the value 4.76 fm.

The inelastic scattering for the excitation of the giant dipole resonance (GDR) in ^{136}Xe was also observed (The calculations were performed for the excitation energy of the GDR E_{ex}=15 MeV, taken from Ref. [91].). According to the simulation for the kinematics of the elastic and inelastic scattering events plotted in Fig. 6.12 and the calculated cross sections, in the fifth group of the Si strip detector the most inelastic events will be detected and the contribution of the elastic scattering there is the smallest. In Fig. 6.13 the experimental data, taken from the fifth group of the

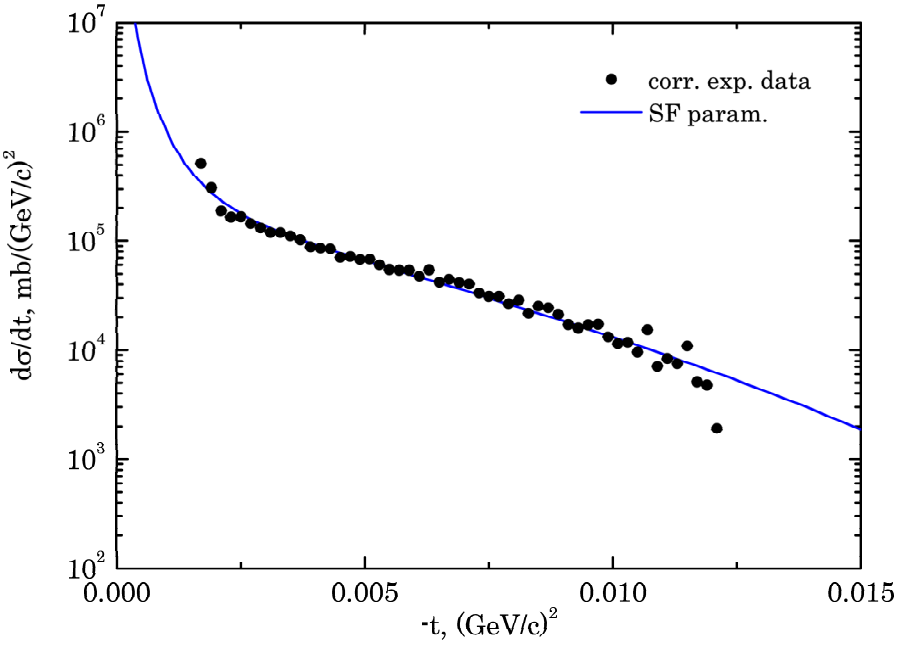

Figure 6.11: Measured differential cross section for p-^{136}Xe elastic scattering. The data points correspond to the experimental data corrected for the extended target size. The cross section was analyzed within the Glauber theory using the symmetrized Fermi parameterization.

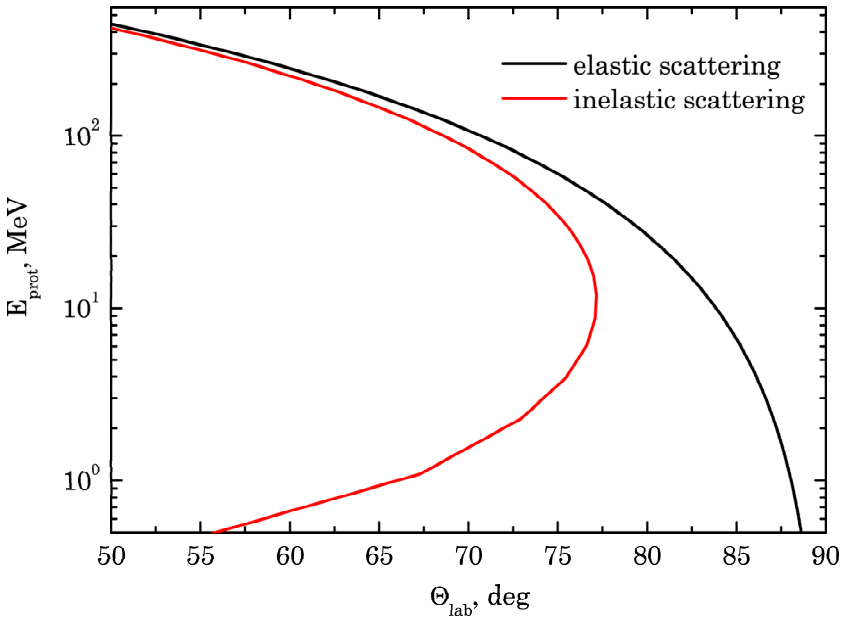

Figure 6.12: Kinematics of the proton scattering on ^{136}Xe nuclei. The energy of ^{136}Xe is 350 MeV/u. The inelastic scattering (red line) is calculated with an assumed excitation energy for the GDR E_{ex}=15 MeV.

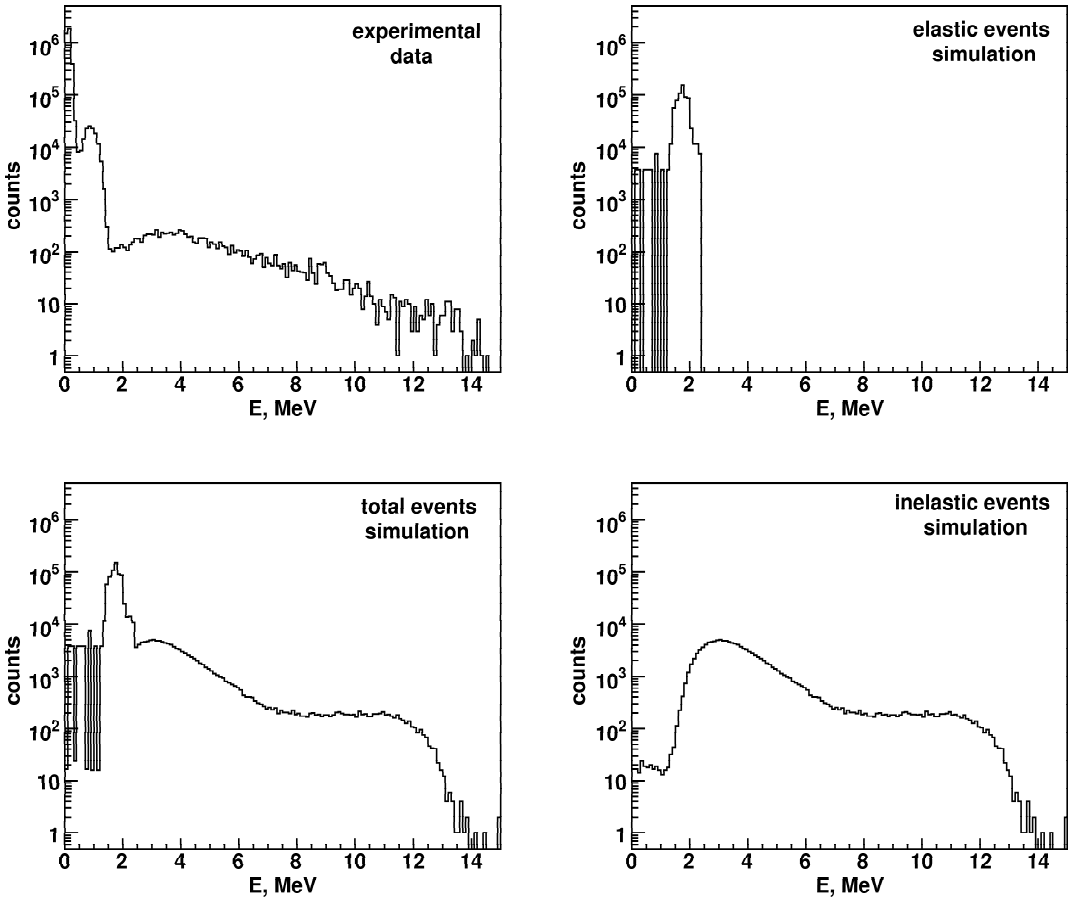

Figure 6.13: Comparison between the experimental data and simulation for the response of the fifth group of the Si strip detector. In the simulation both elastic and inelastic scattering are included. Left side: Total spectra from the experiment (top) and the simulation (bottom). Right side: Simulation of elastic scattering events only (top) and of inelastic scattering events only (bottom).

Si strip detector which is located around 75° in the laboratory system, are compared with the simulation. In the simulation both elastic and inelastic events are included and very good agreement between simulation and experiment is observed.

Other reaction channels, like (p,n), (p,pxn), (p,2pxn) could also be identified using correlations between the detectors for fast ejectiles and the detectors for beam-like heavy ions. The scintillator was used only for triggering as its energy resolution did not allow isotope separation. For this the p-i-n diode, which has better resolution, was used. The result of such a coincidence measurement is shown in Fig. 6.14. The cleaning of the energy spectrum of the p-i-n diode is due to a condition that a light reaction product was detected in the forward scintillators. An example of proton identification is shown in Fig. 6.15. These spectra were obtained with a selection of the iodine isotopes in the p-i-n diode and coincidence conditions in the fast ejectile detectors.

The results from this first test measurements show that investigations of different nuclear reactions at storage rings with cooled beams and gas-jet target are feasible.

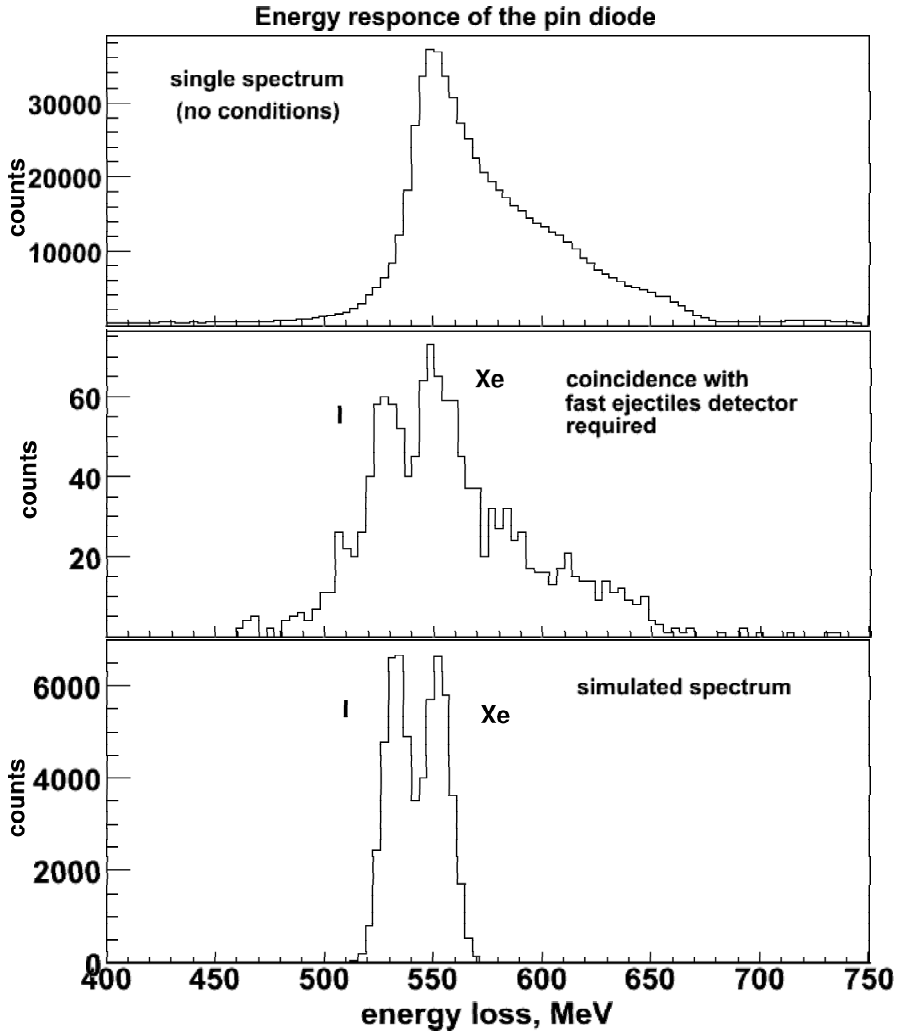

Figure 6.14: Reaction channel selection. The top plot shows the raw energy spectrum of the p-i-n diode without any condition applied. The middle plot is the same spectrum with a condition for a coincidence with a fast proton or neutron hitting the forward angle scintillator detectors. The bottom plot shows a simulation of the p-i-n diode response for a ^{136}Xe(p,pxn)$^{136-x}$Xe and ^{136}Xe(p,2pxn)$^{135-x}$I channels. The left peak corresponds to I isotopes and the right one to Xe.

It is possible to make low background measurements with UHV compatible detectors close to the beam orbit. Separation of different reaction channels is possible as well, when auxiliary detectors are used. The feasibility of the detector setup for the EXL project for FAIR was confirmed.

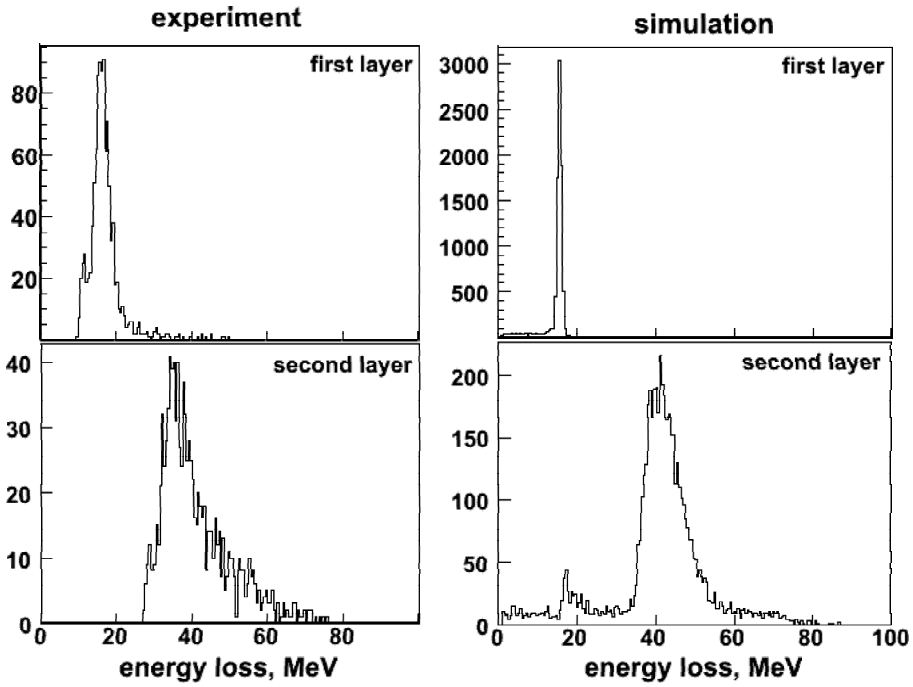

Figure 6.15: Proton signals in the first two layers of the fast ejectiles scintillator detectors are displayed. On the left side the experimental spectra are shown. On the right side the simulation of the signals from 350 MeV protons in the same detectors are plotted for comparison.

Conclusions and future perspectives

The differential cross section for intermediate energy proton elastic scattering provides detailed information about the size and spatial extent of the nuclear matter. The data at low momentum transfer reflect mainly the outer structure of the nucleus thus, the proton elastic scattering is a very good tool for investigating halo nuclei where the most interesting part is the low density surface formed by the halo.

The active target ionization chamber IKAR is designed especially for measurements of recoil protons in proton-hadron collisions at low momentum transfer. It gives high resolution information about the energy and scattering angle of the recoil proton in a 4π measurement.

An experiment on proton elastic scattering on ^{7,9,10,11,12,14}Be and ^{8}B in inverse kinematics was performed at GSI with main part of the experimental setup being the IKAR ionization chamber which served simultaneously as a proton target and a detector for the recoil protons. In addition, there were a number of auxiliary detectors used for particle identification and projectile tracking. The experiment was performed with improved conditions as compared to the previous measurements on the neutron-rich He [8] and Li [11] isotopes. The experimental setup was moved to Cave C where better transmission of the secondary beam from the fragment separator FRS is available, and in addition improved MWPCs with better resolution were used.

The result from the experiment are the differential cross section for proton-nucleus elastic scattering as a function of the four-momentum transfer at small scattering angles. They were analyzed within the Glauber multiple-scattering theory which describes very well the scattering process at intermediate and high energies. This theory connects in a straightforward way the nuclear matter density distribution and the scattering amplitude. The Glauber analysis is proven to work very well for stable nuclei and the theory was already successfully applied for the investigation of the neutron-rich He and Li isotopes. For the analysis, various density parameterizations were used to calculate the differential cross sections and their parameters

were fitted to the experimental data. For the first time the SOG method was applied for the analysis of small-angle proton elastic scattering data.

In this thesis, the results from the analysis of the cross sections for p-^{12}Be, p-^{14}Be and p-^{8}B are presented. The matter radii determined in this analysis with high accuracy are in most cases consistent with the previous measurements with other experimental methods and the values determined with the different density parameterizations are consistent with each other within the uncertainties.

The results from the analysis show evidence for an extended nuclear matter distribution of the nucleus ^{12}Be, and confirm the Borromean halo structure of ^{14}Be. The extended matter distribution of ^{12}Be is explained as due to intruder orbitals from the *sd* shell. The very large nuclear deformation of the isotope results in a change in the shell gap. The last neutrons of ^{12}Be can occupy an *s* orbital and as a result their wave function extends out of the nuclear potential which leads to the appearance of a low density tail in the matter distribution. ^{12}Be is not a Borromean halo nucleus as the core ^{10}Be is stable. The halo structure of ^{14}Be is of no doubt because evidence has been observed in previous experiments and is expected as both factors for the presence of a halo (low binding energy and low orbital momentum of the last nucleons) exist. Unfortunately, the present analysis is not sensitive to the number of halo particles and both two-neutron halo and four-neutron halo give equally good description of the experimental data. The results from this analysis show that the free ^{12}Be nucleus has different structure as compared to the core of ^{14}Be when assumed that the core consists of 12 nucleons.

The obtained high precision experimental data and density distributions can be used as a sensitive test and as an input for different theoretical studies. In this work a comparison was made with several existing model density calculations. For this purpose the experimental cross sections were compared with calculated ones using theoretical densities as an input for the calculation. Densities calculated within the Fermionic molecular dynamics model and the few-body model were used. These models study the clusterization effects and the correlations between the particles in the nuclei. In the case of ^{14}Be relatively good agreement with the data is observed while for the case of ^{12}Be the calculations do not describe the measured differential cross section well in the whole momentum transfer range. Further studies should be performed to investigate the reasons for this disagreement in the case of the ^{12}Be nucleus. For ^{14}Be the comparison with theory showed a possible high occupancy of the *s* orbital even though the shell model predicts that the last two neutrons should be on a *d* orbital.

Preliminary data for the ^{8}B isotopes were also analyzed. The analysis shows the existence of proton halo in ^{8}B, and this study is the first observation of a proton halo with the proton elastic scattering method. The obtained density distribution was compared with FMD calculations and very good agreement is observed. The halo structure of this isotope may be important for the nuclear astrophysics. It is expected that the size and shape of the proton halo, in case it exists, will strongly affect the S_{17} factor of the proton capture reaction ^{7}Be(p,γ)^{8}B [92]. This reaction is considered as one of the most important astrophysical reactions as its low-energy cross section determines the solar neutrino flux [93] coming from ^{8}B and the cross section for it is important for the branching ratios of the pp-chain reactions. At solar energies the reaction is highly peripheral which means that only the external

part of the bound and scattering wave functions contribute to the radiative capture cross section. Thus, the behaviour of the low-density tail of the matter of ^{8}B is very important for the study of this problem.

Data for the compact isotopes ^{9}Be and ^{10}Be were also measured in the present experiment but the analysis of these data is still not completed due to problems in the IKAR detector during this measurements. As these isotopes have a number of particle stable excited states separation of the elastic and inelastic scattering channels is not possible without information from IKAR.

The future usage of the present IKAR setup for further studies is limited. With it, it is possible to investigate isotopes up to carbon. Heavier projectiles have very high multiple Coulomb scattering through the setup and produce big signal in the IKAR detector, hence it is not possible to measure the scattering angles and the recoil energy with the necessary accuracy in the region of low momentum transfer. A proposal has been accepted for an experiment to measure the differential cross sections for proton elastic scattering on the neutron-rich carbon isotopes and this would be the last IKAR experiment.

For the investigation of heavier neutron- and proton-rich isotopes far off stability a new universal detector system EXL is being designed. It should be installed at the NESR at the future accelerator facility FAIR and can be used to study all kinds of reactions. Due to the usage of storage ring techniques high resolution and high luminosity can be achieved. Thus, the system provides very good conditions to study exotic nuclei. The fact that the projectiles do not leave the vacuum of the storage ring and the use of very thin internal target provide favourable conditions for high resolution measurements at low momentum transfer with high luminosity. The experimental conditions for such studies were tested at the existing storage ring ESR at GSI. Single small solid angle detectors representing all the detection systems to be included in EXL were installed at the ESR and the feasibility of the setup was tested with a stable ^{136}Xe beam. The target profile and size were measured. The elastic and inelastic scattering channels were observed. Other reaction channels like (p,pxn) and (p,2pxn) were also identified. The feasibility of the setup for reaction studies was confirmed and the results are considered as an important milestone for the EXL project at FAIR.

APPENDIX A

Absolute differential cross sections

Table A.1, Table A.2 and Table A.3 contain the experimental data points for the differential cross section for elastic scattering measured in inverse kinematics in the current experiment and analyzed in this work.

Table A.1: Measured differential cross section for p-^{12}Be elastic scattering at energy 700.5 MeV/u.

t, $(GeV/c)^2$	$d\sigma/dt$, $mb/(GeV/c)^2$	$\Delta\ d\sigma/dt$, $mb/(GeV/c)^2$
$0.164 \cdot 10^{-2}$	7683.84	259.089
$0.211 \cdot 10^{-2}$	6590.30	245.705
$0.258 \cdot 10^{-2}$	5796.99	229.290
$0.305 \cdot 10^{-2}$	5528.12	225.041
$0.352 \cdot 10^{-2}$	5248.16	224.871
$0.446 \cdot 10^{-2}$	4984.77	123.470
$0.586 \cdot 10^{-2}$	4157.88	115.881
$0.680 \cdot 10^{-2}$	3883.34	197.313
$0.727 \cdot 10^{-2}$	3827.75	197.511
$0.774 \cdot 10^{-2}$	3319.61	187.250
$0.891 \cdot 10^{-2}$	2901.40	75.8509
$0.113 \cdot 10^{-1}$	2548.63	88.9425
$0.127 \cdot 10^{-1}$	2337.00	116.150
$0.136 \cdot 10^{-1}$	2048.54	112.024
$0.145 \cdot 10^{-1}$	2041.63	110.186
$0.155 \cdot 10^{-1}$	1785.57	102.223
$0.164 \cdot 10^{-1}$	1753.28	104.870

continued on next page

continued from previous page		
t, $(GeV/c)^2$	$d\sigma/dt$, $mb/(GeV/c)^2$	$\Delta\ d\sigma/dt$, $mb/(GeV/c)^2$
$0.174 \cdot 10^{-1}$	1644.52	99.1812
$0.183 \cdot 10^{-1}$	1539.64	94.7981
$0.192 \cdot 10^{-1}$	1305.46	88.5779
$0.202 \cdot 10^{-1}$	1345.63	89.9429
$0.211 \cdot 10^{-1}$	1239.18	85.6318
$0.220 \cdot 10^{-1}$	1227.82	85.5067
$0.230 \cdot 10^{-1}$	1054.69	79.5557
$0.239 \cdot 10^{-1}$	919.586	75.2464
$0.249 \cdot 10^{-1}$	969.037	77.1342
$0.258 \cdot 10^{-1}$	956.969	76.9275
$0.267 \cdot 10^{-1}$	873.311	74.2124
$0.277 \cdot 10^{-1}$	770.759	70.6278
$0.286 \cdot 10^{-1}$	821.297	68.5959
$0.296 \cdot 10^{-1}$	808.733	69.5251
$0.305 \cdot 10^{-1}$	740.933	65.8939
$0.314 \cdot 10^{-1}$	718.647	66.4222
$0.324 \cdot 10^{-1}$	626.080	62.7858
$0.333 \cdot 10^{-1}$	602.815	60.7111
$0.342 \cdot 10^{-1}$	546.046	59.5907
$0.361 \cdot 10^{-1}$	495.899	33.0056
$0.385 \cdot 10^{-1}$	407.658	36.9156
$0.403 \cdot 10^{-1}$	362.691	34.2765
$0.422 \cdot 10^{-1}$	326.390	33.5579
$0.441 \cdot 10^{-1}$	288.716	31.5070
$0.460 \cdot 10^{-1}$	273.652	31.0106
$0.479 \cdot 10^{-1}$	277.204	30.6897
$0.497 \cdot 10^{-1}$	221.990	28.8375

Table A.2: Measured differential cross section for p-^{14}Be elastic scattering at energy 699.9 MeV/u.

t, $(GeV/c)^2$	$d\sigma/dt$, $mb/(GeV/c)^2$	$\Delta\ d\sigma/dt$, $mb/(GeV/c)^2$
$0.164197 \cdot 10^{-2}$	9634.82	421.987
$0.211111 \cdot 10^{-2}$	7618.37	400.393
$0.258024 \cdot 10^{-2}$	7171.60	371.693
$0.304938 \cdot 10^{-2}$	6243.02	361.553
$0.351851 \cdot 10^{-2}$	6200.38	355.609
$0.445678 \cdot 10^{-2}$	5673.31	196.862
$0.539505 \cdot 10^{-2}$	5317.73	340.617
$0.586419 \cdot 10^{-2}$	4783.58	328.419
$0.633332 \cdot 10^{-2}$	4553.99	311.440
$0.680246 \cdot 10^{-2}$	4418.89	309.695
$0.727159 \cdot 10^{-2}$	4382.49	311.080
continued on next page		

continued from previous page

t, $(GeV/c)^2$	$d\sigma/dt$, $mb/(GeV/c)^2$	Δ $d\sigma/dt$, $mb/(GeV/c)^2$
$0.797530 \cdot 10^{-2}$	4210.20	226.583
$0.913406 \cdot 10^{-2}$	3597.48	146.859
$0.104880 \cdot 10^{-1}$	3276.08	196.195
$0.118419 \cdot 10^{-1}$	2593.51	125.749
$0.131958 \cdot 10^{-1}$	2466.60	172.840
$0.140984 \cdot 10^{-1}$	2087.57	159.221
$0.150011 \cdot 10^{-1}$	1966.33	157.489
$0.159037 \cdot 10^{-1}$	1731.86	147.575
$0.177089 \cdot 10^{-1}$	1493.04	78.1376
$0.199654 \cdot 10^{-1}$	1095.40	83.6043
$0.213194 \cdot 10^{-1}$	973.751	109.800
$0.222220 \cdot 10^{-1}$	988.608	116.444
$0.231246 \cdot 10^{-1}$	935.490	111.505
$0.244785 \cdot 10^{-1}$	815.551	73.6571
$0.262838 \cdot 10^{-1}$	665.917	66.8068
$0.280890 \cdot 10^{-1}$	648.731	67.5933
$0.298942 \cdot 10^{-1}$	498.940	59.8007
$0.316995 \cdot 10^{-1}$	479.556	56.1793
$0.335047 \cdot 10^{-1}$	391.864	51.7567
$0.362125 \cdot 10^{-1}$	301.333	33.0055
$0.398230 \cdot 10^{-1}$	197.622	28.0605
$0.434335 \cdot 10^{-1}$	138.659	23.0834
$0.470439 \cdot 10^{-1}$	116.887	21.7853

Table A.3: Measured differential cross section for p-^{8}B elastic scattering at energy 700.5 MeV/u (preliminary results).

t, $(GeV/c)^2$	$d\sigma/dt$, $mb/(GeV/c)^2$	Δ $d\sigma/dt$, $mb/(GeV/c)^2$
$0.516 \cdot 10^{-1}$	9917.88	297.95
$0.610 \cdot 10^{-1}$	8227.76	255.26
$0.704 \cdot 10^{-1}$	7198.82	228.82
$0.798 \cdot 10^{-1}$	6450.34	209.32
$0.891 \cdot 10^{-1}$	5934.02	195.71
$0.985 \cdot 10^{-1}$	5365.69	180.56
$0.108 \cdot 10^{-1}$	4806.65	165.46
$0.117 \cdot 10^{-1}$	4518.77	157.6
$1.27 \cdot 10^{-2}$	4279.18	151
$1.36 \cdot 10^{-2}$	3785.14	137.23
$1.45 \cdot 10^{-2}$	3387.68	125.96
$1.55 \cdot 10^{-2}$	3281.82	122.92
$1.64 \cdot 10^{-2}$	3133.23	118.64
$1.74 \cdot 10^{-2}$	2754.35	107.57
$1.83 \cdot 10^{-2}$	2732.06	106.91

continued on next page

continued from previous page		
t, $(\mathrm{GeV/c})^2$	$\mathrm{d}\sigma/\mathrm{dt}$, $\mathrm{mb}/(\mathrm{GeV/c})^2$	$\Delta\ \mathrm{d}\sigma/\mathrm{dt}$, $\mathrm{mb}/(\mathrm{GeV/c})^2$
$1.92{\cdot}10^{-2}$	2531.48	100.94
$2.02{\cdot}10^{-2}$	2089.44	87.5
$2.11{\cdot}10^{-2}$	2078.3	87.15
$2.20{\cdot}10^{-2}$	2056.01	86.46
$2.30{\cdot}10^{-2}$	1853.57	80.12
$2.39{\cdot}10^{-2}$	1820.14	79.07
$2.49{\cdot}10^{-2}$	1678.98	74.56
$2.58{\cdot}10^{-2}$	1580.55	71.37
$2.67{\cdot}10^{-2}$	1387.39	65
$2.77{\cdot}10^{-2}$	1316.81	62.62
$2.86{\cdot}10^{-2}$	1329.81	63.06
$2.96{\cdot}10^{-2}$	1205.38	58.83
$3.05{\cdot}10^{-2}$	1177.52	57.87
$3.14{\cdot}10^{-2}$	1032.65	52.79
$3.24{\cdot}10^{-2}$	1002.93	51.73
$3.33{\cdot}10^{-2}$	921.21	48.78
$3.42{\cdot}10^{-2}$	861.78	46.59
$3.52{\cdot}10^{-2}$	850.64	46.18
$3.61{\cdot}10^{-2}$	806.06	44.51
$3.71{\cdot}10^{-2}$	726.2	41.47
$3.80{\cdot}10^{-2}$	711.34	40.9
$3.89{\cdot}10^{-2}$	689.05	40.03
$3.99{\cdot}10^{-2}$	679.77	39.67
$4.08{\cdot}10^{-2}$	655.62	38.72
$4.18{\cdot}10^{-2}$	575.76	35.51
$4.27{\cdot}10^{-2}$	562.76	34.98
$4.36{\cdot}10^{-2}$	527.47	33.52
$4.46{\cdot}10^{-2}$	501.47	32.42
$4.55{\cdot}10^{-2}$	458.75	30.59
$4.64{\cdot}10^{-2}$	397.46	27.89
$4.74{\cdot}10^{-2}$	410.46	28.47
$4.83{\cdot}10^{-2}$	388.17	27.47
$4.93{\cdot}10^{-2}$	339.88	25.23
$5.02{\cdot}10^{-2}$	308.31	23.72

APPENDIX B

Calculation of the vertex point from MWPC data

From the information obtained with the proportional chambers the vertex point of the interaction can be calculated. In Fig. B.1 the geometry of the chambers and the measured variables are displayed. From this variables the vertex point Z_v is

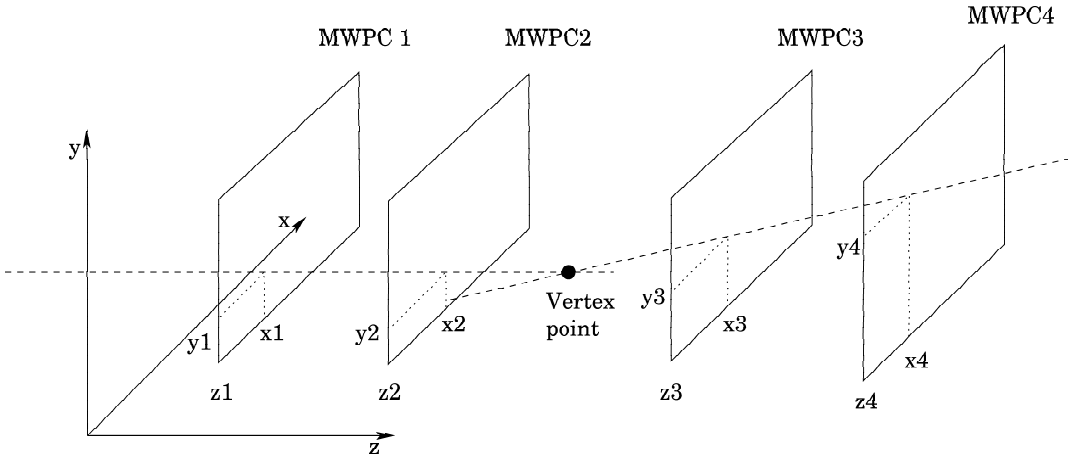

Figure B.1: Geometry for projectile tracking and coordinate determination necessary for calculating the vertex point Z_v.

calculated via the relations:

$$
\begin{aligned}
a_x &= \frac{x_2 - x_1}{\sqrt{(x_2 - x_1)^2 + (y_2 - y_1)^2 + (z_2 - z_1)^2}} \\
a_y &= \frac{y_2 - y_1}{\sqrt{(x_2 - x_1)^2 + (y_2 - y_1)^2 + (z_2 - z_1)^2}} \\
a_z &= \frac{z_2 - z_1}{\sqrt{(x_2 - x_1)^2 + (y_2 - y_1)^2 + (z_2 - z_1)^2}} \\
b_x &= \frac{x_4 - x_3}{\sqrt{(x_4 - x_3)^2 + (y_4 - y_3)^2 + (z_4 - z_3)^2}} \\
b_y &= \frac{y_4 - y_3}{\sqrt{(x_4 - x_3)^2 + (y_4 - y_3)^2 + (z_4 - z_3)^2}} \\
b_z &= \frac{z_4 - z_3}{\sqrt{(x_4 - x_3)^2 + (y_4 - y_3)^2 + (z_4 - z_3)^2}} \\
\theta_x &= \frac{b_x}{b_z} - \frac{a_x}{a_z} \\
\theta_y &= \frac{b_y}{b_z} - \frac{a_y}{a_z} \\
d_x &= x_3 - x_1 - z_3\frac{b_x}{b_z} + z_1\frac{a_x}{a_z} \\
d_y &= y_3 - y_1 - z_3\frac{b_y}{b_z} + z_1\frac{a_y}{a_z} \\
Z_v &= -\frac{d_x\theta_x + d_y\theta_y}{\theta_x^2 + \theta_y^2}
\end{aligned}
\tag{B.1}
$$

APPENDIX C

Relativistic kinematics of elastic scattering

For the description of the scattering processes of particles with energy ~1 GeV relativistic kinematics is used. The Lorentz invariant Mandelstam variables s, t and u describe the particle kinematics. In Eqs. (C.1) a general notation is used where the indices a and b indicate the incoming particles, and 1 and 2 indicate the outgoing particles after the interaction ($p_a + p_b \rightarrow p_1 + p_2$, see Fig. C.1),

$$\begin{aligned} s &= (p_a + p_b)^2 = (p_1 + p_2)^2 \ , \\ t &= (p_a - p_1)^2 = (p_b + p_2)^2 \ , \\ u &= (p_a - p_2)^2 = (p_b + p_1)^2 \ , \end{aligned} \tag{C.1}$$

where p is the four momentum. The variable s is the invariant mass of the two particles, t is the four momentum transfer in the direct channel and u is the four

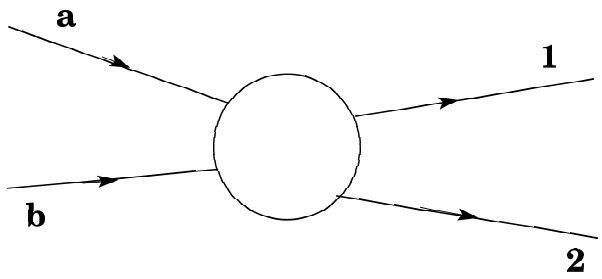

Figure C.1: Schematic representation of a reaction. Particles a and b are the incoming particles before the reaction and particles 1 and 2 are the reaction products (depending on the process they can be identical to a and b or different from them).

momentum transfer in the exchange channel. Only two of these variables are inde-

pendent and the three of them are related by:

$$s + t + u = m_a^2 + m_b^2 + m_1^2 + m_2^2 \ , \tag{C.2}$$

where with m the masses of the particles participating in the reaction are noted. A thorough description of the kinematics is given in [94].

The kinetic energy of the particle T, the total energy E, the linear momentum $\mathbf{p}$ and the four momentum p are connected via the relations:

$$\begin{aligned} E^2 &= \mathbf{p}^2 + m^2 = T + m \\ p^2 &= E^2 - \mathbf{p}^2 \\ \mathbf{p}^2 &= T^2 + 2mT \ . \end{aligned} \tag{C.3}$$

In terms of particle velocity the same variables are given by:

$$T = (\gamma - 1)m \quad \text{and} \quad \mathbf{p} = \beta\gamma m\mathbf{v} \ , \tag{C.4}$$

where

$$\beta = \frac{v}{c} = \sqrt{\frac{T(T+2m)}{(T+m)^2}} \tag{C.5}$$

is the velocity in units of the speed of light c and

$$\gamma = \sqrt{\frac{1}{1-\beta^2}} = \frac{T+m}{m} \tag{C.6}$$

is the total energy in units of the particle rest mass.

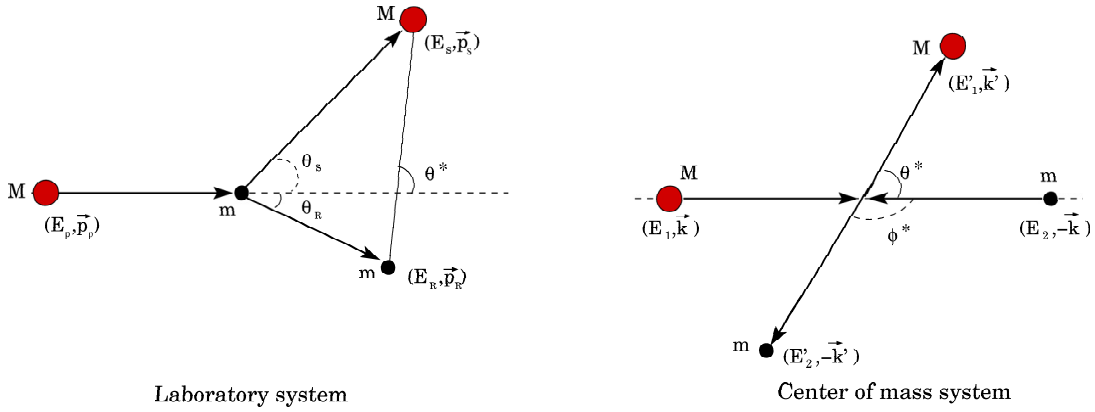

Figure C.2: Particle scattering kinematics in the laboratory system and in the center of mass system.

In Fig. C.2 the elastic scattering of a particle with mass M with a kinetic energy T_p on a particle with mass m is shown. From the conservation of energy and momentum it follows that the scattering angle of the projectile θ_s and the kinetic energy of the recoil target particle are related by:

$$cos\theta_s = \frac{T_p^2 + 2MT_p - T_R(T_p + M + m)}{\sqrt{T_p(T_p + 2M)(T_p - T_R)(T_p - T_R + 2M)}} \tag{C.7}$$

When this equation is solved for the energy of the recoil particle T_R we get its dependence from the scattering angle of the projectile:

$$T_R = T_p(T_p + 2M)\frac{m + (T_p + M)sin^2\theta_s - cos\theta_s\sqrt{m^2 - M^2sin^2\theta_s}}{(T_p + m + M)^2 - T_p(T_p + 2M)cos^2\theta_s} \tag{C.8}$$

The relation between the momentum of the particle in the center of mass system and the kinetic energy in the laboratory system can be derived by using the invariant mass of the system s expressed in the laboratory and the center of mass frames:

$$\mathbf{k}^2 = \frac{T_p(T_p + 2M)m^2}{M^2 + m^2 + 2(T_p + M)m} \ . \tag{C.9}$$

The four momentum transfer t is related to the particle momentum $\mathbf{k}$ via:

$$t = 2\mathbf{k}^2(1 - cos\theta^*) \ , \tag{C.10}$$

where θ^* is the scattering angle in the center of mass system. From this relation it follows that the differential cross section as a function of the solid angle Ω and as a function of the four momentum transfer t are related via:

$$\frac{d\sigma}{dt} = \frac{\pi}{\mathbf{k}^2}\frac{d\sigma}{d\Omega} \ . \tag{C.11}$$

Bibliography

[1] C. J. Batty *et al.*, Adv. Nucl. Phys. **19** (1989) 1

[2] L.-B. Wang *et al*, Phys. Rev. Lett. **93** (2004) 142501

[3] R. Sánchez *et al*, Phys. Rev. Lett. **96** (2006) 033002

[4] M. Zakova *et al.*, Hyper. Int. **171** (2006) 189

[5] I. Tanihata, J. Phys. G: Nucl. Part. Phys. **22** (1996) 157

[6] J. Al-Khalili, in *"The Euroschool Lectures on Physics with Exotic Beams, vol. I*, Lect. Notes Phys. **651** (2004) 77

[7] G. D. Alkhazov *et al.*, Phys. Rep. **42** (1978) 89

[8] S. R. Neumaier *et al.*, Nucl. Phys. **A712** (2002) 247

[9] G. D. Alkhazov *et al.*, Nucl. Phys. **A712** (2002) 269

[10] F. Aksouh, *Investigation of the core-halo structure of the neutron-rich nuclei* ^{6}*He and* ^{8}*He by intermediate-energy elastic proton scattering at high momentum transfer*, PhD thesis, Université de Paris-Sud UFR Scientifique D'Orsay, 2002

[11] A. V. Dobrovolsky *et al.*, Nucl. Phys. **A766** (2006) 1

[12] I. Tanihata *et al.*, Phys. Rev. Lett. **55** (1985) 2676

[13] P. Egelhof, Prog. Part. Nucl. Phys. **46** (2001) 307

[14] K. Riisager, Rev. Mod. Phys. **66** (1994) 1105

[15] P. G. Hansen, A. S. Jensen and B. Jonson, Annu. Rev. Nucl. Part. Sci. **45** (1995) 591

[16] Björn Jonson, Phys. Rep. **389** (2004) 1

[17] K. Riisager, in *"The Euroschool Lectures on Physics with Exotic Beams, vol. II*, Lect. Notes Phys. **700** (2006) 1

[18] The Borromean rings: http://www.liv.ac.uk/ spmr02/rings/

[19] I. Tanihata *et al.*, Phys. Lett. **B206** (1988) 592

[20] M. Zahar *et al.*, Phys. Rev. **C48** (1993) R1484

[21] E. Liatard *et al.*, Europhys. Lett. **13** (1990) 401

[22] T. Suzuki *et al.*, Nucl. Phys. **A658** (1999) 313

[23] Y. Kanada-En'yo *et al.*, Phys. Rev. **C52** (1995) 628

[24] J. S. Al-Khalili *et al.*, Phys. Rev. **C54** (1996) 1843

[25] I. J. Thompson and M. V. Zhukov, Phys. Rev. **C53** (1996) 708

[26] T. Neff, H. Feldmeier and R. Roth, Nucl. Phys. **A752** (2005) 321c

[27] P. Descouvemont, Phys. Rev. **C52** (1995) 704

[28] M. Labiche *et al.*, Phys. Rev. **C60** (1999) 027303; M. Labiche *et al.*, Phys. Rev. Lett. **86** (2001) 600

[29] T. Sugimoto *et al.*, Jour. Phys. **CS49** (2006) 43

[30] N. A. Orr and M. Freer, Nucl. Phys. **A654** (1999) 710c

[31] A. Navin *et al.*, Phys. Rev. Lett. **85** (2000) 266

[32] S. D. Pain *et al.*, Phys. Rev. Lett. **96** (2006) 032502

[33] H. Iwasaki *et al.*, Phys. Lett. **B481** (2000) 7

[34] Y. Kanada-En'yo and H. Horiuchi, Phys. Rev. **C68** (2003) 014319

[35] B. Blank *et al.*, Nucl. Phys. **A624** (1997) 242

[36] I. Pecina *at al.*, Phys. Rev. **C52** (1995) 191

[37] M. M. Obuti *et al.*, Nucl. Phys. **A609** 74

[38] R. E. Warner *at al.*, Phys. Rev. **C52** (1995) R1166; M. Fukuda *at al.*, Nucl. Phys. **A656** (1999) 209

[39] M. H. Smedberg *et al.*, Phys. Lett. **B452** (1999) 1

[40] C. Borcea *at al.*, Nucl. Phys. **A616** (1997) 231c

[41] W. F. Henning, Nucl. Instr. Meth. **B214** (2002) 211

[42] FAIR Baseline Technical Report, GSI Darmstadt, Germany (2006), http://www.gsi.de/fair/reports/btr.html

[43] EXL technical proposal:
http://www-linux.gsi.de/~wwwnusta/tech_report/05-exl.pdf

[44] The NUSTAR program:
http://www.gsi.de/fair/experiments/NUSTAR/index.html

[45] P. Egelhof *et al.*, Physica Scripta **T104** (2003) 151

[46] The GSI accelerator complex:
http://www.gsi.de/beschleuniger/Beschleuniger.html

[47] G. Münzenberg, Nucl. Instr. Meth. Phys. Res. **B70** (1992) 265

[48] H. Geissel *et al.*, Nucl. Instr. Meth. Phys. Res. **B70** (1992) 286

[49] J.-J. Gaimard and K.-H. Schmidt, Nucl. Phys. **A531** (1991) 709

[50] http://www-linux.gsi.de/~wolle/EB_at_GSI/FRS-WORKING/index.html

[51] http://www-linux.gsi.de/~weick/frs/frs-ion-optics.html

[52] *Passage of Particles Through Matter* in Review of Particle Physics, Eur. Phys. Jour. **C** (1998) 1

[53] http://www-linux.gsi.de/ weick/mocadi/

[54] A. A. Vorobyov *et al.*, Nucl. Instr. Meth. **119** (1974) 509

[55] J. P. Burq *et al.*, Phys. Lett. **77B** (1978) 438

[56] A. V. Dobrovolsky *et al.*, Nucl. Phys. **B214** (1983) 1

[57] S. Neumaier, *Untersuchung der nuklearen Dichteverteilungen der neutronenreichen Kerne ^{6}He und ^{8}He mittels elastischer Protonstreuung in inverser Kinematik bei Energien um 700 MeV/u*, PhD thesis, Fachbereich Physik, TH Darmstadt, 1995

[58] U. Fano, Phys. Rev. **72** (1947) 26

[59] T. Schäfer, *Einsatz von Szintillationszählern bei Experimenten zur Untersuchung der Nuclearen Dichteverteilung neutronenreicher Lithium-Isotope*, Diplomarbeit, Institut für Physik, Johannes Gutenberg Universität Mainz, 1997

[60] http://www.e12.physik.tu-muenchen.de/~gernhaus/projects/gassipl/gassidok.html

[61] http://www-win.gsi.de/daq/

[62] http://paw.web.cern.ch/paw/

[63] G. Velichko, *Performance simulation of cathode strip chamber prototype P1*, CMS NOTE 2000/022

[64] E. Mathieson and J. S. Gordon, Nucl. Instr. Meth. Phys. Res. **227** (1984) 277

[65] *Investigation of the dependence of ionization in gases on the energy of α-particles in ionization chambers*, PNPI Preprint **549**, February 1980

[66] G. Korolev, *private communication*

[67] A. G. Sitenko, *Theory of Nuclear Reactions*, World Scientific, 1990

[68] R. J. Glauber, *Theory of high energy hadron-nucleus collisions*, Proceedings of the 3^{rd} International Conference on high energy physics and nuclear structure, New York, 1970

[69] J Saudinos and C. Wilkin, Annu. Rev. Nucl. Sci. **24** (1974) 341

[70] J. A. McNeil *et al.*, Phys. Rev. **C27** (1983) 2123; R. A. Arndt *et al.*, Phys. Rev. **D28** (1983) 97

[71] Yu. N. Eldyshev *et al.*, Sov. Jour. Nucl. Phys. **16** (1973) 282

[72] I. Sick, Nucl. Phys. **A218** (1974) 509

[73] I. Sick, arXiv:nucl-ex/0208009v1, 14 Aug 2002

[74] Particle Data Group: http://pdg.lbl.gov/index.html;
W.-M. Yao *et al.*, Jour. Phys. **G33** (2006) 1

[75] H. Feldmeier and J. Schnack, Rev. Mod. Phys. **72** (2000) 655

[76] M. V. Zhukov *et al.*, Phys. Rep. **231** (1993) 151

[77] I. J. Thompson *et al.*, Nucl. Phys. **A588** (1995) 59c

[78] T. Neff and R. Torabi, *private communication*

[79] A. Delfino *et al.*, Phys. Rev. **C61** (2000) 051301

[80] J. Al-Khalili and J. A. Tostevin, Phys. Rev. Lett. **76** (1996) 3903

[81] A. Csótó, Phys. Lett. **B315** (1993) 24

[82] F. Carstoiu *et al.*, Phys. Rev. **C63** (2001) 054310

[83] http://www.gsi.de/fair/experiments/superfrs/index_e.html

[84] S. Ilieva *et al.*, Eur. Phys. Jour. **ST150** (2007) 357

[85] A. Bleile *et al.*, GSI Scientific Report 2004, p. 92

[86] G. Coló, *private communication*

[87] N. Kalantar-Nayestanaki *et al.*, *Results for the first feasibility study for the EXL project at the experimental storage ring at GSI*, Proceedings of the International Symposium on Physics of Unstable Nuclei ISPUN '07, World Scientific, 2008, p.139

[88] N. Kalantar-Nayestanaki *et al.*, *First feasibility study for EXL with prototype detectors at the ESR and detector simulations*, Proceedings of the 7^{th} International Conference on Nuclear Physics at Storage Rings STORI '08, Inter. Jour. Mod. Phys. **E**, *to be published*

[89] H. Moeini, private communication

[90] Z. Wang *et al.*, Phys. Rev. **C73** (2006) 014610

[91] R. Schmidt *et al.*, Phys. Rev. Lett. **70** (1993) 1767

[92] F. Schümann *et al.*, Phys. Rev. **C73** (2006) 015806

[93] A. Csótó and K. Langanke, Nucl. Phys. **A636** (1998) 240

[94] E. Byckling and K. Kajantie, *Particle kinematics*, John Wiley and Sons Ltd, 1973